# A multi-technique provenance study of the Oligocene – Recent Nile cone sediments and River Nile hinterland

*Thesis submitted in accordance with the requirements of Lancaster University for the degree of Doctor of Philosophy*

Laura Diane Fielding, MESci

September 2015

**Abstract**

This thesis presents the first detailed multiproxy provenance study of the modern Nile

catchment, together with Oligocene-Recent sediments of the offshore Nile cone, and

demonstrates for the first time that the palaeodrainage of the Nile has remained relatively

stable over the last 30 Ma.  Detrital mineral and bulk-rock analyses of modern river, wadi

and bedrock samples demonstrate the role of basement lithology, sedimentary recycling,

and modern geomorphological features in controlling the composition of sediment reaching

the Nile cone.

The bulk provenance signature of the modern Nile is dominated by the input of basic

detritus from the Cenozoic Ethiopian Large Igneous Province. Detrital zircon signatures are

dominated by variations in bedrock lithology, and the availability of easily-eroded

Phanerozoic cover sediments. These represent an important source of detritus to the river

and are characterised by the presence of strongly negative εHf populations at c. 600 and

1000 Ma, and significant populations of pre-Neoproterozoic grains.  Young zircon grains

derived from Ethiopian Cenozoic volcanic rocks are also recognised in samples from the Blue

Nile, Atbara and Nile trunk.

The Sr, Nd and Hf signature of Oligocene Nile cone sediments can only be explained if there

is significant input of mafic material being received from the hinterland. The Ethiopian Large

Igneous Province represents the only possible source for this detritus, indicating that the

Nile has been connected to the Ethiopian Highlands since this time. Zircons with U-Pb ages

and hafnium isotope signatures compatible with the Ethiopian LIP have been supplied to the

Nile cone since at least the Miocene (16 Ma).  Such zircons were not observed in Oligocene

delta sediments, but Sr, Nd and Hf isotope data for Oligocene delta muds as old as 31 Ma require significant mafic input.

The combined U-Pb and Hf-isotope zircon dataset for Nile catchment and cone sediments represents a significant archive that documents the evolution of the North African crust, in particular highlighting phases in the development of the Arabian Nubian Shield and amalgamation of Gondwana in late Neoproterozoic times.

## Acknowledgments

# Contents

| Table No. | Title | Page No. |
|---|---|---|
| **2.1** | Summary of previous work carried out on the evolution of the Nile. | 33-34 |
| **3.1** | Laboratory and experimental conditions used for U-Pb zircon and rutile | 58 |
| **3.2** | Zircon screening procedure | 61 |
| **3.3** | Rutile screening procedure | 61 |
| **3.4** | List of modern hinterland samples analysed as part of this study | 67 |
| **3.5** | List of core samples analysed as part of this study | 72 |
| **4.1** | Core samples analysed for heavy minerals | 97 |
| **4.2** | Core samples analysed for petrographic framework | 98 |

# Chapter 1: Introduction

## 1.1 Aims & Approach

Modern river sediments can be used to efficiently sample large areas of upstream crust in order to determine a region's geological and tectonic history (e.g. Iizuka et al., 2013).  This study aims to characterise the geochemical and isotopic signature of the modern Nile drainage basin, and using this information, to undertake a provenance study of Nile cone sediments dating back to Oligocene times.  This is the first study of the provenance of pre-Holocene Nile cone sediments, benefiting from unique access to core samples supplied by BP Egypt.

Analytical techniques were chosen based on their ability to discriminate between the possible Nile source areas. Techniques used include both *in situ* laser ablation geochronology of zircon and other minor phases, *in situ* hafnium isotope analysis of zircon, and bulk rock techniques such as radiogenic isotope tracer geochemistry, XRF, heavy mineral analysis, and petrography. Multiple methods have been used to ensure a robust provenance study.

The aims of the study are:

a) to determine the factors that influence the provenance signal of the modern river Nile.

The modern Nile drains a complex mosaic of terranes, including the Arabian Nubian Shield, the Saharan Metacraton, the Tanzania Craton, and Cenozoic volcanic rocks of the Ethiopian Large Igneous Province.  The study presents provenance data for modern river deposits sampling all of the above terranes.  Samples were taken from the Nile trunk in Egypt and Sudan, and its tributaries, the Blue and White Nile, Atbara, and Tekeze in Sudan, Ethiopia and Uganda (Figure 1.1).  Data from dry wadis

in the Red Sea Hills and Western Desert of Egypt, and ancient sedimentary and igneous/metamorphic rocks within the Nile's present and proposed past catchment, are also presented.

b) to use this knowledge of the modern Nile system to determine the likely sources of sediment to the offshore Nile cone.

Pre-drilled core samples from Oligocene to Recent Nile cone sediments were obtained from BP Egypt. The sedimentology of these samples had previously been described in BP reports, and dating had been carried out using biostratigraphic methods.  The Oligocene to Recent history of northern Africa encompasses a number of major geological events, including the uplift of the Ethiopian volcanic province, opening of the Red Sea, and the Messinian Salinity Crisis. Provenance data from the Nile cone sediments is used to investigate the changing catchment of the river throughout this time.

c) to determine when sediment derived from the Ethiopian Highlands first drained north to reach the Nile cone – in other words, to date the initiation of the Nile. Deposits from a north-flowing river of Eocene age exist on-land in northern Egypt, and the offshore Nile cone contains sediments as old as Oligocene.  It is not known if the early 'Nile' supplying these sediments had a local source in the Red Sea Hills, or if the catchment extended to the uplifting volcanic province in Ethiopia, far to the south.  An important goal of this study is to identify the earliest occurrence of Ethiopian detritus in the Nile cone sediments.

d) to use the new data on sediment supplied from the Nile catchment to contribute to our understanding of the region's geological history from Precambrian-Recent times.

The resulting data are used to document early crust-forming events, Precambrian orogenies culminating in the Neoproterozoic assembly of Gondwana, subsequent erosion and deposition of voluminous flysch deposits, and finally Cenozoic uplift and eruption of continental flood basalts resulting in the initiation of the Blue Nile in the Early Oligocene.

**Figure 1.1 Modern river samples and hinterland geology of Nile river source areas.** Inset shows location of map as boxed area. Map modified from (al-Miṣrīyah, 1981; Johnson, 2014; Kazmin, 1972; Ministry of Energy and Mines, 1981).

## 1.2 Thesis Structure

**Chapter 1:** Introduction

This chapter discusses the catchment area of the River Nile and the modern day contributions from each source area.

**Chapter 2:** Geology of the Nile Source Regions & Previous Work

This chapter provides background information on the geology of the source regions to the Nile delta cone and also reviews previous research.

**Chapter 3:** Analytical Methods

Here, each provenance technique used in this study is described in detail along with information on standards used and laboratory conditions.

**Chapter 4:** A detrital record of Nile hinterland evolution

Detrital mineral and bulk-rock analyses of modern river, wadi and bedrock samples were analysed in order to assess the role of basement lithology, sedimentary recycling, and modern geomorphological features on the composition of sediment reaching the Nile delta.

**Chapter 5:** When did the Nile begin?

Using the Oligocene – Recent Nile Cone sediments, the principal aim of this study was to determine the initiation of the present day Nile drainage, with a particular focus on when the Blue Nile began draining into the main Nile.

**Chapter 6:** The evolution of the river Nile and factors affecting the Nile cone sedimentary record.

In this paper, the dataset from Chapter 5 was expanded in order to look at the changing distribution of U-Pb and hafnium isotope data in detrital minerals, and other provenance proxies in the Nile delta since the Oligocene.

**Chapter 7:** Concluding Summary

This chapter summarises the main findings from all three papers.

**Chapter 8:** Limitations & Future Work

## 1.3 The Nile Catchment Area

The Nile River is arguably the longest river in the world.  It extends for more than 6,69500 km and drains an area of ~3.3 million square kilometres (Alam, 2001).  The present-day Nile is made up of three main tributaries: the Blue Nile, the Atbara and the White Nile (Figure 1.1).  The mean annual water discharge during times of peak flow is dominated by the Blue Nile (68%), followed by the White Nile (22%) and Atbara (10%) (Williams and Adamson, 1982). The majority of White Nile sediment load is trapped in extensive Sudd marsh swamps in South Sudan (Figure 1.1), and does not reach the main downstream Nile trunk.

**The White Nile:**

The White Nile is sourced from Lake Victoria in Uganda, and drains Archaean – Proterozoic rocks of the Congo and Tanzania Craton. It extends through Precambrian rocks of the Saharan Metacraton (Abdelsalam, 2002) in South Sudan.  For much of its course, the White Nile has an extremely low gradient due to its positioning along the floor of an ancient lake that occupied its valley as long ago as 400 ka before present (Williams and Williams, 1980), and which now forms an extensive area of marshland known as the Sudd.   The present flow regime of the Nile was established  in the late Pleistocene, at c.15 ka, when northwards flow was initiated due to intensification of the summer monsoon and resulting overflow of Lakes Albert and Victoria (Talbot et al., 2000; Williams et al., 2003).

**The Blue Nile and Atbara:**

The Blue Nile and Atbara are sourced in the Ethiopian Highlands, and drain Cenozoic flood basalts, Neoproterozoic Arabian-Nubian Shield basement rocks and

Phanerozoic sedimentary cover sequences.  Uplift of the Ethiopian Highlands in the Oligocene may have led to the initiation of flow in the Blue Nile.  However, there is no consensus in published literature about the timing of initiation of such flow (see section 2.3).

**The Red Sea Hills:**

The Red Sea Hills of eastern Egypt are not presently drained by an established river, but their proximity to the Nile means that sediment contributions from this region need further investigation. The Red Sea Hills are located in the east of Egypt. They run parallel to the Red Sea and extend south into northern Sudan. Bedrock in this area comprises Neoproterozoic Arabian Nubian Shield basement and overlying Phanerozoic sediments.

**The Western Desert of Egypt:**

The Western Desert is not drained by the Nile at the present day. However, some authors (Issawi and McCauley, 1992; Said, 1981) have suggested that the Palaeo-Nile catchment extended as far west as the Gilf Kebir in south-west  Egypt. The basement and cover of the Western Desert comprises Precambrian basement rocks of the Saharan Metacraton, overlain by Phanerozoic cover sequences.
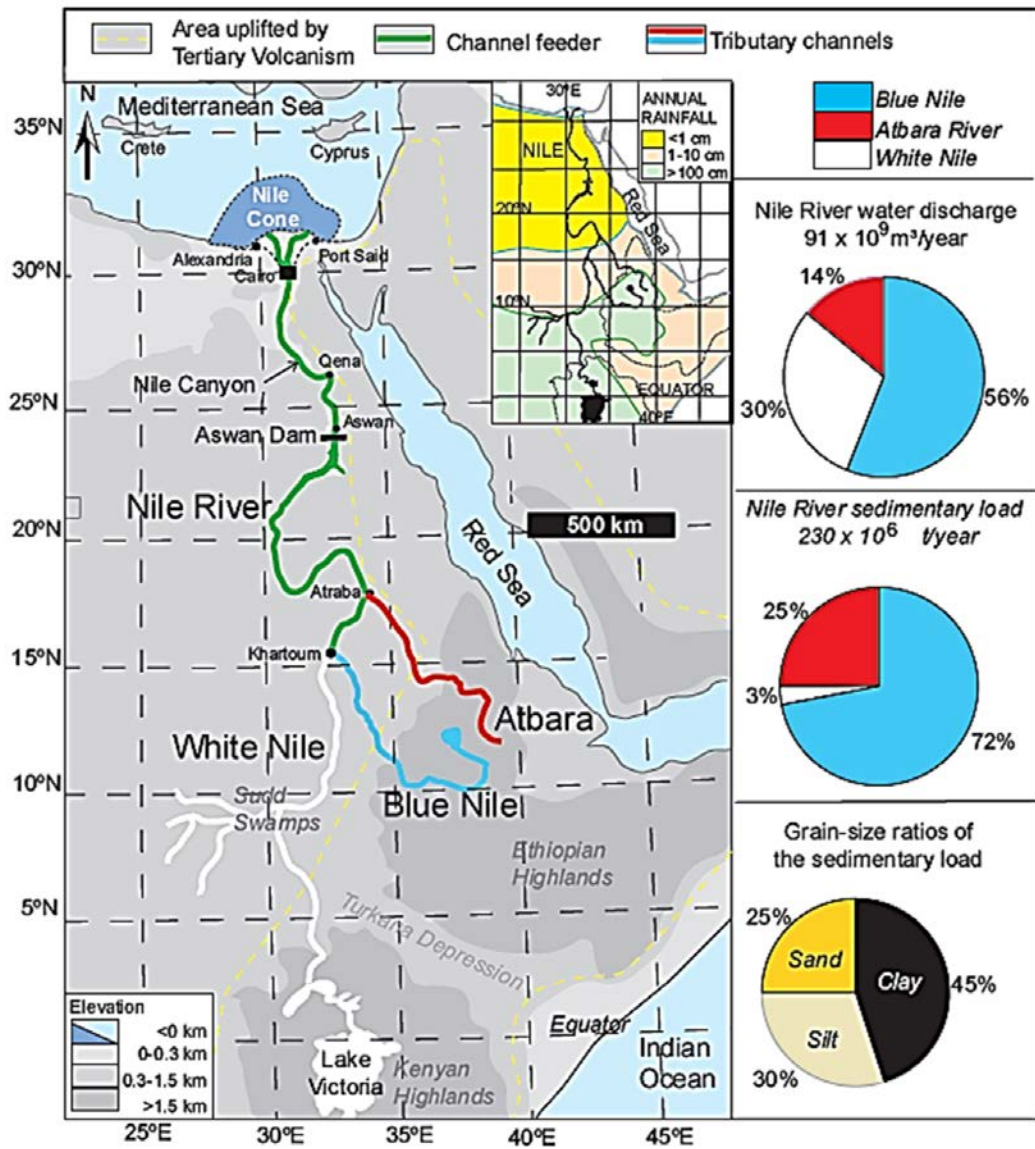
**Figure 1.2** Sediment load, precipitation and discharge rates for the modern Nile river catchment area, measured upstream of the confluene of each tributary. Modified from Adamson et al. (1980), Foucault and Stanley (1989), Garzanti et al. (2006) and Krom et al. (2002)

## Chapter 2:

Geology of the Nile Source Regions &

Nile Delta Cone Sediments

## 2.1 Geology of the Nile Source Regions

The geology of east Africa has largely been shaped by the events of the Pan-African Orogeny, during which east and west Gondwana collided to form 'Greater Gondwana' at the end of the Neoproterozoic (Figure 2.1 and Figure 2.2). The Pan-African orogeny involved the collision of ancient cratons such as the Congo and Tanzanian cratons and the Saharan Metacraton with the Arabian Nubian Shield, a terrane comprising more juvenile, Neoproterozoic oceanic island arcs. Cenozoic uplift of the Ethiopian Highlands, and uplift and rifting associated with opening of the Red Sea, have also had an important effect on the geology of the Nile catchment.

### 2.1.1 Precambrian cratons

The cratons of Central Africa are formed from various blocks of Archaean and Palaeoproterozoic crust, flanked or truncated by Palaeoproterozoic to Mesoproterozoic orogenic belts. Together, these form the Congo-Tanzania Craton (Figure 2.1), defined as the "amalgamated central African landmass at the time of Gondwana assembly", and incorporating the Angola-Kasai block and Tanzania Craton (De Waele et al., 2008).

The Congo craton (Figure 2.1) forms part of the West-African-Central-Belt which formed between 2.0 and 3.0 Ga ago and comprises orthogneisses, metasediments and granitoids of the Gabon-Kamerun Shield, Bomu-Kibalian Shield, Kasai Shield and the Angolan Shield (Cahen et al., 1984; Goodwin, 1996; Tchameni et al., 2000; Walraven and Rumvegeri, 1993).

The Tanzanian craton (Figure 2.1) covers an area of over 3,500,000 km$^2$ with an average elevation of 1260m (Cahen et al., 1984) and forms the eastern part of the

Congo-Tanzania Craton. It is almost entirely composed of granitoids and greenstone belts, with emplacement ages of c. 2700 Ma, and positive εNd values, suggesting derivation from a mantle source without significant involvement of older crust (De Waele et al., 2008).

The Saharan Metacraton is of particular interest, because it underlies a large area of the catchment of the Nile in north-east Africa, including much of Egypt.  The term 'Saharan Metacraton' (Figure 2.1) refers to an area of pre-Neoproterozoic continental crust which has, in part, been remobilised during the Pan-African orogeny (Abdelsalam, 2002).  It covers an area of 5,000,000 km$^2$ and extends from the Arabian Nubian Shield in the east to the Tuareg Shield in the west and the Congo Craton in the south. More than 50% of the Saharan Metacraton is overlain by Mesozoic 'Nubian' sediments and desert sands (Abdelsalam et al., 2011).  The poor exposure of the region means that the Saharan Metacraton, and its relationship to adjacent blocks, is poorly understood.  The southern boundary is not well defined, but is taken to be marked by the Oubangides orogenic belt which separates it from the Congo-Tanzania Craton (Abdelsalam, 2002). Little modern geochronology has been carried out on rocks of the Saharan Metacraton.  However, Bea et al. (2011) report Sensitive High Resolution Ion Microprobe (SHRIMP) U-Pb zircon ages as old as 3.22 ± 0.04 Ga for gneisses in the Uweinat and Gebel Kamil regions of the Western Desert in southernmost Egypt.

### 2.1.2 Arabian Nubian Shield

The Arabian Nubian Shield is a collage of Neoproterozoic (c. 870-670 Ma) continental margin and juvenile island arcs, overlain by younger sedimentary and volcanic basins, and cut by voluminous granitoid intrusions (Johnson and Woldehaimanot, 2003;

Kusky and Matsah, 2003; Stern, 1994). Only minor outcrops of pre-Neoproterozoic crust are found.  Formation of the Arabian Nubian Shield began with the initiation of subduction and arc-formation at 870 Ma. Terrane amalgamation associated with closure of the Mozambique Ocean and amalgamation of East and West Gondwana took place between c. 780 Ma and c. 600 Ma (Johnson and Woldehaimanot, 2003).

To the west of the Red Sea, the oldest arc terranes (> 800 Ma) of the Arabian Nubian shield occur in the south in Ethiopia, Eritrea and Sudan (Johnson and Woldehaimanot, 2003).  Contrastingly, ophiolitic rocks of the Eastern Desert of Egypt range in age from 810 to 720 Ma (Ali et al., 2010), and are overlain by younger (c.600 Ma) volcanic sequences (e.g. Breitkreuz et al. (2010)).

Pre-Cambrian alluvial sedimentary rocks of the Hammamat Formation overlie the Arabian Nubian Shield basement in the eastern desert of Egypt (Figure 1.1). The Hammamat Group clastic sediments comprise terrestrial molasse in the Red Sea Hills area and corresponding Midyan Terrane in northwest Saudi Arabia. The immature nature of the Hammamat molasse sediments imply that they were deposited during regional surface uplift and exhumation (Eliwa et al., 2010; Johnson et al., 2011a). However, Ries et al. (1983) suggests that the formation is in fact syn-deformational and was deposited during the collision of the Arabian Nubian Shield with the Saharan Metacraton, due to the cleaved and stretched nature of some of the sedimentary rocks.

### 2.1.3 The Pan-African Orogeny

During the Pan-African Orogeny, the final closure of the Mozambique Ocean led to amalgamation of the Saharan Metacraton and Congo-Tanzanian cratons with the

Arabian Nubian Shield, and the formation of the 'Trans-Gondwanan Supermountain' in the region that now forms NE Africa (Meinhold et al., 2013; Squire et al., 2006). To the south, collision between the Saharan Metacraton and Congo-Tanzania craton resulted in the formation of the Oubanguides orogenic belt or Central African Fold Belt (Abdelsalam et al., 2002). Erosion of the mountain belt resulted in the deposition of a thick cover of fluvial and marine sediments overlying the amalgamated terrains from the Cambrian onwards. Fluvial sediments were transported north (present co-ordinates) to the Gondwana margin, where they were inter-bedded with marine sediments deposited during periods of marine transgressions. Sedimentation continued until Cenozoic times, punctuated by periods of uplift caused by various plate collisions and disintegrations (Klitzsch and Squyres, 1990).

### 2.1.4 Phanerozoic cover sequences

Previous studies of the cover sediments in regions adjacent to the Nile catchment (i.e. Libya, Jordan, Israel) have proposed contrasting Phanerozoic palaeogeographies for the region. Altumi et al. (2013) and Kolodner et al. (2006a) record a trend from arkosic basal sediments with a dominant restricted Late Neoproterozoic zircon population, to quartz arenites with an increasing number of older zircons (peaks at ca. 1000, 2000 and 2500 Ma) in the overlying succession. Meinhold et al. (2011) studied Mesozoic and Palaeozoic sediments of southern Libya, and ascribe the textural and mineralogical maturity of the bulk of the cover, and the provenance of the sediments, to varying degrees of recycling, long distance transport, and/or intense chemical weathering. In particular, long-distance transport has been suggested to explain a c.1000 Ma zircon population for which an obvious basement

source in the Saharan Metacraton or Arabian Nubian Shield has not been recognised (Kolodner et al., 2006a; Meinhold et al., 2011).

### 2.1.5 Cenozoic uplift and eruption of flood basalts

More recently, uplift of the Red Sea Hills associated with opening of the Red Sea rift, and uplift in Ethiopia associated with eruption of voluminous continental flood basalts, have had a major influence on Nile drainage (Figure 2,2). Many studies have attempted to ascertain the timing of Red Sea Hills uplift, with authors suggesting that uplift of rift shoulders began at around 24 Ma (Bosworth et al., 2005), 25-30 Ma (Ghebread, 1998), <29 Ma (Kenea, 2001) and 34 Ma (Omar and Steckler, 1995).

The continental flood basalts that dominate much of the Ethiopian Highlands are associated with East African plume activity, rifting and continental break up (Buck, 2006; Ebinger, 2005). Pre-rift basaltic magmatism initiated at around 31 Ma (Baker et al., 1996; Rochette et al., 1998; Ukstins et al., 2002), and subsequent plume-related uplift caused faulting within what is now the Ethiopian Highlands. Plume-related uplift was succeeded by formation of the Afar depression and shield-volcano building episodes between 26 and 22 Ma (e.g. the Choke and Guguftu shield volcanoes) (Gani et al., 2007). During these periods, a significant volume of rhyolitic lava and ignimbrites were emplaced.  Whereas the continental flood basalts are poor in zircon, the more evolved rhyolites and ignimbrites are of particular importance to this study because they represent a fertile source of zircon to the Nile catchment.
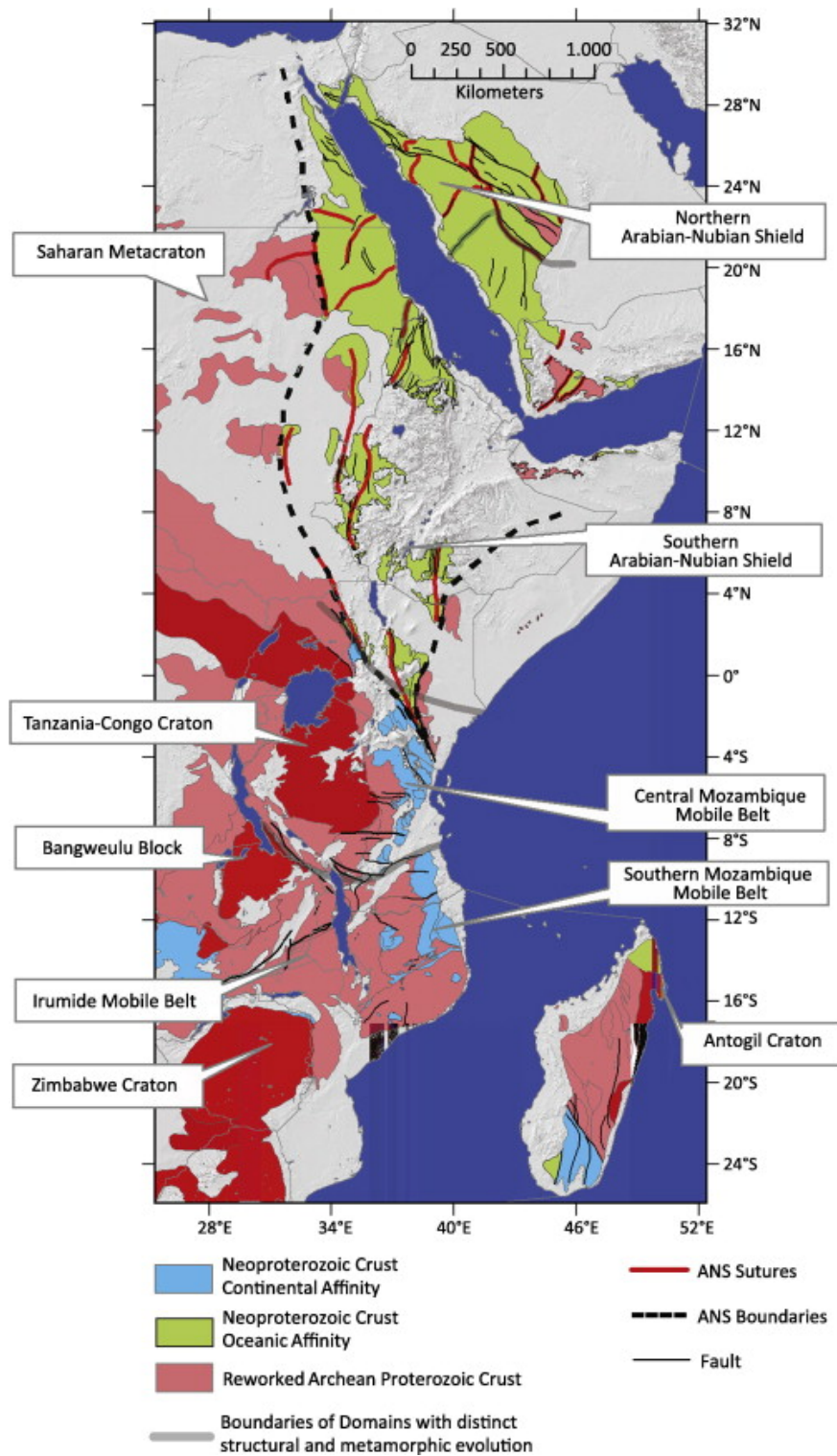
**Figure 2.1** Geological map depicting the location the terranes involved in the Pan-African Orogeny at c.600 Ma (Johnson et al, 2012).
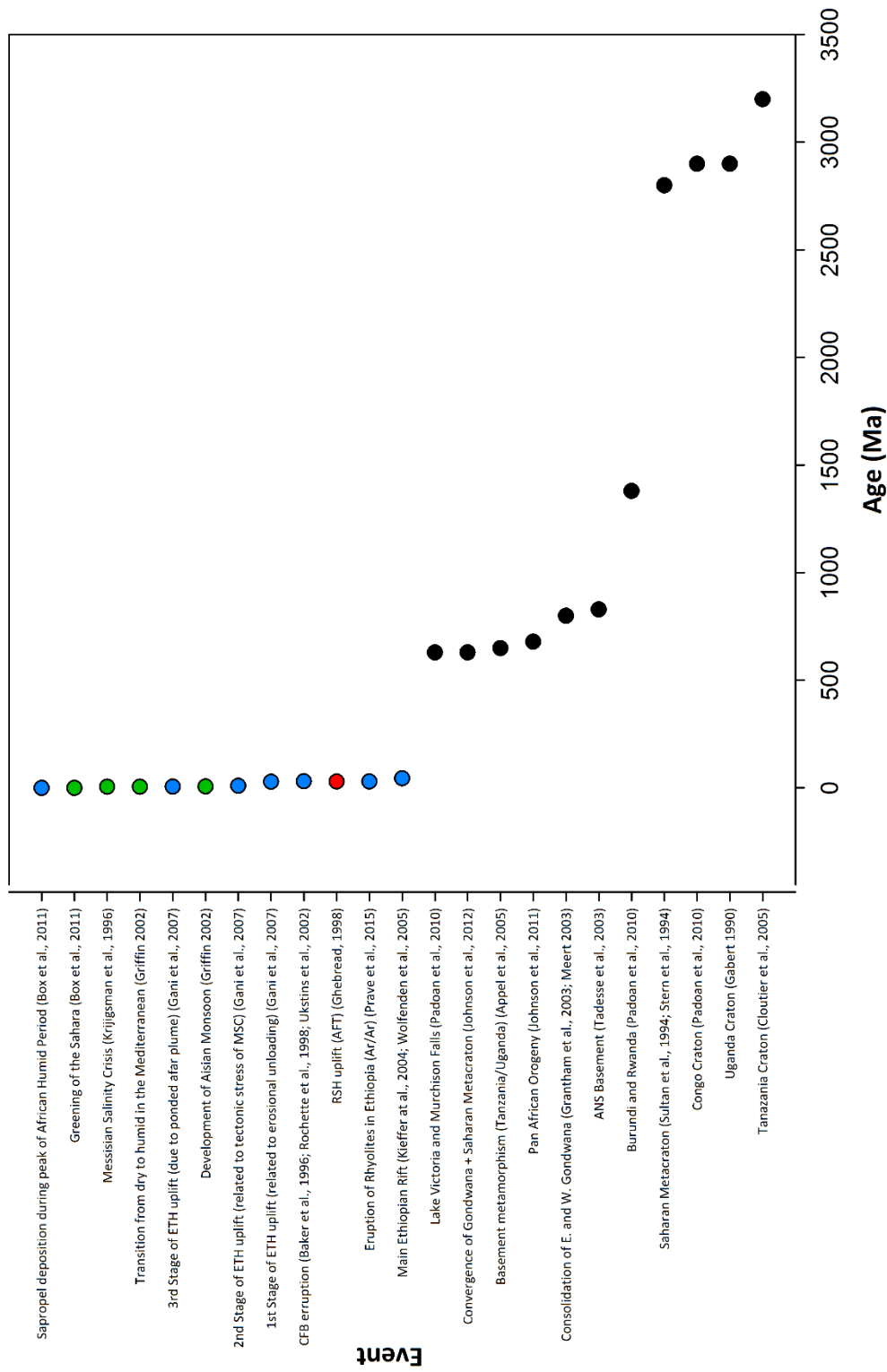
Figure 2.2. Graphical representation of the tectonic history of North East Africa.

## 2.2 The Nile Cone

The offshore Nile Delta area is subdivided into three major basins (Figure 2.3): the Middle to Late Miocene Nile Cone Basin in the West, the Central Late Oligocene to Early Miocene basin and the Early Cretaceous basin lying offshore from the Sinai Peninsula in the East. Rifting of this area started in the Late Triassic and persisted until Early Cretaceous (Loncke et al., 2006). Subsequently, the depositional area was controlled by four main tectonic phases (Dolson et al., 2001):

| End Early Cretaceous | Extensional tectonics causing tilting of northern Egypt; |
|---|---|
| Late Cretaceous | NW-SE oblique compressional/transpressional tectonics ending in the Eocene closure of the Tethys Ocean |
| Late Oligocene – Early Miocene | Uplift and separation of the Arabian Platform from the Levantine Basin |
| Early Pliocene | NW-SE trending wrench faults developed in the northern offshore areas. |
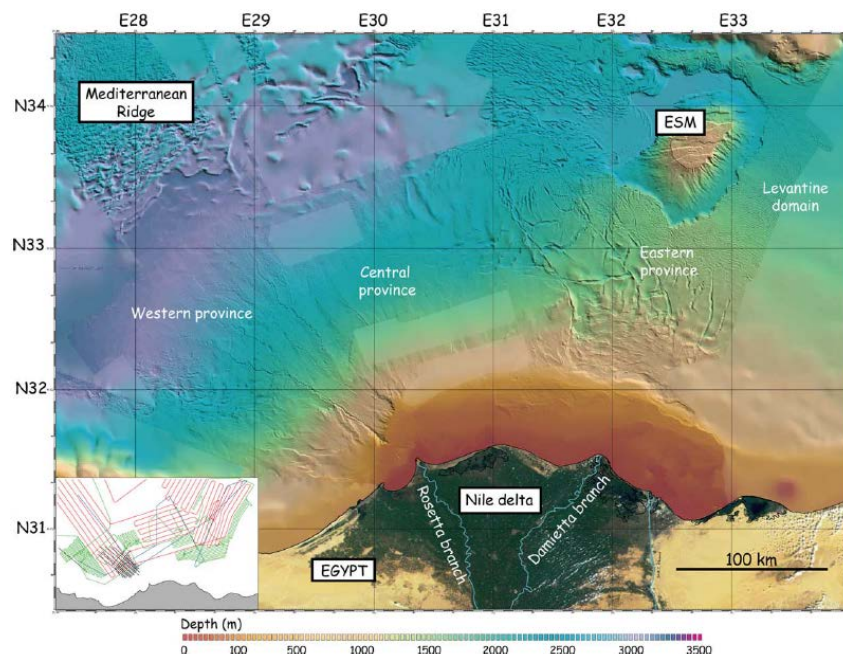


**Figure 2.3** Bathymetric map of the Nile delta and submarine Nile cone showing the East, West and Central provinces (Loncke et al., 2006). ESM= Erasmus Sea Mount. Inset is an example of the extent of seismic data coverage of the area.

## 2.3 Previous work on the evolution of the Nile

The palaeodrainage history of the Nile has been the subject of debate, with estimates for the initiation of an extensive drainage network ranging from Oligocene to Pleistocene. Table 2.1 summarises previous work carried out on each main Nile source area in order to characterise it's provenance signature.

The timing of initiation of the White Nile has been studied by Williams et al. (2003), who used optical luminescence to date the finely laminated alluvial clays and sands on the floor of a palaeolake in the White Nile valley. They demonstrate that initiation of the White Nile took place at c.250 k.y. ago. It is still unclear at what point detritus from the White Nile reached the Nile delta cone.

The point at which Nile drainage changed from a locally sourced Red Sea Hills catchment to a more extensive catchment encompassing the Ethiopian Highlands (via the Blue Nile and Atbara) is poorly known, with estimates ranging from Oligocene to Late Pleistocene (Issawi and McCauley, 1992; Macgregor, 2012; Pik et al., 1999; Shukri, 1950).

A number of authors have presented palaeogeographies and palaeodrainage maps from the Late Eocene onwards. The different models outlining evolution of the Nile are discussed in Table 2.1.

| Author | Time | Evolution Hypotheses | Method |
|--------|------|----------------------|--------|
| Williams et al., 2003 | | Initiation of the White Nile took place at c.250 k.y. ago. It is still unclear at what point detritus from the White Nile reached the Nile delta cone. | Optical luminescence used to date the finely laminated alluvial clays and sands on the floor of a palaeolake in the White Nile valley |
| Salem, 1976 | Late Eocene | Carbonate sedimentation with minor terrigenous influx. Filled the remaining basin and the shoreline prograded northwards. | |
| McCauley et al., 1986 | Late Eocene | 'The Trans-African Drainage System' (Figure 2.4) – sediment from the Red Sea Hills was diverted and deposited in the Atlantic. | Remote sensing of radar rivers in the Western Desert. |
| Issawi and McCauley 1992; Said, 1981 | Late Eocene | 'The Gilf System' - (Figure 2.5) an extensive drainage system originating in the Red Sea Hills region, flowing west before bending round to the north and meeting the Mediterranean at Siwa. system also includes a north-flowing stream that followed the retreating Tethys Sea and flanked the emerging Red Sea Hills with a delta forming in the Fayoum area | Based on sparse Landsat data which penetrates c.50cm beneath dune sands |
| Pik et al., 2003 and Gani et al., 2007 | Oligocene (25-29 Ma) | Blue Nile and Tekeze Gorges were initiated in Ethiopia between 25-29 Ma. This suggests that the elevated plateau physiography, which controls most of the present-day Nile hydrology, has been in place since the Oligocene | Thermochronological studies (Pik et al., 2003). Fluvial geomorphology and 'knick-point' facies (Gani et al., 2007) |
| Bosworth et al., 2005; Craig et al., 2011; Burke and Wells 1989 | Oligocene (c.24 Ma) to Early Miocene | Initial stages of uplift in the Red Sea Hills – coeval with a sharp change in clastic input to the Nile and the Nile delta which resulted in a NE progradation of the delta from Fayoum. | |
| Issawi and McCauley et al., 1992; Bosworth et al., 2005 | Early Miocene | "Qena System" - (Figure 2.6), a major south-flowing stream developed down the dip slope of a zone of intensified uplift in the Red Sea range during the early Miocene. Suggested deposition of | Remote sensing of radar rivers in the Western Desert. |

| Author | Time | Evolution Hypotheses | Method |
|--------|------|---------------------|--------|
| | | Red Sea Hills sediment in the Gulf of Guinea. | |
| Issawi and McCauley et al., 1992; Said, 1981 | Late Miocene (5.96 to 5.33 Ma) | "The Nile System" – (Figure 2.7) A drop in Mediterranean Sea level, coeval with the Messinian Salinity Crisis caused the head-ward erosion (northwards) of the limestone plateau, capturing the "Qena System". This was coeval with the formation of the Eonile Canyon which reaches as far back as Aswan. | Remote sensing of radar rivers in the Western Desert. |
| Sestini, 1989; Woodward et al., 2007 | Early Pliocene | Marine sediments began to fill the Eonile Canyon (Figure 2.8). Red Sea Hills sediments are said to be an important source of sediment at this time. | |
| Sestini, 1989 | Late Pliocene | The Nile began to advance across the marine embayment where large quantities of sand and mud were then dispersed far into the eastern Mediterranean creating a large sub-marine fan. | |
| Macgregor 2012; Shukri, 1950 | Plio-Pleistocene | Nile trunk was not connected to the Ethiopian Highlands until the Plio-Pleistocene. These calculations assume that the Ethiopian Highlands only contributed volcanic sediments to the delta and not clastic sediments from the Phanerozoic cover. This data has been coupled with mineralogical data whereby the low pyroxene content of delta sediments has been taken to indicate that Ethiopian detritus was being deposited elsewhere until the Pleistocene. | Sediment volume calculations (MacGregor, 2012) and heavy mineral analysis (Shukri, 1950) |
| Pickford and Mein, 2006 | Pleistocene (c.2 Ma) | Nilotic biota found in Lake Albert indicates that the White Nile was connected to the main Nile at this time. | Biostratigraphy |

**Table 2.1** Summary of previous studies carried out in order to ascertain the evolution of the Nile River.
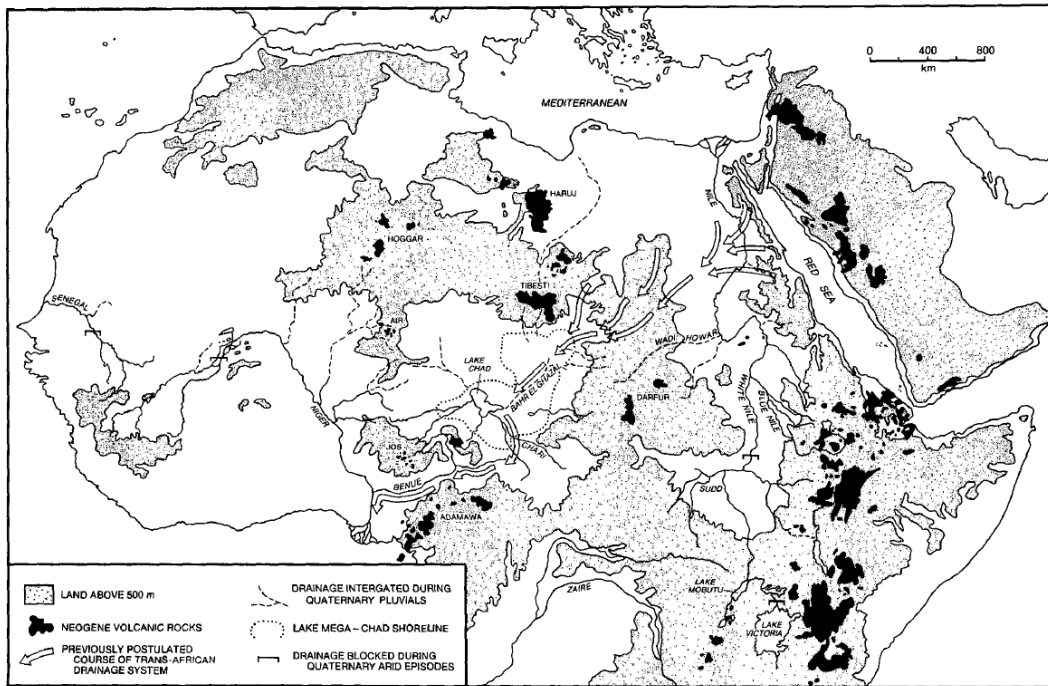
**Figure 2.4** The Trans-African Drainage System was proposed by Mccauley et al. (1986).



**Figure 2.5** The 'Gilf System' proposed by Issawi and McCauley (1992).
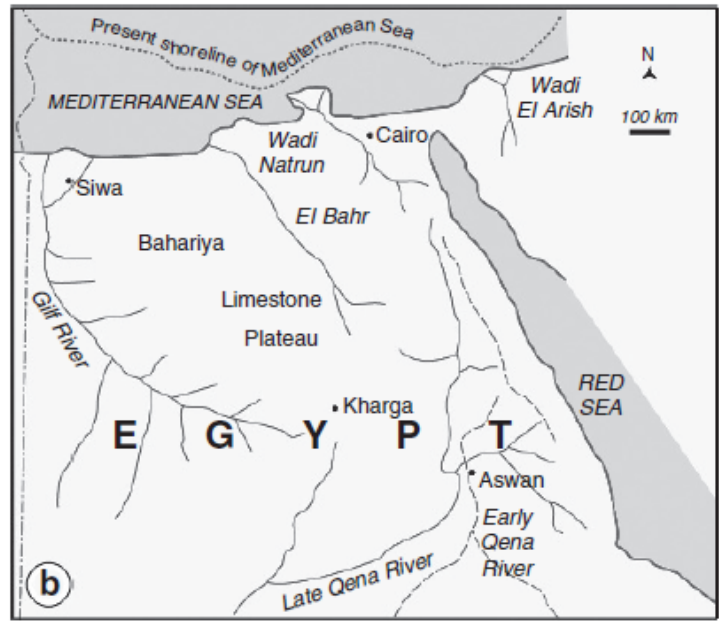
**Figure 2.6** The 'Qena System' as suggested by Issawi and McCauley (1992) proposes a major south-flowing stream during the early Miocene.
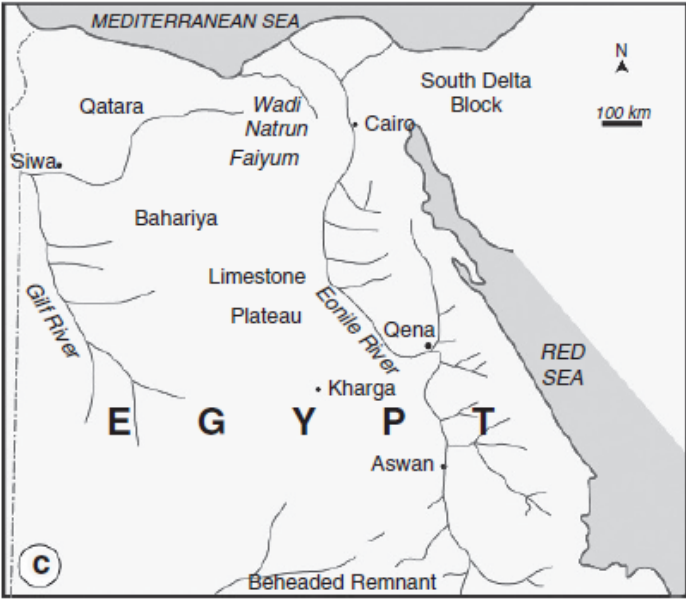


**Figure 2.7** The 'Nile System' proposed by Issawi and McCauley (1992). A drop in sea-level during the Messinian Salinity Crisis caused down-cutting and head ward erosion, capturing new river drainages (the Qena System), coeval with the formation of the Eonile Canyon.
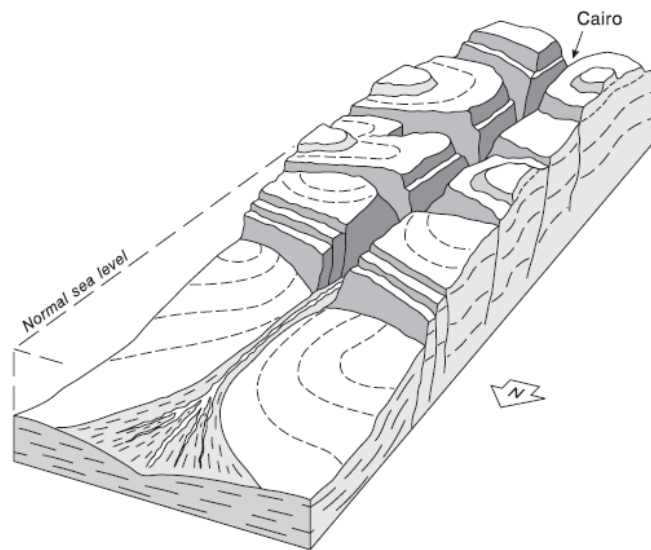
**Figure 2.8** The Eonile Canyon, which formed as a result of down-cutting during the Messisnan Salinity Crisis (Said, 1981).

## 2.4 Previous work on the isotope signature of Nile sediments

The provenance of sediments in the Nile River has previously been studied using heavy mineral distributions and petrography, Sr and Nd trace isotope studies, and U-Pb analysis of detrital zircons.

Sr and Nd ratios have proved useful when recording major changes in provenance along the course of the River Nile (Padoan et al., 2011). High $^{87}Sr/^{86}Sr$ ratios and low εNd values in White Nile muds from Archaean cratonic sources contrast with lower $^{87}Sr/^{86}Sr$ and higher εNd in the River Sobat, which receives most of its sediment load from the crystalline basement and Cenozoic volcanic rocks of the Ethiopian Highlands. Isotope signatures of the Blue Nile and Atbara Rivers are dominated by Ethiopian volcanic detritus and show low $^{87}Sr/^{86}Sr$ ratios and higher εNd values.

Heavy mineral analysis and petrography have also been used to characterise the signature of the Nile catchment area (Garzanti et al., 2006). The Blue Nile, Atbara and Tekeze drain predominantly flood basalts and rhyolitic ignimbrites in their upper courses until they reach the Neoproterozoic amphibolite-facies basement (Arabian Nubian Shield) consisting of granitoid gneisses, staurolite-bearing schists, and marbles (Tadesse et al., 2003) and Phanerozoic sediments found in the pre-rift sedimentary succession of the Blue Nile Canyon (Figure 4.1).

The Victoria Nile (downstream of the Lake Victoria output) carries feldspatho-quartzose sand, with feldspars derived from locally exposed granitoid rocks (Garzanti et al., 2006). Downstream of the Lake Albert outlet, Albert Nile sand is quartzose with few feldspars and a low abundance of heavy-mineral suites with epidote, hornblende, kyanite, rutile and zircon. The Nile composition changes across South Sudan, and White Nile sand of all grain sizes downstream of the Sudd marshes chiefly consists of monocrystalline quartz and becomes slightly enriched in plagioclase, volcanic lithics and clinopyroxene recycled from the Gezira Fan, which is ultimately derived from the Ethiopian Traps via an overspill from the Blue Nile (Garzanti et al., 2006).

Iizuka et al., (2013) present coupled U-Pb, Lu-Hf and O-isotope data for detrital zircons from a sample of modern Nile sand taken, somewhat cryptically, 'Near Cairo City'. They identified age peaks at 1.1-0.9, 0.85-0.7 and 0.7-0.55 Ga, with minor groups at c. 2.6 and 2.0 Ga. They noted that grains with ages between 0.85 and 0.7 Ga had positive $\epsilon$Hf values, and were likely to have been derived from juvenile crust in the Arabian-Nubian Shield. Zircons with ages of 1.1 – 0.9 and 0.7-0.55 Ga,

coinciding with times of supercontinent assembly, showed wide variations in O-isotope composition and εHf.

Be'eri-Shlevin et al. (2014) discuss U-Pb and Hf-isotope data for detrital zircons in Quaternary to Recent Israeli coastal sands, which are believed to have been derived by a combination of longshore drift and aeolian transport from the Nile delta.  They conclude that the ubiquitous presence of 0.56-0.75 Ga detrital zircons with negative εHf implies that the Arabian-Nubian shield (which is dominated by zircon grains of this age but with positive εHf) is not the main source of Nile sands.  Rather, they believe that multiple recycling through Phanerozoic sedimentary rocks that blanketed North Africa explains both the detrital zircon age / hafnium distribution, and the quartz budget of the system.

Despite the substantial number of isotope, heavy mineral, radar river, landsat, fluvial geomorphological and exhumation studies carried out on the modern Nile drainage system and hinterland, existing data for the Nile cone and or delta does not extend further back than the Holocene (Revel et al., 2010). Therefore, up until now, it has not been possible to tie all of this data cohesively together to help constrain the development for the ancient Nile, from Oligocene to recent times. This study aims to generate a more complete review of the evolution of the River Nile and it's catchment area.

**Chapter 3:** Analytical Methods

Both mud and sand samples were collected from the modern Nile catchment area, in order to carry out both single grain and bulk rock provenance techniques. Sample locations are shown in Figure 1.1 and are tabulated in Table 3.4 When collecting modern river samples, care was taken to avoid contamination from other sources. This was done by sampling upstream of any bridges, mining or construction sites and in as remote areas as possible. Aeolian contamination was avoided by ensuring samples were taken from below the surface and were clearly water lain (e.g. showing ripple lamination).

Mud, sand and silt samples were collected from pre-drilled core taken from the Nile cone during visits by the author to BP Egypt, Cairo (Table 3.5). Samples from the cone were limited to the intervals where core had been drilled and varied from consolidated to unconsolidated. All core had previously been logged and dated using biostratigraphy by BP Egypt.

## 3.1 Major and Trace Element Analysis

X-Ray Fluorescence (XRF) geochemistry is a quantitative, non-destructive tool for measuring different quantities of trace and major elements within both consolidated and unconsolidated rock samples. The interaction of x-rays with the sample causes the emission of characteristic secondary X-rays, which allows determination of its geochemical composition. A wavelength dispersive spectrometer was used at the Open University to analyse silicate rock samples for 10 major and minor elements ($SiO_2$, $TiO_2$, $Al_2O_3$, $Fe_2O_3$, $MnO$, $MgO$, $CaO$, $Na2O$, $K_2O$ and $P_2O_5$) as percentage oxides and 20 trace elements (Rb, Sr, Y, Zr, Nb, Ba, Pb, Th, U, Sc, V, Cr, Co, Ni, Cu, Zn, Ga, Mo, As and S) at ppm levels.

**Sample Preparation and Analyses:** 20 grams of bulk rock mud samples (modern river and core muds) were dried and powdered using a micro-mill or pestle and mortar at Lancaster University. These samples were then sent to John Watson at the Open University, where each powdered rock sample was then mixed with lithium borate and fused in a platinum crucible at 1100˚C. The resulting melt was pressed in a brass mould to form a circular glass disc in preparation for major element analysis. For trace element analysis rock powder was mixed with a binding agent and compressed in a steel mould to form a 35 mm diameter pellet. Reference materials used include: WS-E, OU-3 (majors), BHVO-1, QLO-1, DNC-1, W-2 (traces).

## 3.2 Heavy Mineral Analysis

Heavy mineral analysis was carried out by Eduardo Garzanti, Marta Padoan and Sergio Andò at the Dipartimento di Scienze Geologiche e Geotecnologie, Universita di Milano-Bicocca. A comparison of the heavy mineral assemblages obtained from the Nile delta as part of this study with the existing hinterland data sets, it may be possible to gain a better understanding of the evolution of the Nile river over time.

### 3.2.1 Nile Cone Sands

A split aliquot of the same 16 sand samples analysed for petrography were dry sieved and both fine cohesive material (< 32 μm) and coarse fragments thus eliminated, because the presence of detrital grains with great size differences within a single concentrate makes mounting and identification difficult (Mange and Maurer, 1992).

In order not to cut off and lose a significant part of the heavy-mineral population, and to obtain a representative quantitative description of the detrital assemblage, a 3.5 to 4 ϕ-wide size-window for analysis was chosen. From a split aliquot of the

selected 32-355 or 32-500 µm classes, which are thought to be most representative of the whole heavy-mineral spectrum, the dense fraction was separated by centrifuging in sodium metatungstate (density ~ 2.90 g/cm$^3$), and recovered by partial freezing with liquid nitrogen. No chemical pre-treatment, which might have modified the original detrital assemblage in the laboratory, was used.

Between 200 and 270 transparent heavy minerals were counted in grain mounts by the "area method" (Galehouse, 1971). For each mineral species, the percentage of corroded, etched, deeply etched and skeletal grains was also observed and quantitatively recorded.

Heavy-mineral concentration was calculated as the volume percentage of total (HMC) and transparent (tHMC) heavy minerals; the SRD (Source Rock Density) index was calculated as the weighted average density of terrigenous grains after assigning a suitable density to each detrital species (Garzanti and Andò, 2007). Transparent heavy-mineral suites are described as "extremely poor" (tHMC < 0.1), "very poor" (0.1 ≤ tHMC < 0.5), "poor" (0.5 ≤ tHMC < 1), "moderately poor" (1 ≤ tHMC < 2), "moderately rich" (2 ≤ tHMC < 5) and "rich" (5 ≤ tHMC < 10).

The "Hornblende Colour Index" HCI, based on the relative abundance of blue-green, green, green-brown and brown hornblende grains, and the "Metasedimentary Minerals Index" MMI, based on the relative abundance of chloritoid, staurolite, kyanite, andalusite and sillimanite (Andò et al., 2012; Garzanti and Andò, 2007), were calculated to estimate the average metamorphic grade of metaigneous and metasedimentary source rocks. They both vary from 0 in detritus from greenschist-facies to lowermost amphibolite-facies rocks yielding exclusively blue/green

amphibole and chloritoid, to 100 in detritus from granulite-facies rocks yielding exclusively brown hornblende and sillimanite. The ZTR index (Hubert, 1962) indicates the percentage of stable zircon, tourmaline, rutile and other Ti oxides over total transparent heavy minerals, and varies from 0 to 100.

### 3.2.2 Nile Cone Muds

As with the sand samples, the 8 selected mud samples were wet sieved in order to eliminate both the finer mud (clay to fine silt) and sand fractions, in order to make mounting and identification easier. A 2 $\phi$-wide size-window was chosen for analysis as to avoid cutting off and losing a significant part of the heavy-mineral population, and to obtain a faithful quantitative description of the detrital assemblage. From a split aliquot of the selected 15-63 µm class, held as representative of the entire heavy-mineral spectrum, the dense fraction was separated by centrifuging in sodium metatungstate (density ~ 2.90 g/cm$^3$), and recovered by partial freezing with liquid nitrogen. No chemical pre-treatment, which might have modified the original detrital assemblage in the laboratory, has been used.

For most samples, 200 to 230 transparent heavy minerals were counted in grain mounts by the "area method"(Galehouse, 1971). For NDM12 and NDM31, the former dominated by very numerous unidentifiable turbid grains and the latter extremely poor in heavy minerals, only 79 and 63 transparent heavy minerals could be counted in the whole slide, respectively. For each mineral species, the percentage of corroded, etched, deeply etched and skeletal grains was also observed and quantitatively recorded.

The same criteria as illustrated above were followed to describe transparent-heavy-

mineral assemblages and to calculate the HMC, tHMC, SRD, HCI, MMI and ZTR

indices.

## 3.3 Petrography

Petrographic analyses were carried out by Eduardo Garzanti and Giovanni Vezzoli at the Dipartimento di Scienze Geologiche e Geotecnologie, Universita di Milano-Bicocca, Italy.

Split aliquots of each bulk sample were impregnated with Araldite and prepared as standard thin sections including the addition of alizarine red (stain) to distinguish between calcite and dolomite. In each thin section, 400 grains were counted according to the Gazzi-Dickinson method (Ingersoll et al., 1984). Metamorphic rock fragments were classified according to both composition and metamorphic rank, mainly inferred from degree of recrystallization of mica flakes. The average rank for each sample was expressed by the Metamorphic Index (MI), which varies from 0 in detritus from sedimentary and volcanic cover rocks to 500 in detritus from high-grade basement rocks (Garzanti and Vezzoli, 2003). Very low to low-rank metamorphic lithics, for which protolith can still be inferred, were subdivided into metasedimentary (Lms) and metavolcanic (Lmv) categories. Medium to high-rank metamorphic lithics were subdivided instead into felsic (metapelite, metapsammite, metafelsite; Lmf) and mafic (metabasite; Lmb) categories.

Grain size was determined by ranking and direct measurement in thin section. The analysed Nile Delta sands are mostly upper-fine to medium grained, and range from 170 to 500µm (2.6 to 1µm). Only the Lower Pleistocene sample ND42 is very-fine grained (~ 100µm).

## 3.4 Separation Preparation for Isotope Geochemistry

### 3.4.1 Sample preparation

Sample Separation of Rb, Sr, Sm, Nd, Lu and Hf from bulk rock mud samples was carried out by the author at the NERC Isotope Geoscience Laboratory (NIGL) in Keyworth, supervised by Ian Millar, and assisted by Carlyn Stewart. Samples of Nile delta mud and silt were powdered using a ball mill at the University of Lancaster. Weathering and transport processes can affect the Sr isotope signature of sediments, so similar size fractions (<63 microns) were analysed from each sample in order to exclude the sand fraction. However, in some cases, the < 2µm fraction was separated in order to test the effect of grain size on Sr ratios. In this case, the samples were placed in a 30 ml centrifuge tube with milliQ water, and placed in an ultrasonic bath for several hours to prevent flocculation of clay minerals. The samples were then allowed to settle for a time calculated using Stoke's Law, and the fluid containing the < 2µm fraction in suspension was carefully pipetted off and dried.

### 3.4.2 Weighing and leaching

Calcium carbonate was present in both core and modern Nile catchment samples. 150-200 mg of sample was weighed into 15ml Savillex Teflon beakers, and leached in warm dilute (10%) Romil uPA acetic acid in order to remove carbonate material.  The samples were then centrifuged and the leachate was discarded using a pipette. Samples were then washed in milliQ water and re-centrifuged, transferred back to the Savillex beakers, dried and reweighed.

### 3.4.3 Sample dissolution

Mixed $^{149}$Sm-$^{150}$Nd, $^{176}$Lu-$^{177}$Hf and single $^{84}$Sr and $^{87}$Rb isotope tracers were weighed and added to the samples.   1-2mls of 2x quartz-distilled 16M $HNO_3$ and 5-6 mls of

29M HF were added, and the sample beakers were left closed on a hotplate at 140°C overnight.  After evaporation, a further 1-2 mls of $HNO_3$ were added, and the samples were covered and left on the hotplate overnight.  The samples were then converted to chloride form using 10 mls of 2x quartz-distilled HCl.  The samples were then dissolved in c. 2 ml of 1M HCl + 0.1M HF in preparation for column chemistry and centrifuged.  In some cases, a significant residue remained after dissolution.  This was inspected using an optical microscope, and was found to consist of brown flakes of probable organic material.  Only a few micron-scale crystals of a silver-grey ore mineral were observed.  No garnet, zircon or other hard-to-dissolve rock-forming minerals were seen.

### 3.4.4 Primary column separation

Primary columns consisting of 2 ml of Eichrom AG50x8 cation exchange resin in 10ml Biorad Poly-Prep columns were used to separate bulk high field strength elements (HFSE: Ti, Hf, Zr), a fraction containing Sr, Ca and Rb, and a bulk rare-earth element (REE) fraction.

Samples were loaded onto the columns in c. 1.5 mls of 1M HCl + 0.1M HF, and the HFSE were immediately eluted in 10 mls of 1M HCl + 0.1M HF. This fraction was evaporated to dryness in preparation for separation of Hf. Sr, Ca and Rb were eluted in 30 mls of 1.5M HCl, and evaporated to dryness in preparation for separation of Rb and Sr.  Finally, the REE were eluted in 10 mls of 6M HCl and evaporated to dryness in preparation for separation of Sm, Nd and Lu.

### 3.4.5 Separation of Hf

Hafnium separation followed a procedure adapted from Münker et al. (2001). HFSE concentrates from the primary columns were dissolved in c. 2 mls of 6M HCl and loaded onto 10ml Biorad Poly-Prep columns packed with 1 ml of EICHROM LN-SPEC ion exchange resin. Matrix elements were eluted in 10-20 mls of 6M HCl, and 2 * 2 mls of milliQ water was then passed through the column to remove HCl from the columns prior to subsequent elution steps involving peroxide (mixing of HCl and peroxide would result in immediate elution of HFSE from the columns). The columns were then washed with several 10ml column volumes of a solution containing citric acid, nitric acid and peroxide.  In this medium, titanium citrate complexes show a distinctive bright orange colour, allowing Ti to be quantitatively removed from the column by repeated washing.  Once all traces of Ti were removed from the columns, 5mls of peroxide-free citric acid + nitric acid solution were eluted, again in order to avoid mixing of peroxide with HCl solutions. Zr was then washed from the columns using 50-80 ml of 6M HCl + 0.06M Hf.  Finally, Hf was collected in 10 mls of 6M HCL + 0.2M HCl.

### 3.4.6 Separation of Rb and Sr

The normal procedure for separation of Sr from rock samples at NIGL uses EICHROM Sr-SPEC resin.  However, correction for [87]Rb interference on the [87]Sr peak in the mass spectrometer is problematic for samples spiked with [87]Rb tracer, so it was necessary to ensure a particularly good separation of Rb from Sr.  It was therefore decided to use the more time consuming (but equally 'clean') separation method using EICHROM AG50x8 cation exchange resin.

About 2 mls of sample solution was pipetted onto quartz-glass columns containing 4mls of AG50x8 cation exchange resin, which had been specifically recalibrated to ensure recovery of Rb.  Matrix elements were washed off the column using 26 mls of calibrated 2.5M HCl, and discarded.  Rb was collected in 3 mls of 2.5M HCl.  Ca was then eluted and discarded in 18 mls of 2.5M HCl, before Sr was collected in 12 mls of 2.5M HCl, and evaporated to dryness.

### 3.4.7 Separation of Sm, Nd and Lu from the bulk REE fraction

Sm and Nd were separated using 2mls of EICHROM LN-SPEC ion exchange resin packed into 10ml Biorad Poly-Prep columns.  The bulk REE fraction was dissolved in 200 microlitres of 0.2M HCl and loaded onto the columns.  La, Ce and Pr were eluted using a total of 14mls of 0.2M HCl.  Nd was collected in 3mls of 0.3M HCl and Sm was collected in 3.5mls of 0.6M HCl.  The middle rare-earth elements were eluted in 50 mls of 2.5 M HCl, and finally Lu (+ some residual Yb) was collected in 10 mls of 6M HCl.  Sm, Nd and Lu fractions were evaporated to dryness in preparation for mass spectrometry.

## 3.5 Mass Spectrometry

### 3.5.1 Lu and Hf Analysis

Lu fractions were dissolved in 1 ml of 2% $HNO_3$ prior to analysis on a Thermo-Electron Neptune mass spectrometer, using a Cetac Aridus II desolvating nebuliser.  0.006 l/min of nitrogen were introduced via the nebulizer in addition to argon in order to minimise oxide formation.  The instrument was operated in static multicollection mode, with cups set to monitor $^{176}Er$, $^{177}Er$, $^{172}Yb$, $^{173}Yb$, $^{175}Lu$, $^{176}Lu+Hf+Yb$, $^{177}Hf$ and $^{179}Hf$.  Standard sample cones and X-skimmer cones were

used, giving a typical signal of c. 600 V/ppm Lu. 1% dilutions of each sample were tested prior to analysis, and samples diluted to c. 20ppb prior to the addition of c. 20ppb of Er. Data reduction followed Lapen et al. (2004) using a ratio of 0.6841 for $^{167}Er/^{166}Er$ to correct $^{176}Lu/^{175}Lu$ for mass fractionation. $^{176}Yb$ and $^{176}Hf$ interferences on $^{176}Lu$ were monitored using $^{173}Yb$ and $^{177}Hf$ respectively; $^{176}Yb/^{173}Yb$ and $^{176}Hf/^{177}Hf$ were also corrected for mass bias using $^{167}Er/^{166}Er = 0.6841$ before interference corrections were made. During the period of analysis, Ames Lu (the lutetium standard used) gave a value for $^{176}Lu/^{175}Lu$ of 0.02658 ± 0.00002 (2-sigma, n=59), which lies within analytical uncertainty of the value obtained by Lapen et al. (0.02656 ± 0.00003, 2-sigma). Replicate analysis of the BCR-2 standard across the time of analysis gave a mean Lu concentration of 0.509 ± 0.005 ppm (1-sigma, n=7).

For Hf analysis, fractions were dissolved in 1ml of 2% $HNO_3$ + 0.1M HF prior to analysis on a Thermo-Electron Neptune mass spectrometer, using a Cetac Aridus II desolvating nebuliser. 0.006 l/min of nitrogen were introduced via the nebulizer in addition to argon in order to minimise oxide formation. The instrument was operated in static multi-collection mode, with cups set to monitor $^{172}Yb$, $^{173}Yb$, $^{175}Lu$, $^{176}Lu+Hf+Yb$, $^{177}Hf$, $^{178}Hf$, $^{179}Hf$ and $^{180}Hf$. 1% dilutions of each sample were tested prior to analysis, and samples diluted to c. 20ppb. Standard sample cones and X-skimmer cones were used, giving a typical signal of c. 800-1000 V/ppm Hf. Correction for $^{176}Yb$ on the $^{176}Hf$ peak was made using reverse-mass-bias correction of the $^{176}Yb/^{173}Yb$ ratio empirically derived using Hf mass-bias corrected Yb-doped JMC475 solutions (Nowell and Parrish, 2001). $^{176}Lu$ interference on the $^{176}Hf$ peak was corrected by using the measured $^{175}Lu$ and assuming $^{176}Lu/^{175}Lu = 0.02653$. The column procedure used to separate Hf effectively removes most Yb and Lu, so these

corrections are minimal.  Spike-stripping was carried out using an iterative algorithm.

Data are reported relative to $^{179}$Hf/$^{177}$Hf = 0.7325.

The Hf standard solution JMC475 was analysed during each analytical session and sample $^{176}$Hf/$^{177}$Hf ratios are reported relative to a value of 0.282160 for this standard (Nowell and Parrish, 2001). Across the 18-month period of analysis, 94 analyses of JMC475 gave a mean $^{176}$Hf/$^{177}$Hf value of 0.282148 ± 0.000007 (23.1 ppm, 1-sigma).  Typical external precision for a single day's analysis was in the range between 13-22 ppm.  Replicate analysis of the BCR-2 rock standard run with the samples gave a mean Hf concentration of 4.977 ± 0.021 ppm (1-sigma), and a mean $^{176}$Hf/$^{177}$Hf value of 0.282865 ± 0.000002 (7.7 ppm, 1-sigma, n=5).  Mean Lu/Hf (wt) for BCR-2 was 0.1021 ± 0.0009 (1-sigma).

### 3.5.3 Sm and Nd analysis

Sm fractions were loaded onto one side of an outgassed double Re filament assembly using dilute (0.6M) HCl, and analysed in a Thermo Scientific Triton mass spectrometer in static collection mode. Replicate analysis of the BCR-2 rock standard across the time of analysis gave a mean Sm concentration of 6.34 ± 0.06 ppm (1-sigma, n=7).

Nd fractions were also loaded onto one side of an outgassed double Re filament assembly using 0.6M HCl, and analysed in a Thermo Scientific Triton mass spectrometer.  Nd data were normalised to $^{146}$Nd/$^{144}$Nd = 0.7219.  Samples were analysed in several sessions across a period of 22 months.  Across this period, 19 analyses of the JND-i standard gave a value of 0.512102 ± 0.000005 (10.4 ppm, 1-sigma).  All other standard and sample data is quoted relative to a value of 0.512115

for this standard.  Seven analyses of La Jolla gave 0.511864 ± 0.000006 (11.5 ppm, 1-sigma).  Replicate analysis of the BCR-2 rock standard gave a mean Nd concentration of 28.1 ± 0.3 ppm and $^{143}Nd/^{144}Nd$ = 0.512638 ± 0.000006 (11.9 ppm, 1-sigma, n=12).

### 3.5.5 Rb and Sr analysis

Rb fractions were loaded onto one side of an outgassed double Re filament assembly using dilute (0.6M) HCl, and analysed in a Thermo Scientific Triton mass spectrometer in static multi-collection mode.  Natural Rb standards were analysed to monitor for mass bias (which was negligible given the selected running conditions).  Replicate analysis of the BCR-2 rock standard across the time of analysis gave a concentration 46.9 ± 0.4 ppm.

Sr fractions were loaded onto outgassed single Re filaments using a TaO activator solution, and analysed in a Thermo-Electron Triton mass spectrometer in multi-dynamic mode.  Data were normalised to $^{86}Sr/^{88}Sr$ = 0.1194.  Samples were analysed in several sessions across a period of 22 months.  Across this period, 143 analyses of the NBS987 standard gave a value of 0.710250 ± 0.000006 (9 ppm, 1-sigma).  NBS987 standards analysed with the samples gave a value of 0.710249 ± 0.000004 (6 ppm, 1-sigma, n=14).  This is within analytical uncertainty of the preferred value for this standard (0.710250), so no secondary correction of the data was required.  Replicate analyses of the BCR-2 rock standard run with the samples gave a mean Sr concentration of 340.6 ± 5.1 ppm, and $^{87}Sr/^{86}Sr$ = 0.705041 ± 0.00023 (33 ppm, 1-sigma, n=15).  The calculated Rb/Sr (weight) ratio for BCR-2 is 0.1379 ± 0.0013 (1-sigma).

## 3.6 U-Pb Geochronology – Zircon and Rutile

### 3.6.1 Laser Ablation Plasma Ionisation Mass Spectrometry

Zircon and rutile samples were prepared and analysed at NIGL by the author, supervised by Dr Ian Millar, using a Nu Instruments AttoM single-collector inductively coupled plasma mass spectrometer (SC-ICP-MS). Laser ablation was performed with either a New Wave Research UP193SS or UP193FX laser ablation system. On the UP193FX, an in-house produced low-volume cell is used (see Horstwood et al. (2003) for details), and on the 193SS a two-volume New Wave Research large format cell is used; both of these have a washout to less than 1% of the peak signal in less than one second. Ablation parameters were optimized to suit the Pb and U contents of the material, and in all cases, bracketing reference materials were analysed using the same parameters; these were 5Hz, with a fluence of 1.5 to 3.0 J/cm2, a 30 second ablation time, and a 25 to 35 µm spot size. Laboratory and experimental conditions are listed in Table 3.1.

On the Attom, tuning was adopted that gave ThO and UO of <0.4%. Data processing for all analyses used the time-resolved function on the Nu Instruments' software, an in-house Excel spreadsheet for data reduction and error propagation, and Isoplot 4.15 for data presentation (Ludwig, 2003). Uncertainties were propagated in the manner advocated by Horstwood (2008) and include a contribution from the external reproducibility of a reference material analysed within each session, and a contribution reflecting long-term standard reproducibility, across the 18-month duration of the analytical work. All uncertainty ellipses plotted on Wetherill or Tera-Wasserburg diagrams are at the 2σ confidence level.

The Nu Attom SC-ICP-MS is used in peak-jumping mode with measurement on a MassCom secondary electron multiplier. On the Attom the following masses are measured in each sweep: $^{202}$Hg, $^{204}$Pb+Hg, $^{206}$Pb, $^{207}$Pb, and $^{235}$U (for zircons) or $^{238}$U (for rutile). Each data integration records 100 sweeps of the measured masses, which roughly equates to 0.22 seconds. Dwell times on each mass are 400μs on $^{207}$Pb and $^{235}$U, and 200μs on all other masses; the switching between masses takes 40μs. $^{238}$U (for zircons), or $^{235}$U (for rutile) is calculated using $^{238}$U/$^{235}$U = 137.818.

Three zircon reference materials (91500, GJ-1 and Plesovice) were analysed at regular intervals; the average bias of the $^{207}$Pb/$^{206}$Pb and $^{206}$Pb/$^{238}$U ratios from preferred values derived by TIMS analysis are used for normalization. Accepted ages are presented in Table 3.2.

$^{206}$Pb/$^{238}$U and $^{207}$Pb/$^{206}$Pb uncertainties were propagated in a similar way utilising the measurement uncertainty and the reproducibility of the ablation reference material used. All zircons were CL-imaged prior to laser-ablation work.

Sugluk-4 and PCA-S207 (Bracciali et al., 2013) were analysed as primary and secondary rutile reference materials, respectively.

**Table 3.1** Laboratory and experimental conditions adopted at NIGL, BGS during U-Pb zircon and rutile analysis using LA-ICP-MS.

| | |
|---|---|
| **Laboratory & Sample Preparation** | |
| Laboratory name | NERC Isotope Geosciences Laboratory |
| Sample type/mineral | Zircons and rutile |
| Sample preparation | Conventional mineral separation, 1 inch resin mount, 1μm polish |
| Imaging | CL, 10nA, 16mm working distance |
| **Laser ablation system** | |
| Make, Model & type | ESI/New Wave Research, UP193SS & FX |
| Ablation cell & volume | NWR two-volume 'large format cell', and NIGL low volume cell, both with low effective volume (ca. 3-4cm3), washout ca.1 sec |
| Laser wavelength (nm) | 193nm |
| Pulse width (ns) | 3-4ns |
| Fluence (J.cm-2) | 1.5-3 J.cm-2 |
| Repetition rate (Hz) | 5Hz |
| Ablation duration (secs) | 30secs |
| Ablation pit depth / ablation rate | 16um pit depth, equivalent to 0.08μm/pulse |
| Spot size (μm) | 20-50μm |
| Sampling mode / pattern | Static spot ablation |
| Carrier gas | 100% He, Ar make-up gas |
| Cell carrier gas flow (l/min) | 0.8l/min |
| **ICP-MS Instrument** | |
| Make, Model & type | Nu Instruments Attom SC-SF-ICP-MS |
| Sample introduction. | Free air aspiration of desolvator |
| RF power (W) | 1300W |
| Make-up gas flow (l/min) | 0.7l/min Ar |
| Detection system | Discrete dynode MassCom ion counter |
| Masses measured | 202, 204, 206, 207, (+/- 208), (+/- 232), 235 or 238 |
| Integration time per peak (ms) | ca.200ms |
| Integration time / reading | Ca.1 sec |
| Sensitivity / | Not determined |
| IC Dead time (ns) | 15ns |
| **Data Processing** | |
| Gas blank | 30 second on-peak zero subtracted |
| Calibration strategy | 91500, GJ1, Plesovice (zircon), Sugluk-4 and PCA-5207 (rutile) |
| Reference Material info | 91500 (Wiedenbeck et al 1995); Plesovice (Slama et al., 2008); GJ1 $^{206}$Pb/$^{238}$U 602.3 ± 1Ma, $^{207}$Pb/$^{206}$Pb 609.2 ± 0.7Ma (in-house TIMS). Sugluk-4 (1749 +/- 24 Ma); PCA-5207 (1866 +/- 9 Ma) Bracciali et al. 2013 |
| Data processing package used | Nu Instruments software, in-house spreadsheets |
| Mass discrimination | $^{207}$Pb/$^{206}$Pb and $^{206}$Pb/$^{238}$U normalised to ref. material |
| Common-Pb correction | No common-Pb correction applied to the data |
| Uncertainty level & propagation | Ages in the data table are quoted at 2-sigma absolute, propagation is by quadratic addition. Reproducibility reference material is propagated. |
| Quality control / Validation | See data table for validation results |

### 3.6.2 Data selection strategy

Prior to analyses, zircon and rutile grains were separated using wet separation methods on a Haultain Superpanner, followed by separation using di-iodomethane heavy liquid with a density of 3.3. Magnetic separation was kept to a minimum in order to avoid biasing the mineral populations, and was only used when large concentrations of highly magnetic minerals were present. Because of the complex populations of heavy minerals present (in which zircon and rutile commonly formed a minor proportion), it was not practical to avoid bias by sprinkling the samples onto tape in order to prepare grain mounts. Instead, zircons were hand-picked taking care to select all grains within a particular sub-fraction of the separate. During analysis, where possible, all picked grains were targeted, with no selection due to size, morphology or cathodoluminescence characteristics. The only exception was where clear core-rim relationships could be seen, and zones targeted individually. Grain mount maps were photographed in order to help identify analysis spots and grains that would be used for multiple analyses (e.g. U/Pb and Hf analysis of the same grains). Cathodoluminescence (CL) imaging was used on the Scanning Electron Microscope to image the zircons before analysis. This allowed us to see zonation, radiation damage and cracks in the grains that should be avoided.

After the initial round of analysis (samples from each source and each time period from the delta cone), targeted grain mounts were made and CL was used to screen for ~30Ma grains. From previous work, the younger grains had much higher luminescence (reflecting their low U content) and were usually euhedral with pitting and etching around the edge of the grains.

The screening procedure for zircon analyses is summarised in Table 3.2. Only data that are concordant within the limits defined in Table 3.2 are accepted and plotted in Probability Density plots. An exception is made for young (<60 Ma) grains, which are commonly discordant due to their low U content and relatively high common Pb. The age of these grains was derived by conducting several analyses on each grain, and carefully assessing the resulting data. An example of this process is shown in Figure 3.1. All young grain calculations are presented in Appendix 7.

Parameters for rutile analysis are given in Table 3.3. Because of the relatively high common Pb content of rutile, it was often necessary to derive model ages by regressing each data point through a fixed common Pb composition on a Tera Wasserburg plot.
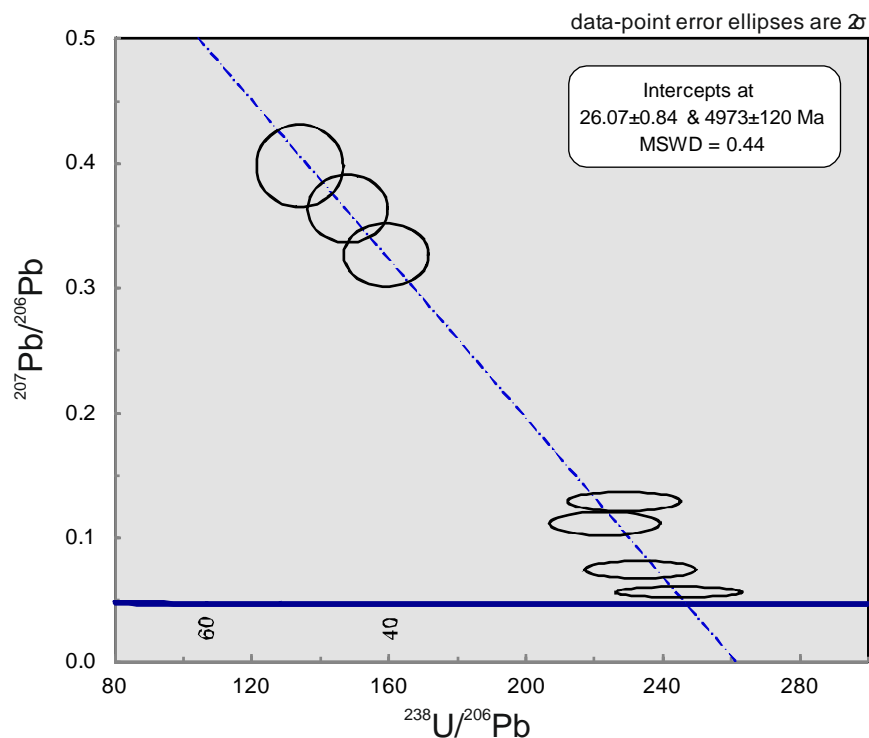


**Figure 3.1.** Tera-Wasserburg plot showing example of calculation of young grain age from multiple analysis. See Appendix 7 for information on the calculation of young ages.

**Table 3.3** Data screening procedure for zircon analysis.

| Zircon Screening Procedure | | |
|---|---|---|
| **1** | Failed | Do Not Use |
| **2** | $^{206}$Pb/$^{238}$U age > 60 Ma, uncertainty >10% | Do Not Use |
| **3** | $^{206}$Pb/$^{238}$U age > 1200 Ma, > 10% discordant | Do Not Use |
| **4** | $^{206}$Pb/$^{238}$U age 60 - 1200 Ma, > 10% discordant | Do Not Use |
| **5** | $^{206}$Pb/$^{238}$U age 60 - 1200Ma, 5-10% discordant | Do Not Use |
| **6** | Young grain - $^{206}$Pb/$^{238}$U age < 60 Ma | Use $^{206}$Pb/$^{238}$U |
| **7** | $^{206}$Pb/$^{238}$U age 60 - 1200Ma , < 5% discordant | Use $^{206}$Pb/$^{238}$U |
| **8** | $^{206}$Pb/$^{238}$U age > 1200 Ma, < 10% discordant | Use $^{207}$Pb/$^{206}$Pb |

**Table 3.4** Data screening procedure for rutile analysis.

| Rutile Screening Procedure | | |
|---|---|---|
| **1** | Failed | Do Not Use |
| **2** | $^{207}$Pb/$^{206}$Pb > 0.5 | Do Not Use |
| **3** | All other data | Accept |
| **4** | If ellipse touches Concordia | $^{206}$Pb/$^{238}$U |
| **5** | If discordant, regress line from common Pb ($^{207}$Pb/$^{206}$Pb = 0.867 ± 0.017 (1-sigma) and calculate age of intercept with concordia) | |

## 3.7 Zircon Hf isotope analysis

Hafnium isotope studies are based on the decay of $^{176}Lu$ to form $^{176}Hf$ (the half-life is about 38 billion years). When the mantle melts to form oceanic crust at mid-ocean ridges, or to create new continental crust above subduction zones, Lu tends to be more compatible than Hf, and is preferentially retained in the mantle. So over the history of the Earth, the depleted mantle develops a higher Lu/Hf ratio than continental crust. In turn, due to the decay of $^{176}Lu$, the depleted mantle develops high $^{176}Hf/^{177}Hf$, while the lower Lu/Hf ratio in continental crust leads to lower $^{176}Hf/^{177}Hf$ ratios.

A positive εHf value indicates that a zircon is derived from a depleted oceanic source (e.g. an island arc) with a relatively high Lu/Hf and $^{176}Hf/^{177}Hf$ ratio. This means that the grain crystallised from melt derived from previously depleted mantle.

A negative εHf value indicates that the zircon has been derived from melting of pre-existing continental crust with relatively low Lu/Hf and $^{176}Hf/^{177}Hf$ ratio. The older the crustal source, the lower will be the εHf value. For example, Archaean cratonic rocks of the Congo-Tanzania craton have present day εHf values as low as -40.

Zircons derived from oceanic rocks and ophiolitic source rocks plot close to this line, due to the depleted nature of the Hf in the source of these rocks. The gradient of the depleted mantle curve shows increasingly more juvenile (positive) values towards the present day and crosses the y axis at εHf = 16.4, which is equivalent to the $^{176}Hf/^{177}Hf$ ratio of modern mid-ocean bridge basalts (0.28325). This reflects the high Lu/Hf ratio of the depleted mantle causing it to increasingly diverge from CHUR through time.

Hf forms an integral part of the zircon lattice (1-2%) and is therefore immobile (Patchett et al., 1981). Also, zircons have very low Lu/Hf ratios, so correction for ingrowth of radiogenic Hf within a crystal is straightforward.  This means that the measured $^{176}Hf/^{177}Hf$ ratio of a zircon can be reliably used to represent the composition of its source magma (and to determine whether it has more crustal or juvenile characteristics). Hf zircon analysis is useful when considering basins where several stages of re-working have occurred (e.g. the Arabian Nubian Shield in the Nile catchment area).

Isotope analyses were carried out at NIGL using a Thermo Scientific Neptune Plus MC-ICP-MS coupled to a New Wave Research UP193FX Excimer laser ablation system and low-volume ablation cell. Helium was used as the carrier gas through the ablation cell with Ar make-up gas being connected via a Y-piece and sourced from a Cetac Aridus II desolvating nebulizer.  Lutetium ($^{175}Lu$), ytterbium ($^{172}Yb$, $^{173}Yb$), and hafnium ($^{176}Hf$, $^{178}Hf$, $^{179}Hf$ and $^{180}Hf$) isotopes were measured simultaneously during static 30 second ablation analyses.  The spot size used was 35 or 50 µm; fluence = 7-10 J/cm$^2$.

Hf reference solution JMC475 was analysed during the analytical session and sample $^{176}Hf/^{177}Hf$ ratios are reported relative to a value of 0.282160 for this standard. Correction for $^{176}Yb$ on the $^{176}Hf$ peak was made using reverse-mass-bias correction of the $^{176}Yb/^{173}Yb$ ratio empirically derived using Hf mass bias corrected Yb-doped JMC475 solutions (Nowell and Parrish, 2001). $^{176}Lu$ interference on the $^{176}Hf$ peak was corrected by using the measured $^{175}Lu$ and assuming $^{176}Lu/^{175}Lu = 0.02653$.

At least two zircon reference materials (91500, Mud Tank and on occasion, Plesovice and Zr144 standard glass) were analysed throughout the analytical session. Lu-Hf data for samples and standards are presented in Appendix 6.   The 91500 zircon reference material was used to normalise the $^{176}$Lu/$^{177}$Hf ratio assuming a value of 0.000311 (Woodhead and Hergt, 2005).

Analytical uncertainties for unknowns were propagated by quadratic addition to include the standard error of the mean of the analysis and the reproducibility of the 91500 reference material. εHf values were calculated using a $^{176}$Lu decay constant of 1.867 x 10-11y$^{-1}$ (Söderlund et al., 2004), the present-day chondritic $^{176}$Lu/$^{177}$Hf value of 0.0336 and $^{176}$Hf/$^{17}$7Hf ratio of 0.282785 (Bouvier et al., 2008).

Latterly, the Hf-isotope data was processed using the Iolite data reduction package (www.iolite.org.au).  Standard data is summarised in Lu/Hf Zircon, Appendix 9.

## 3.8 Ar/Ar Analysis of Plagioclase and Mica (SUERC)

Ar/Ar analysis of plagioclase feldspar and biotite mica is a geochronological technique often used in provenance studies. It is used in this study to evaluate the absence or presence of different provenance sources in the Nile Cone sedimentary record. The technique is underpinned by the principle that $^{40}$K naturally decays to $^{40}$Ar (Beckinsale., 1969). The age determined for each analysis represents the time since crystallisation of each grain, and relies on the fact that radiogenic argon resulting from the decay of 40K remains trapped in the grain.

**Sample preparation and analyses**

Modern river and Nile cone samples were powdered in Lancaster University.

Minerals were picked at Lancaster University and NIGL, before being sent to the

Scottish Universities Environmental Research Centre in East Kilbride, where analyses

were carried out by Dan Barfod. Samples and neutron flux monitors were placed in

aluminium discs and stacked in quartz tubes. The relative positions of wells in the

discs were precisely measured for later reconstruction of neutron flux gradients. The

sample package was irradiated in the Oregon State University reactor, Cd-shielded

facility. Fish Canyon Sanidine (28.294 Ma (Renne et al., 2011) was used to monitor

$^{39}$Ar production and establish neutron flux values (J) for the samples.  The neutron

flux within a given disc is calculated by least-squares fitting of a surface to the J-

monitors.  Estimated errors in the neutron flux measurements are calculated from

the residual deviation from the fitted surface.

Gas was extracted from samples using a mid-infrared $CO_2$ laser, with samples housed

in a ZnS-window laser cell.  Individual sample grains were loaded into a steel

planchette containing 208 2mm diameter wells. Liberated argon was then purified of

active gases (e.g., $CO_2$, $H_2O$, $H_2$, $N_2$, $CH_4$) using three Zr-Ti-Al getters; one at 25°C and

two at 400°C.  Data were collected on a GVi instruments ARGUS 5-collector mass

spectrometer using a variable sensitivity faraday collector array in static collection

(non-peak hopping) mode (Mark et al., 2009; Sparks et al., 2008). Time-intensity data

are regressed to $t_0$ with second-order polynomial fits to the data.  Mass

discrimination was monitored by comparison to running-average values of an air

standard ($^{40}$Ar/$^{36}$Ar$_{ATM}$=298.56±0.31, 1).  The average total system blank for laser

extractions, measured between each sample run, was $1\times10^{-15}$ mol $^{40}$Ar, $3\times10^{-17}$ mol $^{39}$Ar, $3\times10^{-18}$ mol $^{36}$Ar.

All data are blank, interference and mass discrimination corrected using the Massspec software package (authored by Al Deino, BGC).

| Locality | Location | N | E | River/Wadi | Environment | Samples | Sample Type |
|----------|----------|---|---|------------|-------------|---------|-------------|
| **Ethiopia** | | | | | | | |
| ETH01 | Blue Nile Gorge | 10'04'40.2 | 038'11.35.4 | Blue Nile | Fluvial | ETH01A<br>ETH01B | Modern river sand<br>Modern river mud |
| ETH02 | Arranja Bridge | 10'58'06.3 | 035'1106.7 | Blue Nile | Fluvial | ETH02A<br>ETH02B | Modern river sand<br>Modern river mud |
| ETH03 | Blue Nile Falls | 11'29'17.8 | 037'35'41.7 | Blue Nile | Fluvial | ETH03A<br>ETH03B | Modern river sand<br>Modern river mud |
| ETH04 | Kechin Abeba | 11'57'30.7 | 039'00'40.2 | Tekeze | Fluvial | ETH04A<br>ETH04B | Modern river sand<br>Modern river mud |
| ETH05 | Merishet River | 12'15'40.3 | 039'01'51.2 | Tekeze | Fluvial | ETH05A<br>ETH05B | Modern river sand<br>Modern river mud |
| ETH06 | River Gibai | 13'36'00.7 | 039'22'45.0 | Tekeze | Fluvial | ETH06A<br>ETH06B | Modern river sand<br>Modern river mud |
| ETH07 | Aserte Bridge | 13'50'47.6 | 039'00'11.6 | Uri | Fluvial | ETH07A<br>ETH07B | Modern river sand<br>Modern river mud |
| ETH08 | Malemin Bridge | 13'44'09.8 | 038'11'52.9 | Tekeze | Fluvial | ETH08A<br>ETH08B | Modern river sand<br>Modern river mud |
| **Red Sea Hills (Egypt)** | | | | | | | |
| RSH01 | Wadi Tarfa | 28 21'39.5" | 031 07'32.3" | Tarfa | Point Bar | RSH01A<br>RSH01B | Modern wadi sand<br>Modern wadi mud |
| RSH02 | Wadi Qena | 28 02'45.8" | 032 28'58.4" | Qena | Fluvial | RSH02A | Bedrock sandstone (Jurassic) |
| RSH03 | Wadi Umm Omeiyid | 27 40'10.7" | 032 34'34.2" | Qena | Fluvial | RSH03A<br>RSH03B | Modern wadi sand<br>Modern wadi mud |

| Locality | Location | N | E | River/Wadi | Environment | Samples | Sample Type |
|---|---|---|---|---|---|---|---|
| RSH04 | N. Wadi Qena | 27 40'11.4" | 032 34'20.2" | Qena | Marine? | RSH04A | Bedrock sandstone (Lower Cretaceous) |
| RSH05 | Central Wadi Qena | 26 59'53.4" | 032 44'55.6" | Qena | Point Bar | RSH05A RSH05B | Modern wadi sand Modern wadi mud |
| RSH06 | South Wadi Qena | 26 07'23.7" | 033 09'39.8" | Qena | Marine? | RSH06A RSH06B | Bedrock sandstone (Nubian) Bedrock mudstone (Nubian) |
| RSH07 | Wadi Hammamat (S) | 25 45'43.5" | 033 18'09.9" | Hammamat | Point Bar | RSH07A RSH07B | Modern wadi sand Modern wadi mud |
| RSH08 | Near. Wadi Kharit | 23 50'26.2" | 033 31'39.7" | Kharit | Fluvial | RSH08A RSH08B | Bedrock sandstone (Nubian) Bedrock mudstone (Nubian) |
| RSH09 | Wadi Kharit | 24 12'40.5" | 033 20'52.1" | Kharit | Fluvial | RSH09A | Bedrock sandstone (Nubian) |
| RSH10 | Wadi.Kharit tributary | 24 13'39.1 | 033 31'24.3" | Kharit | Fluvial | RSH10A RSH10B RSH10C | Modern wadi sand Modern wadi mud Aeolian sand |
| RSH11 | Wadi Kharit main | 24 36'35.6" | 033 40'55.2" | Kharit | Point Bar | RSH11A RSH11B | Modern wadi sand Modern wadi mud |
| RSH12 | Wadi Abbad | 25 04'36.6" | 033 06'32.7" | Abbad | Point Bar | RSH12A RSH12B | Modern wadi sand Modern wadi mud |
| RSH13 | Wadi Umm Tihe | 25 10'50.3" | 033 09'10.8" | Abbad | Point Bar | RSH13A RSH13B | Modern wadi sand Modern wadi mud |

| Locality | Location | N | E | River/Wadi | Environment | Samples | Sample Type |
|---|---|---|---|---|---|---|---|
| | | | | | | RSH13B | Modern wadi mud |
| RSH14 | Wadi Hammamat | 25 58'03.5" | 033 32'38.3" | Hammamat | Breccia | RSH14A | Bedrock (Neoproterozoic) |
| | | | | | | RSH14B | Modern wadi mud |
| RSH15 | Near Wadi Hammamat | 26 08'80.4" | 033 57'10.9" | Hammamat | Fluvial | RSH15A | Modern wadi sand |
| | | | | | | RSH15B | Modern wadi mud |
| | | | | | | RSH15C | Modern wadi sand (fine) |
| RSH16 | Wadi Umm Gehir | 26 43'52.0" | 033 52'27.8" | Nr. Safaga | Fluvial | RSH16A | Modern wadi sand (fine) |
| | | | | | | RSH16B | Modern wadi mud |
| | | | | | | RSH16C | Modern wadi sand (coarse) |
| *Sudan* | | | | | | | |
| SD01 | South Aulia | 14°59'31.7" | 032°26'48.2" | White Nile | Fluvial | SD01A | Modern river sand |
| | | | | | | SD01B | Modern river mud |
| SD02 | Esh Shawal | 13°31'17.7" | 032°38'18.2" | White Nile | Fluvial | SD02A | Modern river sand |
| | | | | | | SD02B | Modern river mud |
| SD03 | Wad Madani | 14°18'17.1" | 33°34'8.40" | Blue Nile | Fluvial | SD03A | Modern river sand |
| | | | | | | SD03B | Modern river mud |
| SD04 | Al Beere | 21°20'47.5" | 030°55'13.7" | Nile Trunk | Fluvial | SD04A | Modern river sand |
| | | | | | | SD04B | Modern river mud |
| SD05 | Abu Hamad | 19°22'27.2" | 033°22'51.6" | Nile Trunk | Fluvial | SD05A | Modern river sand |
| | | | | | | SD05B | Modern river mud |
| SD06 | Atbara | 17°41'07.9" | 034°00'52.7" | Atbara | Fluvial | SD06A | Modern river sand |

| Locality | Location | N | E | River/Wadi | Environment | Samples | Sample Type |
|---|---|---|---|---|---|---|---|
| | | | | | | SD06B | Modern river mud |
| ***Western Desert (Egypt)*** | | | | | | | |
| WD03 | The Great Sand Sea | 26°59'4.70"N | 25°14'5.20"E | | Aeolian | WD03c | Aeolian sand |
| WD04 | Silica Glass Area | 25°45'27.10"N | 25°15'25.30"E | | Aeolian | WD04C | Aeolian sand |
| WD05 | West of Silica Glass | 25°34'58.10"N | 25° 9'21.70"E | | Fluvial | WD05a | Bedrock sandstone (Upper Cretaceous) |
| WD06 | Diesel Depot | 24°55'21.60"N | 25°46'34.20"E | | Fluvial | WD06a | Bedrock sandstone (Upper Cretaceous) |
| WD07 | South of Great Sand Sea | 25° 8'15.70"N | 25°36'20.20"E | | Aeolian | WD07c | Aeolian sand |
| WD08 | NW of Gilf Kebir | 24°18'15.66"N | 25°42'28.10"E | | | WD08b | Bedrock mudstone (Upper Cretaceous) |
| WD09 | South-east of Silica Glass | 24°47'22.30"N | 25°26'29.40"E | | Fluvial | WD09a | Bedrock sandstone (Upper Cretaceous) |
| | | | | | | WD09b | Bedrock mudstone (Upper Cretaceous) |
| WD10 | North of Wadi Tahl | 24°36'48.80"N | 25°22'23.30"E | N. of Wadi Tahl | Fluvial | WD10C | Aeolian sand |
| WD11 | NW of Gilf Kebir | 24°56'0.90"N | 25°37'56.00"E | | | WD11b | Modern wadi mud |
| WD12 | Wadi Tahl | 24° 3'52.10"N | 25°10'27.60"E | Wadi Tahl | Fluvial | WD12a | Bedrock sandstone (Palaeozoic) |
| | | | | | | WD12b | Bedrock mudstone (Palaeozoic) |
| WD13 | Cave of the Swimmers | 23°39'2.08"N | 25° 9'49.60"E | | Fluvial | WD13a | Bedrock sandstone (Palaeozoic) |

| Locality | Location | N | E | River/Wadi | Environment | Samples | Sample Type |
|---|---|---|---|---|---|---|---|
| WD14 | Uweinat, Sudan | 21°59'27.20"N | 25° 7'49.00"E | | Fluvial | WD14a | Bedrock sandstone (Cambrian) |
| | | | | | | WD14b | Bedrock mudstone (Cambrian) |
| WD15 | North of Uweinat | 22°38'15.20"N | 25°32'25.70"E | | | WD15a | Granite |
| WD16 | Kalashnikov Gneiss | 22° 5'1.40"N | 25°45'12.20"E | | | WD16a | Gneiss |
| WD17 | Eight Bells | 22°25'36.30"N | 26°16'19.70"E | | Fluvial | WD17a | Bedrock sandstone (Palaeozoic) |
| WD18 | Wadi Wassa | 23°12'16.50"N | 26°16'36.40"E | Wadi Wassa | Fluvial | WD18a | Mesozoic Sandstone |
| | | | | | | WD18aa | Mesozoic Sandstone |
| WD19 | Near Dakhla Oasis | 25°10'38.50"N | 27°24'42.90"E | | Aeolian | WD19c | Aeolian sand |
| WD20 | Near Frafra Oasas | 26°14'39.00"N | 27°35'10.00"E | | Aeolian | WD20c | Aeolian sand |
| *Uganda* | | | | | | | |
| N7-17 | Murchison Falls | 02°16'38.1" | 031°41'12.9" | White Nile | Fluvial | N7-17 | Modern river sand |
| N7-16 | Itanda Falls | 02°43'25.47" | 031°26'36.11" | White Nile | Fluvial | N7-16 | Modern river sand |
| *Other* | | | | | | | |
| 11 | Kom Ombo | Collected by Shukri 1950 | | Pre-Dam Nile | Fluvial | 11 | Modern river sand |
| 46 | Aswan | Collected by Shukri 1950 | | Pre-Dam Nile | Fluvial | 46 | Modern river sand |

| Locality | Location | N | E | River/Wadi | Environment | Samples | Sample Type |
|---|---|---|---|---|---|---|---|
| 47 | Luxor | Collected by Shukri 1950 | | Pre-Dam Nile | Fluvial | 47 | Modern river sand |
| 49 | Minya | Collected by Shukri 1950 | | Pre-Dam Nile | Fluvial | 49 | Modern river sand |
| 51 | Cairo | Collected by Shukri 1950 | | Pre-Dam Nile | Fluvial | 51 | Modern river sand |
| S1984 | Wadi Qasab | Collected by E. Garzanti | | Wadi Qasab | | S1984 | Modern wadi sand |
| S1989 | Wadi Qena | Collected by E. Garzanti | | Wadi Qena | | S1989 | Modern wadi sand |
| S1990 | Safaga | Collected by E. Garzanti | | | | S1990 | Modern wadi sand |
| S2408 | Aswan | Collected by E. Garzanti | | | | S2408 | Modern wadi sand |
| S3001 | Wadi Kharit | Collected by E. Garzanti | | Wadi Kharit | | S3001 | Modern wadi sand |

**Table 3.3** Samples collected from the modern Nile catchment area as part of this study.

| Sample No. | Age (Ma) | Stratigraphic Age | Lithology Type |
|---|---|---|---|
| **Holocene** | | | |
| NDM36 | 0 | Holocene | Mud |
| NDM37 | 0 | Holocene | Mud |
| **Pleistocene** | | | |
| ND41 | 1.295 | Early Pleistocene | Medium sand |
| ND42 | 1.295 | Early Pleistocene | Medium sand |
| NDM33 | 1.295 | Early Pleistocene | Mud |
| NDM34 | 1.295 | Early Pleistocene | Mud |
| NDS1 | 1.295 | Early Pleistocene | Silt |
| NDS2 | 1.295 | Early Pleistocene | Silt |
| **Pliocene** | | | |
| ND01 | 2.65 | Piacenzian | Medium sand |
| ND02 | 2.65 | Piacenzian | Medium sand |
| ND03 | 2.65 | Piacenzian | Medium sand |
| ND04 | 2.65 | Piacenzian | Medium sand |
| ND05 | 2.65 | Piacenzian | Medium sand |
| ND06 | 2.65 | Piacenzian | Medium sand |
| ND44 | 2.65 | Piacenzian | Medium sand |
| NDC03 | 2.65 | Piacenzian | Clasts |
| NDC04 | 2.65 | Piacenzian | Clasts |
| NDC05 | 2.65 | Piacenzian | Clasts |
| NDM01 | 2.65 | Piacenzian | Mud |
| NDM16 | 2.65 | Piacenzian | Mud |
| NDM02 | 2.65 | Piacenzian | Mud |
| NDM23 | 2.65 | Piacenzian | Mud |
| NDM24 | 2.65 | Piacenzian | Mud |
| NDM03 | 2.65 | Piacenzian | Mud |
| NDM04 | 2.65 | Piacenzian | Mud |
| NDM05 | 2.65 | Piacenzian | Mud |
| NDM06 | 2.65 | Piacenzian | Mud |
| NDM07 | 2.65 | Piacenzian | Mud |
| NDM08 | 2.65 | Piacenzian | Mud |
| NDM09 | 2.65 | Piacenzian | Mud |
| NDS12 | 2.65 | Piacenzian | Silt |
| NDS13 | 2.65 | Piacenzian | Silt |

| | | | |
|---|---|---|---|
| NDS14 | 2.65 | Piacenzian | Silt |
| NDS15 | 2.65 | Piacenzian | Silt |
| NDS16 | 2.65 | Piacenzian | Silt |
| NDS17 | 2.65 | Piacenzian | Silt |
| NDS18 | 2.65 | Piacenzian | Silt |
| NDM10 | 2.78 | Piacenzian | Mud |
| ND08 | 2.78 | Piacenzian | Medium sand |
| ND09 | 2.78 | Piacenzian | Medium sand |
| NDC02 | 2.78 | Piacenzian | Clasts |
| NDM11 | 2.78 | Piacenzian | Mud |
| NDM12 | 2.78 | Piacenzian | Mud |
| NDM13 | 2.78 | Piacenzian | Mud |
| NDM14 | 2.78 | Piacenzian | Mud |
| NDM15 | 2.78 | Piacenzian | Mud |
| NDS10 | 2.78 | Piacenzian | Silt |
| NDS11 | 2.78 | Piacenzian | Silt |
| NDS08 | 2.78 | Piacenzian | Silt |
| NDS09 | 2.78 | Piacenzian | Silt |
| NDM17 | 2.78 | Piacenzian | Mud |
| NDM18 | 2.78 | Piacenzian | Mud |
| NDM20 | 2.78 | Piacenzian | Mud |
| NDM21 | 2.78 | Piacenzian | Mud |
| NDM22 | 2.78 | Piacenzian | Mud |
| NDS05 | 2.79 | Piacenzian | Silt |
| NDS06 | 2.79 | Piacenzian | Silt |
| ND43 | 3.2 | Piacenzian | Medium sand |
| NDS07 | 3.2 | Piacenzian | Silt |
| ND07 | 3.25 | Piacenzian | Medium sand |
| NDC1 | 3.25 | Piacenzian | Clasts |
| NDS3 | 3.25 | Piacenzian | Silt |
| **Miocene** | | | |
| ND27 | 15.2 | Langhian | Medium sand |
| ND28 | 15.2 | Langhian | Medium sand |
| ND29 | 15.2 | Langhian | Medium sand |
| ND30 | 15.2 | Langhian | Medium sand |
| ND31 | 15.2 | Langhian | Medium sand |
| NDM29 | 15.2 | Langhian | Mud |

| | | | |
|---|---|---|---|
| NDM30 | 15.2 | Langhian | Mud |
| NDS32 | 15.2 | Langhian | Silt |
| NDS33 | 15.2 | Langhian | Silt |
| ND14 | 15.5 | Langhian | Medium sand |
| ND15 | 15.5 | Langhian | Medium sand |
| ND16 | 15.5 | Langhian | Medium sand |
| ND17 | 15.5 | Langhian | Medium sand |
| ND18 | 15.5 | Langhian | Medium sand |
| ND19 | 15.5 | Langhian | Medium sand |
| ND20 | 15.5 | Langhian | Medium sand |
| ND21 | 15.5 | Langhian | Medium sand |
| ND22 | 15.5 | Langhian | Medium sand |
| ND23 | 15.5 | Langhian | Medium sand |
| ND24 | 15.5 | Langhian | Medium sand |
| ND25 | 15.5 | Langhian | Medium sand |
| ND26 | 15.5 | Langhian | Medium sand |
| NDM27 | 15.5 | Langhian | Mud |
| NDM28 | 15.5 | Langhian | Mud |
| NDS20 | 15.5 | Langhian | Silt |
| NDS21 | 15.5 | Langhian | Silt |
| NDS22 | 15.5 | Langhian | Silt |
| NDS23 | 15.5 | Langhian | Silt |
| NDS24 | 15.5 | Langhian | Silt |
| NDS25 | 15.5 | Langhian | Silt |
| NDS26 | 15.5 | Langhian | Silt |
| NDS27 | 15.5 | Langhian | Silt |
| NDCu13 | ? | Langhian | Cuttings |
| ND10 | 17 | Burdigalian | Medium sand |
| ND11 | 17 | Burdigalian | Medium sand |
| ND12 | 17 | Burdigalian | Medium sand |
| ND13 | 17 | Burdigalian | Medium sand |
| NDM25 | 17 | Burdigalian | Mud |
| NDM26 | 17 | Burdigalian | Mud |
| NDS28 | 17 | Burdigalian | Silt |
| NDS29 | 17 | Burdigalian | Silt |
| NDS30 | 17 | Burdigalian | Silt |
| NDS31 | 17 | Burdigalian | Silt |

**Oligocene**

| | | | |
|---|---|---|---|
| ND32 | 27.5 | Chattian | Medium sand |
| ND33 | 27.5 | Chattian | Medium sand |
| ND45 | 27.5 | Chattian | Medium sand |
| NDCu5 | 27.5 | Chattian | Cuttings |
| NDM31 | 27.5 | Chattian | Mud |
| NDS34 | 27.5 | Chattian | Silt |
| ND34 | 31 | Rupelian | Medium sand |
| ND35 | 31 | Rupelian | Medium sand |
| ND36 | 31 | Rupelian | Medium sand |
| ND37 | 31 | Rupelian | Medium sand |
| ND38 | 31 | Rupelian | Medium sand |
| ND39 | 31 | Rupelian | Medium sand |
| ND40 | 31 | Rupelian | Medium sand |
| ND46 | 31 | Rupelian | Medium sand |
| NDM32 | 31 | Rupelian | Mud |
| NDS35 | 31 | Rupelian | Silt |
| NDCu01 | 27.5 | Chattian | Cuttings |
| NDCu10 | 27.5 | Rupelian | Cuttings |
| NDCu11 | 31 | Rupelian | Cuttings |
| NDCu02 | 27.5 | Chattian | Cuttings |
| NDCu03 | 27.5 | Chattian | Cuttings |
| NDCu04 | 27.5 | Chattian | Cuttings |
| NDCu06 | 27.5 | Chattian | Cuttings |
| NDCu07 | 27.5 | Chattian | Cuttings |
| NDCu08 | 27.5 | Chattian | Cuttings |
| NDCu09 | 27.5 | Chattian | Cuttings |
| NDCu12 | 31 | Rupelian | Cuttings |

**Table 3.4** Nile Cone core samples collected as part of this study during visits to BP Egypt, Cairo.  Note that the location of sampled wells is subject to embargo by BP Egypt.

# Chapter 4: A detrital record of Nile hinterland evolution

Laura Fielding[1], Yani Najman[1], Ian Millar[2], Peter Butterworth[3], Sergio Ando [4], Marta Padoan[4], Dan Barfod[5] & Ben Kneller[6]

*1. Lancaster Environment Centre, Lancaster University, Lancaster, U.K.; 2. British Geological Survey, Keyworth, U.K.; 3. BP Egypt, Cairo; 4. University Milano-Biccoca, Milan, Italy; 5. SUERC, East Kilbride, U.K.; 5. University of Aberdeen, Aberdeen*.

## Abstract

We present detrital mineral and bulk-rock analyses of modern river, wadi and bedrock samples, in order to assess the role of basement lithology, sedimentary recycling, and modern geomorphological features on the composition of sediment reaching the Nile delta. Our combined U-Pb and Hf-isotope zircon dataset, heavy mineral analyses, and trace element data document the evolution of the North African crust, in particular highlighting phases in the development of the Arabian Nubian Shield (ANS) and amalgamation of Gondwana in Late Neoproterozoic times.

New U-Pb and Hf-isotope data for Archaean basement of the Saharan Metacraton, together with detrital zircons derived from the Congo Craton in northern Uganda, indicate a common history of crustal growth, with new crust formation at 3.0-3.5 Ga, and crustal melting at c. 2.7 Ga.

We consider the maximum depositional age of the Neoproterozoic Hammamat Group of the ANS to be 630 Ma, based on the age of the youngest zircon population. The sediments are locally derived and were deposited in an intra-arc setting before the suturing of the Saharan Metacraton and ANS.

The bulk provenance signature of the modern Nile is dominated by the input of basic detritus from the Ethiopian Volcanic Province. Detrital zircon signatures are dominated by variations in bedrock lithology, and the availability of easily-eroded Phanerozoic cover sediments. These represent an important source of detritus to the river and are characterised by the presence of strongly negative εHf populations at c. 600 and 1000 Ma, and significant (9-12%) populations of pre-Neoproterozoic zircon

grains.  The highest proportions of pre-Neoproterozoic grains in the modern river are

seen in the Nile trunk in Egypt.

Modern geomorphological features are also important.  The composition of White

Nile sediment varies dramatically across the Sudd marshes as a result of sediment

trapping, with little or no material derived from the Congo craton reaching the White

Nile in Sudan, where locally derived sediment from Phanerozoic cover is dominant.

The White Nile immediately south of Khartoum is affected by its proximity to the

Gezira fan and receives an influx of Blue Nile sediment during times of peak flow.

## 4.1 Introduction

Modern river sediments can be used to efficiently sample large areas of upstream crust in order to determine a region's geological history (e.g. Iizuka et al., 2013). In this study, we use a range of provenance techniques, including U-Pb and Hf isotope analysis of zircon from river sands, and Sr-Nd-Hf tracer isotope analysis of river mud samples, in order to characterise the catchment of the modern Nile River. Our aims are to gain a broad overview of the geological evolution of NE Africa, and also to constrain the potential sources of sediment to the Nile delta cone, an important depocentre for hydrocarbon reservoirs.

We report data for sand and mud samples from the Nile trunk, and its tributaries the Blue Nile, White Nile and Atbara, together with samples from dry wadis in the Red Sea Hills and Egyptian Western Desert, which represent possible sources of detritus to the river. We have also studied fluvial, deltaic and marine sandstones that have draped NE Africa since the latest Precambrian, and which represent an important source of detritus to the river. We present zircon U-Pb and Hf-isotope data for gneissic basement within the Saharan Metacraton, which is poorly documented. This data helps to characterise the nature of the Archaean crust of North Africa.

Our data document early crust-forming events, Precambrian orogenies culminating in the Neoproterozoic assembly of Gondwana, subsequent erosion and deposition of voluminous flysch deposits, and finally Cenozoic uplift of the Highlands and eruption of continental flood basalts in Ethiopia. Additionally, our data track the influence of topography and local geology on the progressive evolution of the Nile sedimentary signal downstream.

The Nile River is the longest river in the world, extending for more than 6,800 km,

and draining an area of ~3.3 million km$^2$. The present-day Nile is made up of three

main tributaries, the Blue Nile, White Nile and Atbara (Figure 4.1). The mean annual

water discharge during times of peak flow is dominated by the Blue Nile (68%),

followed by the White Nile (10%) and Atbara (22%) (Williams and Adamson, 1982).

Sediment supplied to the Nile trunk in Egypt is dominated by contributions from the

Blue Nile (50-61%) and Atbara (30-42%) (Padoan et al., 2011). The vast majority of

the White Nile sediment load is trapped in extensive swamps in South Sudan (the

Sudd marshes, Figure 4.1), accounting for <3% of the total Nile sediment budget

(Padoan et al., 2011).

The White Nile drains Archaean – Proterozoic rocks of the Congo and Tanzania

Cratons, and extends through Precambrian rocks of the Saharan Metacraton

(Abdelsalam, 2002) in South Sudan. In its terminal tract, the White Nile has an

extremely low gradient due to its positioning along the floor of an ancient lake that

occupied its valley as long ago as 400 ka before present (Williams et al., 2003). The

present flow regime of the Nile was established in the late Pleistocene, at c.15 ka,

when northwards flow was reinitiated due to intensification of the summer monsoon

and resulting overflow of Lakes Albert and Victoria (Talbot et al., 2000; Williams et

al., 2003).

The Blue Nile and Atbara, together with its tributary the Tekeze are sourced in the

Ethiopian Highlands, where they drain Cenozoic flood basalts (e.g. Pik et al., 1998),

Neoproterozoic Arabian-Nubian Shield basement rocks (e.g. Evuk et al., 2014;

Johnson, 2014) and Phanerozoic cover sequences (e.g. Gani et al., 2009). Uplift of

the Ethiopian Highlands in the Oligocene may have led to the initiation of flow in the Blue Nile. However, there is no consensus in published literature about the timing of initiation of such flow.

Proponents of Oligocene initiation of sediment supply from the Ethiopian plateau have used knick-point facies (the point at which a river down-cuts due to uplift) to infer a 3-phase incision in the Ethiopian Highlands at 29-10 Ma, 10-6 Ma and 6 Ma, which instigated erosion in the Tekeze, Atbara and Blue Nile catchments (Gani et al., 2007). Thermochronological studies using apatite and titanite He ages suggest that the elevated plateau physiography, which controls most of the present-day Nile hydrology, has existed since the Oligocene, ca.29 Ma (Pik et al., 2003), whilst authors favouring a  Nile drainage originating in the Late Miocene cite sparse remotely sensed radar data to argue for a south-draining 'Qena System' dominating the Nile valley until the Messinian Salinity Crisis (Issawi and McCauley, 1992). Sediment volume calculations of the delta cone have been used to infer that a connection with the Ethiopian Highlands did not occur until the Pleistocene (Macgregor, 2012; Palacios, 2013).

The Red Sea Hills, to the east of the present day Nile trunk, drain ANS basement and Phanerozoic sediments which are comprised of Palaeozoic and Mesozoic sediments and Eocene carbonates (Figure 4.1). Although not drained by the Nile at present, the Western Desert is thought to have once contributed detritus to the main Nile trunk (e.g. Issawi and McCauley, 1992). It comprises reworked pre-Neoproterozoic crust of the Saharan Metacraton, and overlying Phanerozoic sedimentary successions (Figure 4.1).

**Figure 4.1 Modern river samples and hinterland geology of Nile river source areas.** Inset shows location of map as boxed area. Map modified from (al-Miṣrīyah, 1981; Johnson, 2014; Kazmin, 1972; Ministry of Energy and Mines, 1981).

## 4.2 Geology of the Nile catchment

Phanerozoic cover sediments, such as the Nubian sandstone, blanket much of north east Africa. Beneath these, basement rocks record the collision of east and west Gondwana during the Pan-African Orogeny towards the end of the Neoproterozoic (Figure 4.1). During this time, juvenile ocean island arcs of the Arabian Nubian Shield amalgamated with Archaean cratons such as the Congo and Tanzania cratons and the Saharan Metacraton. It was not until the Cenozoic that uplift of the Ethiopian Highlands and the eruption of Continental Flood Basalts led to the formation of one of the Niles most influential source areas and the initiation of the Blue Nile.

### 4.2.1 Precambrian cratons

Each of the major African cratons is outlined below, the location of which is illustrated in Figure 4.1.

The Congo craton (Figure 4.1) forms part of the West-African-Central-Belt which formed between 2.0 and 3.0 Ga ago and comprises orthogenesis, metasediments and granitoids of the Gabon-Kamerun Shield, Bomu-Kibalian Shield, Kasai Shield and the Angolan Shield (Cahen et al., 1984; Goodwin, 1996; Tchameni et al., 2000; Walraven and Rumvegeri, 1993).

The Tanzania craton (Figure 4.1) covers an area of over 3,500,000 km$^2$ with an average elevation of 1260m (Cahen et al., 1984) and lies to the east of the Congo Craton. It is almost entirely composed of granitoids and greenstone belts, with emplacement ages of c. 2700 Ma, and positive εNd values, suggesting derivation from a mantle source without significant involvement of older crust (De Waele et al., 2008).

The term Saharan Metacraton (Figure 4.1) refers to an area of pre-Neoproterozoic continental crust which has, in part, been highly remobilised during the Pan-African orogeny (Abdelsalam, 2002). It covers an area of 5,000,000 km$^2$ and extends from the Arabian Nubian Shield in the east to the Tuareg Shield in the west and the Congo Craton in the south. More than 50% of the Saharan Metacraton is overlain by Phanerozoic 'Nubian' sedimentary rocks and desert sands (Abdelsalam et al., 2011). The poor exposure of the region means that the Saharan Metacraton, and its relationship to adjacent blocks, is poorly understood. The southern boundary is not well defined, but is taken to be marked by the Oubangides orogenic belt which separates it from the Congo-Tanzania Craton (Abdelsalam, 2002). Little modern geochronology has been carried out on rocks of the Saharan Metacraton. Legacy Rb-Sr and U-Pb data quoted by Abdelsalam (2002) indicate a range of late Archaean and Palaeoproterozoic  protolith ages, with significant cratonic reworking and addition of new crust in the Neoproterozoic. Bea et al. (2011) report SHRIMP U-Pb zircon ages as old as 3.22 ± 0.04 Ga for gneisses in the Uweinat and Gebel Kamil regions of the Western Desert in southernmost Egypt.

### 4.2.2 The Arabian Nubian Shield

To the west of the ancient African cratons lies the Arabian Nubian Shield. It a collage of Neoproterozoic (c. 870-670 Ma) continental margin and juvenile island arcs, overlain by younger sedimentary and volcanic basins, and cut by voluminous granitoid intrusions (Johnson and Woldehaimanot, 2003; Kusky and Matsah, 2003; Stern, 1994). Formation of the Arabian Nubian Shield began with the initiation of subduction and development of magmatic arcs at 870 Ma. Terrane amalgamation associated with closure of the Mozambique Ocean and amalgamation of East and

West Gondwana took place between c. 780 Ma and c. 600 Ma (Johnson and

Woldehaimanot, 2003).

To the west of the Red Sea, the oldest arc terranes (> 800 Ma) of the Arabian Nubian

shield occur in the south, in Ethiopia, Eritrea and Sudan (Johnson and

Woldehaimanot, 2003).  In contrast, ophiolitic rocks of the Eastern Desert of Egypt

range in age from 810 to 720 Ma (Ali et al., 2010), and are overlain by younger (c.600

Ma) volcanic sequences (e.g. Breitkreuz et al. (2010)).

Pre-Cambrian alluvial sedimentary rocks of the Hammamat Group overlie the

Arabian Nubian Shield basement in the Eastern Desert of Egypt (Figure 4.1). The

Hammamat Group clastics comprise terrestrial molasse in the Red Sea Hills area and

corresponding Midyan Terrane in northwest Saudi Arabia. The timing of deposition

of these sediments and their facies is of some debate. Some authors (e.g. Eliwa et al.

(2010) and Johnson et al. (2011b)) argue that they were deposited during regional

surface uplift and exhumation (i.e. pre-collisional facies) as part of a major fluvial

system of continental proportions and not in isolated basins as previously believed

(Wilde and Youssef, 2002). However, other authors suggest that the deposition is in

fact syn-collisional  due to the cleaved and stretched nature of some of the facies

(Ries et al., 1983). Bezenjani et al. (2014) also suggest a maximum depositional age of

596 Ma and that deposition occurred during the collision of the Arabian Nubian

Shield with the Saharan Metacraton (i.e. syn-collisional facies).

### 4.2.3 The Pan-African Orogeny

During the Pan-African Orogeny, the final closure of the Mozambique Ocean led to

amalgamation of the Saharan Metacraton and Congo-Tanzanian cratons with the

Arabian Nubian Shield and the formation of the 'Trans-Gondwanan Supermountain' in the region that now forms NE Africa (Meinhold et al., 2013; Squire et al., 2006). To the south, collision between the Saharan Metacraton and Congo-Tanzania craton resulted in the formation of the Oubanguides orogenic belt or Central African Fold Belt (Abdelsalam et al., 2002).

### 4.2.4 Phanerozoic Sediments

Erosion of the Trans-Gondwanan mountain belt resulted in the deposition of a thick cover of fluvial and marine sediments overlying the amalgamated terrains, from the Cambrian onwards. Fluvial sediments were transported north (present day co-ordinates) to the Gondwana margin where they were inter-bedded with marine sediments deposited during periods of marine transgressions. Sedimentation continued until Cenozoic times, punctuated by periods of uplift caused by various plate collisions and disintegrations (Klitzsch and Squyres, 1990).

Previous studies of the cover sediments in regions adjacent to the Nile catchment (i.e. Libya - Altumi et al. (2013), Jordan and Israel (Kolodner et al. (2006a) and Morag et al. (2011)) have put forward contrasting Phanerozoic palaeogeographies for the region during deposition of the sedimentary cover succession. Meinhold et al. (2011) ascribe the textural and mineralogical maturity of the bulk of the cover, and the provenance of the sediments, to varying degrees of recycling, long distance transport, and/or intense chemical weathering. Particularly debated is the origin of the c.1000 Ma zircon population for which an obvious basement source in the Saharan Metacraton or Arabian Nubian Shield has not been recognised (Kolodner et al., 2006a; Meinhold et al., 2011).

### 4.2.5 Cenozoic Uplift and Flood Basalts

More recently, uplift of the Red Sea Hills associated with opening of the Red Sea rift, and uplift in Ethiopia associated with eruption of voluminous continental flood basalts, have had a major influence on Nile drainage. Many studies have attempted to ascertain the timing of Red Sea Hills uplift, with authors suggesting that uplift of rift shoulders began around 24 Ma (Bosworth et al., 2005), 25-30 Ma (Ghebread, 1998), <29 Ma (Kenea, 2001) and 34 Ma (Omar and Steckler, 1995).

The continental flood basalts that dominate much of the Ethiopian Highlands are associated with East African rift-related magmatism and continental break up (Buck, 2006; Ebinger, 2005). Pre-rift basaltic magmatism initiated around 31 Ma (Baker et al., 1996; Rochette et al., 1998; Ukstins et al., 2002) and subsequent uplift, related to magmatic upwelling, caused faulting within what is now the Ethiopian Highlands. Uplift was succeeded by formation of the Afar depression and shield-volcano building episodes between 26 and 22 Ma (e.g. Choke and Guguftu shield volcanoes) (Gani et al., 2007). During these periods, a significant volume of rhyolitic lava and ignimbrite was also emplaced. These latest Oligocene-Miocene felsic rocks are a fertile source of zircons to the modern Nile (Chapter 5).

## 4.3 Previous work on the provenance signal of Nile River sediments

The provenance of sediments in the Nile River have previously been studied using heavy mineral distributions and petrography, Sr and Nd trace isotope studies, and U-Pb analysis of detrital zircons.

Sr and Nd ratios have proved useful when recording major changes in provenance along the course of the River Nile (Padoan et al., 2011). High $^{87}Sr/^{86}Sr$ ratios and low

εNd values in White Nile muds from Archaean cratonic sources, contrast with lower $^{87}Sr/^{86}Sr$ and higher εNd in the River Sobat, which receives most of its sediment load from the crystalline basement and Cenozoic volcanic rocks of the Ethiopian Highlands. Isotope signatures of the Blue Nile and Atbara Rivers are dominated by Ethiopian volcanic detritus and show low $^{87}Sr/^{86}Sr$ ratios and higher εNd values (Padoan et al. 2011).

Heavy mineral analysis and petrography have also been used to characterise the signature of the Nile catchment area (Garzanti et al., 2006). The Blue Nile, Atbara and Tekeze drain predominantly flood basalts and rhyolitic ignimbrites in their upper courses until they reach the Neoproterozoic amphibolite-facies basement of the Arabian Nubian Shield, consisting of granitoid gneisses, staurolite-bearing schists, and marbles (Tadesse et al., 2003), and Phanerozoic sediments found in the pre-rift sedimentary succession of the Blue Nile Canyon (Figure 4.2). Despite both rivers draining similar lithologies in the Ethiopian Highlands, the Atbara contains significantly less quartz than the Blue Nile.

The Victoria Nile downstream of its Lake Victoria output carries feldspatho-quartzose sand with feldspars, derived from granitoid rocks exposed locally (Garzanti et al., 2006). Downstream of the Lake Albert outlet, Albert Nile sand is quartzose with few feldspars and poor heavy-mineral suites with epidote, hornblende, kyanite, rutile and zircon. Sediment composition changes across South Sudan, and White Nile sand of all grain sizes downstream of the Sudd marshes chiefly consist of monocrystalline quartz*,* becoming slightly enriched in plagioclase, volcanic lithics and clinopyroxene

recycled from the Gezira Fan. This fan deposit is ultimately derived from the Ethiopian Traps via an overspill from the Blue Nile (Garzanti et al., 2006).

The Red Sea Hills lie adjacent to the Nile River through much of its course through Sudan and Egypt, and have been considered to be a likely source of sediment to the river. However, Red Sea Hills-derived sediment has not been considered as an end-member in modelling of the Sr and Nd isotope composition of sediments in the Nile delta cone (Krom et al., 2002; Revel et al., 2014). This study aims to address this in looking at the varying contributions from each source area, including the dominantly Phanerozoic cover overlying the Red Sea Hills, over the last c.30 Ma.

Iizuka et al., (2013) present coupled U-Pb, Lu-Hf and O-isotope data for detrital zircons from a sample of modern Nile sand taken, somewhat cryptically, 'Near Cairo City'. They identified age peaks at 1.1-0.9, 0.85-0.7 and 0.7-0.55 Ga, with minor groups at c. 2.6 and 2.0 Ga. They noted that grains with ages between 0.85 and 0.7 Ga had positive εHf values, and were likely to have been derived from juvenile crust in the Arabian-Nubian Shield. Zircons with ages of 1.1 - 0.9 and 0.7 - 0.55 Ga, coinciding with times of supercontinent assembly, showed wide variations in O-isotope composition and εHf.

Be'eri-Shlevin et al. (2014) discuss U-Pb and Hf-isotope data for detrital zircons in Quaternary to recent Israeli coastal sands, which are believed to have been derived by a combination of longshore drift and aeolian transport from the Nile delta. They conclude that the ubiquitous presence of 0.56-0.75 Ga detrital zircons with negative εHf implies that the Arabian-Nubian shield is not the main source of Nile sands. Rather, they believe that multiple recycling through Phanerozoic sedimentary rocks

that blanketed North Africa explains the age and hafnium isotope composition of the detrital zircon populations, as well as the quartz budget of the system.

## 4.4 Analytical Methods

1kg of medium sands and approximately 50g of water-lain mud samples were taken from modern rivers, sedimentary bedrock, modern wadis, and aeolian dunes. Sand and mud samples were taken in order to carry out both single grain and bulk rock provenance techniques. Sample locations were chosen in order to best capture the hinterland of each source area. Modern river samples were preferable to bedrock and wadi sediments as they represent a wider area of the catchment. Whilst upstream samples best reflect variations in local geology, the most downstream samples from each river were taken to represent the best average of the represented catchment. For analyses such as heavy minerals and petrography, samples analysed were restricted to only the Red Sea Hills and Western Desert in order to complement existing datasets (e.g. Garzanti et al., 2006). A sample of gneissic basement was also collected from the Saharan Metacraton. Due to sampling conditions, it was not possible to sample bar and levee or floodplain deposits at each location in order to assess the effect of hydraulic sorting on provenance signatures.

Detailed analytical methods for techniques used in this study are given in Chapter 3 - *Analytical Methods*.

Zircon and rutile grains were separated using standard methods, then hand-picked and mounted in epoxy disks and polished to reveal their interiors. All zircon grains were imaged using Cathodoluminescence prior to analysis in order to allow targeting of laser spots. U-Pb analyses for both zircon and rutile were carried out at the NERC Isotope Geosciences Laboratory (NIGL), using a single collector Nu-Attom mass spectrometer with one of three New Wave laser systems, typically using a 35μm

laser spot. Hafnium isotope composition of zircons was measured at NIGL using a Thermo-Electron Neptune Plus mass spectrometer, coupled to a New Wave 193UC or 193FX Excimer laser. A 50μm spot was used, targeting previously dated zircon domains.

Plagioclase and white mica were separated from the light fraction remaining after zircon and rutile separation. $^{40}Ar/^{39}Ar$ analyses were carried out at SUERC, East Kilbride, using a GVi instruments ARGUS 5-collector mass spectrometer using a variable sensitivity Faraday collector array in static collection (non-peak hopping) mode (Mark et al., 2009; Sparks et al., 2008).

Mud samples for Sr, Nd and Hf analysis were leached in dilute acetic acid to remove carbonate before spiking with $^{149}Sm$-$^{150}Nd$, $^{176}Lu$-$^{180}Hf$, $^{87}Rb$ and $^{84}Sr$ isotope tracers. Standard dissolution methods and ion-exchange chromatography were used to separate elements of interest. Sr and Nd isotope compositions were measured at NIGL on a Thermo-Electron Triton mass spectrometer using dynamic multi-collection. Hf isotope composition was analysed in static mode on a Thermo-Electron Neptune mass spectrometer coupled to a Cetac Aridus II desolvating nebuliser.

Petrographic analysis and heavy mineral analysis of sands and muds were carried out using methods modified from Garzanti et al., 2006 and Garzanti and Andò, 2007. Split aliquots of each bulk sample were impregnated with Araldite and prepared as standard thin sections and stained with alizarine red to distinguish calcite from dolomite. In each thin section, 400 points were counted for petrography according to the Gazzi-Dickinson method (Ingersoll et al., 1984). For heavy mineral analysis, between 200 and 270 transparent heavy minerals were counted in grain mounts by

the "area method" (Galehouse, 1971).  Assemblages were described in terms of

transparent Heavy Mineral Concentrations (tHMC), Zircon-Tourmalline-Rutile Index

(ZTR), Mineral Maturity Index (MMI) and Hornblende Colour Index (HCI). See Chapter

3 (Analytical Methods) for more details.

## 4.5 Results

### 4.5.1 Petrography & Heavy Mineral Analysis

(i) Red Sea Hills, Egypt

Modern Wadi Sands (RSH03a and RSH05a) in northern Egypt are sub-litharenites

(Table 4.1, Table 4.2 and Figure 4.2), with carbonate clasts and minor chert and shale

grains, and a poor to moderately poor tHMC of 1.2 ± 1.0. Epidote-amphibole-

clinopyroxene transparent-heavy-mineral assemblages include minor garnet, zircon,

rutile, staurolite and tourmaline (ZTR 10 ± 5). Cretaceous bedrock samples (RSH08a

and RSH09a) from the Red Sea Hills are quartz arenites (Figure 4.2) with an extremely

high zircon-tourmaline-rutile index (ZTR) of 98-99 and heavy-mineral assemblages of

tHMC 12 and 20. The wadi sands contain slightly more (4-5%) feldspar than the

bedrock samples. This may reflect sampling bias as the modern wadi sands sample a

larger area. A sample from the Hammamat Group (RSH14a) was found to be a lithic-

arkose volcaniclastic arenite, with a zircon-tourmaline-rutile index of 0 and a rich

heavy mineral assemblage (tHMC of 73) dominated by epidote.

 (ii) Western Desert, Egypt

Aeolian dune sands (WD03c, 19c and 20c) in the Egyptian desert west of the Nile are

quartzose, with few feldspars (K-feldspar prevailing over plagioclase) and

sedimentary rock fragments (limestone and subordinately siltstone/shale and chert).

Very poor to moderately poor (tHMC of 0.8 ± 0.4) transparent-heavy-mineral

assemblages include epidote, zircon, amphibole, rutile, tourmaline, clinopyroxene,

staurolite, garnet, kyanite and titanite (HCI of 11 ± 1, MMI of 50, ZTR 34 ± 13).

(iii) Nile Trunk, Sudan

Downstream of the confluence of both the Blue Nile and Atbara with the White Nile (SD04a and SD05a), sediments are quartz-dominated with plagioclase feldspar prevailing over K-feldspar and with some volcanic detritus. Both samples were found to be rich in transparent-heavy-mineral-assemblages (tHMC of 16.8 and 10.1) including clinopyroxene, epidote and hornblende (HCI of 6-7). The ZTR for both Nile trunk samples was very low (0-1).

**Table 4.1** Nile Cone samples analysed for heavy minerals. A more extensive table of results can be found in Appendix 3. *Heavy mineral concentration. **Transparent heavy mineral concentration.

|  | Sample | Type | GSZ | HMC* | tHMC** |
|---|---|---|---|---|---|
| **Pleistocene** | ND41 | Sand | 239 | 0.6 | 0.4 |
|  | ND42 | Sand | 123 | 4.8 | 3.4 |
|  | NDM33 | Mud | 12 | 1.7 | 0.8 |
| **Pliocene** | ND01 | Sand | 365 | 0.8 | 0.3 |
|  | ND03 | Sand | 258 | 0.5 | 0.2 |
|  | ND04 | Sand | 260 | 1.2 | 0.7 |
|  | ND07 | Sand | 153 | 0.6 | 0.2 |
|  | ND09 | Sand | 416 | 1.4 | 0.9 |
|  | NDM02 | Mud | 8 | 1.3 | 0.3 |
|  | NDM07 | Mud | 8 | 6.1 | 1.2 |
|  | NDM12 | Mud | 8 | 38.9 | 0.5 |
| **Miocene** | ND11 | Sand | 10 | 0.3 | 0.1 |
|  | ND13 | Sand | 441 | 0.6 | 0.1 |
|  | ND16 | Sand | 281 | 0.3 | 0.1 |
|  | ND18 | Sand | 167 | 0.2 | 0.0 |
|  | ND22 | Sand | 236 | 0.5 | 0.2 |
|  | ND26 | Sand | 374 | 0.4 | 0.1 |
|  | ND30 | Sand | 215 | 0.2 | 0.1 |
|  | NDM29 | Mud | 63 | 0.6 | 0.0 |
|  | NDM30 | Mud | 60 | 1.1 | 0.1 |
| **Oligocene** | ND32 | Sand | 472 | 0.1 | 0.1 |
|  | ND40 | Sand | 217 | 0.3 | 0.1 |
|  | NDM31 | Mud | 81 | 0.3 | 0.0 |
|  | NDM32 | Mud | 81 | 1.3 | 0.1 |

**Table 4.2** Nile Cone samples used for petrographic analysis. A more extensive table of results can be found in Appendix 4. GSZ = Grain size.

| Sample | Depth (ft) | GSZ (μm) | Q | F | L |
|---|---|---|---|---|---|
| **Pleistocene** | | | | | |
| ND41 | 1213 | 340 | 88 | 11 | 1 |
| ND42 | 1527 | 100 | 73 | 19 | 8 |
| **Pliocene** | | | | | |
| ND 1 | 1705 | 240 | 79 | 13 | 8 |
| ND 3 | 1672 | 450 | 90 | 8 | 1 |
| ND 4 | 1790 | 360 | 89 | 9 | 2 |
| ND 7 | 2434 | 260 | 79 | 17 | 4 |
| ND 9 | 2030 | 500 | 86 | 12 | 2 |
| **Miocene** | | | | | |
| ND11 | 4443 | 300 | 89 | 10 | 2 |
| ND 13 | 4492 | 170 | 88 | 9 | 3 |
| ND 16 | 4678 | 350 | 93 | 6 | 0 |
| ND 18 | 4592 | 230 | 91 | 8 | 1 |
| ND 22 | 4682 | 200 | 86 | 12 | 3 |
| ND 26 | 5236 | 210 | 87 | 11 | 2 |
| ND 30 | 5274 | 220 | 89 | 7 | 3 |
| **Oligocene** | | | | | |
| ND 32 | 5600 | 280 | 96 | 3 | 1 |
| ND 40 | 6517 | 180 | 96 | 2 | 2 |
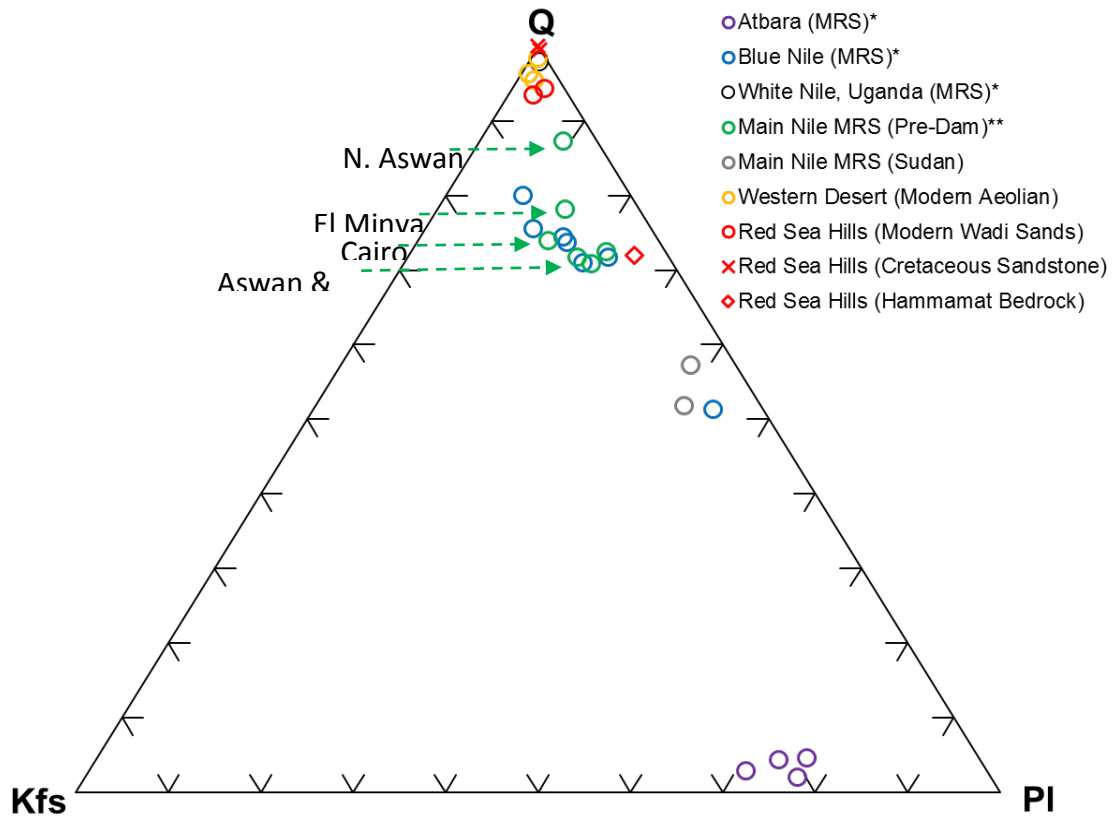
**Figure 4.2** Petrographic variability of detrital modes in modern river sands (MRS), bedrock and aeolian sands from the Nile trunk and hinterland. The ternary plot illustrates the proportion of quartz (Q), K-feldspar (Kfs) and plagioclase feldspar (Pl) of Nile trunk and hinterland modern sands (aeolian and river) and bedrock sands (Cretaceous 'Nubian' and Neoproterozoic Hammamat volcanic arenite). Data from Garzanti et al. (2006)(*) and Garzanti et al. (2015)(**).

### 4.5.2 Major and trace element chemistry

Trace element results are presented in Figure 4.3, normalized to the trace element concentrations of Post Archean Australian Shale (PAAS), compiled by McLennan and Taylor (1985). V, Cr, Co, Ni and Cu concentrations from trace analysis were of particular interest as their quantities enable us to quantify the amount and location of mafic material within the Nile catchment area.

As expected, mafic material is shown to be predominantly derived from the Ethiopian Flood Basalts, carried by the Blue Nile and Atbara. When upstream samples from the Blue Nile and Atbara (Padoan et al., 2011) are compared to samples taken downstream in Sudan (this study), a noticeable decrease in all trace elements can be seen. This is particularly true of Cr, where we see a decrease from an anomaly of 6 to 3.4 in the Atbara and from 2.7 to 1.6 in the Blue Nile.

All modern Nile trunk samples show higher Cr and Ni ppm values than found in the White Nile (Padoan et al., 2011) and Red Sea Hills (modern wadi muds), but still lower than found in both the Blue Nile and Atbara in the Ethiopian Highlands (Padoan et al., 2011).

Samples from the White Nile and Western Desert show similar anomalies. This is expected due to the cratonic nature of the bedrock in their respective source areas (Figure 4.1).
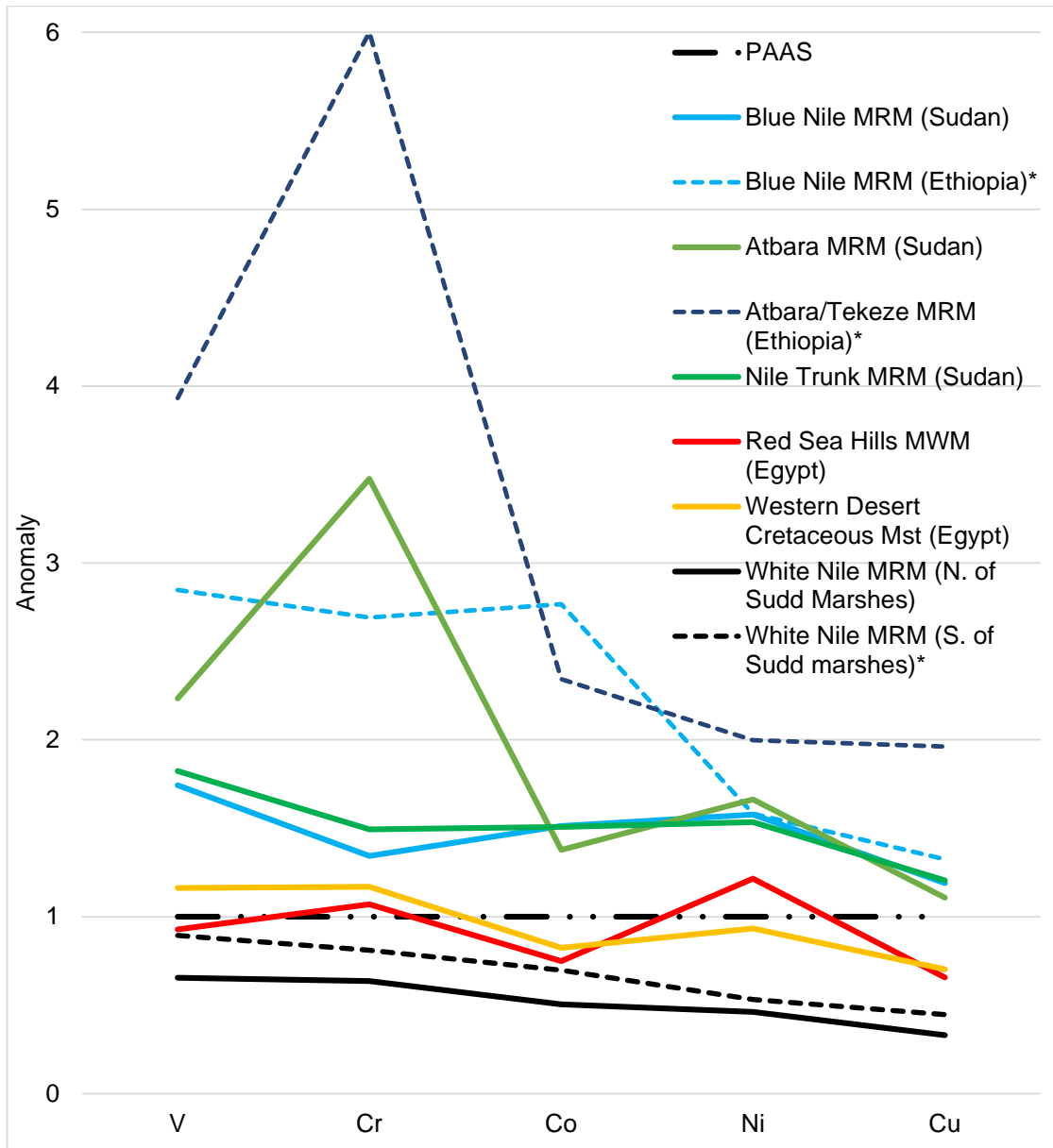
**Figure 4.3** XRF results showing selected trace element concentrations from each of the Nile source areas and the main Nile trunk. Concentrations are normalized to trace element concentrations of Post Archean Australian Shale (PAAS) compiled by McLennan and Taylor (1985) where (in ppm) Cr = 110, Ni = 55, Cu = 50, Co = 23, and V = 150. *Data from Padoan et al. (2011).

### 4.5.3 U-Pb ages and Hf isotope signature of zircon.

Probability density plots and hafnium isotope data shown in Figures 4.4 and 4.5. The location of all analysed samples is shown in Figure 4.1.

**i) Cratonic sources**

**- *Western Desert Archaean Gneiss.***

The oldest bedrock sample analysed (WD16a) is a grey gneiss, mapped as Archaean crust of the Saharan Metacraton (Daumain et al., 1958), collected east of Uweinat in southernmost Egypt.  Zircon crystals have oscillatory-zoned cores under CL, with homogeneous CL-dark, possibly metamorphic overgrowths (Figure 4.4 inset).  Cores are commonly broken, with abrupt terminations, suggesting that the sample may have had a sedimentary protolith that has undergone high-grade metamorphism.

Fifteen U-Pb analyses of zircon cores have $^{207}Pb/^{206}Pb$ ages ranging from 2924 to 3235 Ma, with a single analysis giving a statistically younger age of 2794 Ma.  It is not possible to identify statistically valid populations within the zircon core dataset due to the small number of cores and rims found in the samples. This may reflect a detrital source for the zircons.  The zircon cores have an average εHf of -2.3, and a weighted average depleted mantle model age (TDM$_{Hf}$ ) of 3479 ± 47 Ma (MSWD = 4.1, n= 15/16).

Five analyses of zircon rims form a cluster with a weighted average $^{207}Pb/^{206}Pb$ age of 2701 ± 32 Ma.  Three further rim analyses yield younger $^{207}Pb/^{206}Pb$ ages, between 2524 and 2587 Ma.  The zircon rims yield an average εHf of -10.6 and a weighted average TDM$_{Hf}$ of 3467 ± 45 Ma (MSWD = 2.2, n=8), within error of the age derived from zircon cores, indicating that new zircon growth took place in a closed system

during high-grade metamorphism (Flowerdew et al., 2006). The weighted average model age of all zircon analyses in this sample is 3474 ± 31 Ma (MSWD = 3.3, n=23/24).  It is notable that the Th/U ratio of cores (0.37 – 1.3) is considerably higher than that in the rims (0.03 – 0.14), supporting a metamorphic origin for the rims.

- ***White Nile (Uganda) – N7-16 and N7-17***

Modern river sands were collected from the White Nile upstream of the Sudd marshes at Itanda Falls (N7-16) and Murchison Falls (N7-17) in northern Uganda. Both samples show a similar distribution of Archaean ages, with maxima at c. 2620 Ma (Figure 4.5), and only a few older grains.  Analyses with $^{207}$Pb/$^{206}$Pb ages of 2500 – 2570 commonly occur as overgrowths on older zircon cores.  Only 3% of grains in sample N7-16 give younger, Neoproterozoic to Mesoproterozoic ages.  However, N7-17 contains 24% of such grains, with significant populations at c. 630, 800 and 900-1000 Ma (Figure 4.5).

The c. 2620 Ma zircon population in sample N7-17 typically shows oscillatory zoning under CL, and has an average εHf of -7 and a TDM$_{Hf}$ of 3412 ± 23 (MSWD = 2.3, n=68/74; Figure 4.4).  Eight grains with ages between 900 and 1000 Ma have an average εHf value of -24, a composition that is consistent with formation by melting of Archaean crust similar to that represented by the c. 2620 Ma zircon population. The 900 – 1000 Ma grains show oscillatory zoning with no evidence for core/rim relationships.  Zircons with ages between 670 and 870 Ma have εHf between +3.5 and -15, requiring input of juvenile material in addition to Archaean crust.  These grains are typically CL-light, and weakly zoned or unzoned, with Th/U of 0.22 – 0.89.

Four analyses of rims on Archaean zircon cores give ages of c. 630 Ma, with an average $\varepsilon$Hf of -30.5 (Figure 4.4). The overgrowths show no zoning under CL, and have low Th/U (<= 0.03), suggesting a possible metamorphic origin. A single zircon rim, which formed on a c. 800 Ma grain, also gives an age of c. 630 Ma, with $\varepsilon$Hf = -14, again consistent with growth in a closed system under metamorphic conditions (Flowerdew et al., 2006).

Figure 4.4 includes a field for North-East African Archaean Basement, which is derived using the composition of zircons in the Saharan Metacraton gneiss (WD16a) and the detrital zircon grains from the White Nile at Murchison Falls (N7-17). The slope of the observed trend is consistent with an average $^{176}$Lu/$^{177}$Hf ratio in the sampled North African crust of c. 0.012. This field represents the likely composition of craton-derived grains in other sedimentary rocks of the Nile catchment, discussed below.
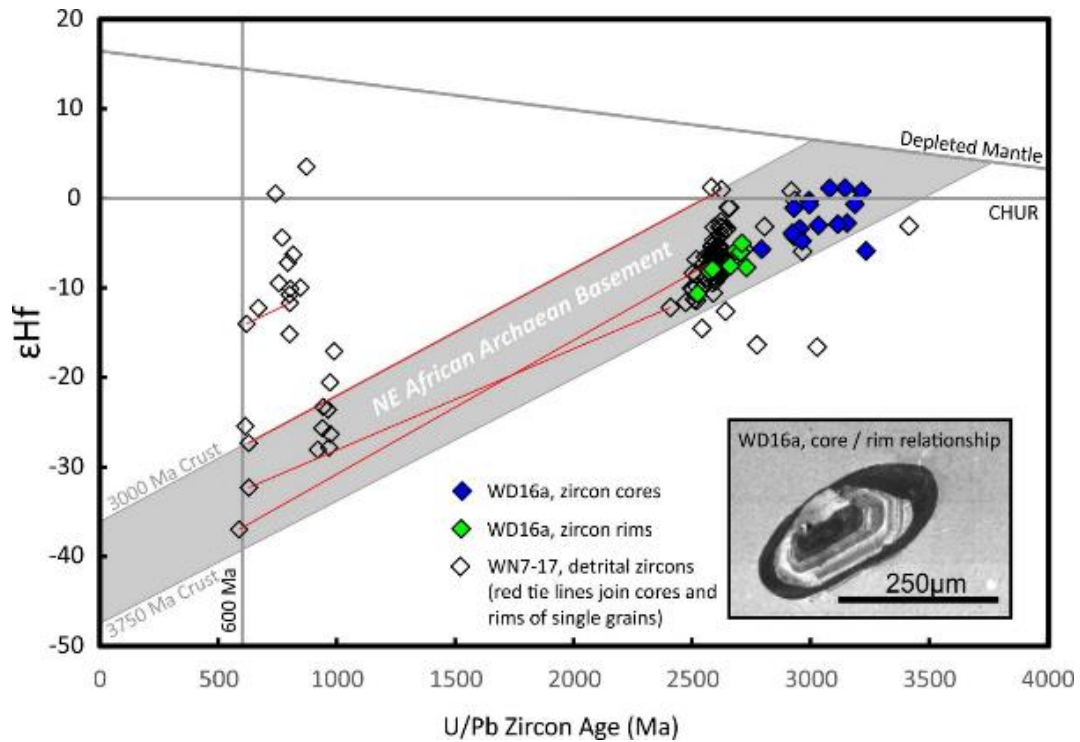
**Figure 4.4** U/Pb age and hafnium isotope composition of complex zircons in Archaean gneiss within the Saharan Metacraton (WD16a), and detrital zircons in White Nile sand draining Archaean craton (N7-17). The grey field represents the Hf-isotope evolution of average NE African basement. 600 Ma is shown as a reference point during the Pan-African Orogeny. Inset shows a CL image of a zircon that exhibits a broken core and metamorphic rim. Two sigma uncertainties are smaller than the symbol size, typically c. 20 Ma on the age determinations, and 1-2 epsilon units.

## ii) Arabian Nubian Shield cover – the Hammamat Group

Sample RSH14a is a volcanic arenite collected within conglomerates of the Um Had conglomerate member of the Hammamat Group, in Wadi Hammamat (Abd El-Rahman et al. 2010). The Hammamat Group in this area is folded, cleaved and overthrust by a complex of c. 740 Ma ophiolitic and volcaniclastic rocks of the Arabian Nubian Shield, prior to intrusion of the Um Had granite at 596.3 ± 1.7 Ma (Andresen et al. 2009).

Sample RSH14a has a rich heavy mineral assemblage dominated by epidote. Zircon grains are dominated by a c. 630 - 780 Ma grains with juvenile hafnium isotope values (Figure 4.4). Only four grains give apparent ages younger than 620 Ma, the youngest having a $^{206}Pb/^{238}U$ age of 596 ± 18 Ma – within error of the age of the structurally much later Um Had granite. Because the timing of deposition of the Hammamat Group is disputed (e.g. Wilde & Yousef 2002, Bezenjani et al. 2014), it was important to establish whether these anomalously young grains had been affected by Pb-loss. Several grains with ages younger than 645 Ma were therefore revisited, and five new analyses were carried out on each grain (data and age calculations are presented in Appendix 11). All grains yielded ages of c. 635 Ma or older, confirming that the original analyses had been affected by Pb-loss (Figure 4.5). The original analyses used a much larger laser spot size (35μm, cf. 20 μm for the new analyses), and may have been more likely to intersect cracks and defects in the grains.

80% of the overall zircon population have positive, juvenile εHf values (Figure 4.5). Grains in the region of 700-800 Ma show higher εHf values (+14) than seen in any

other sample in the Nile catchment area. 2% of analysed grains gave

Palaeoproterozoic or Archaean ages.
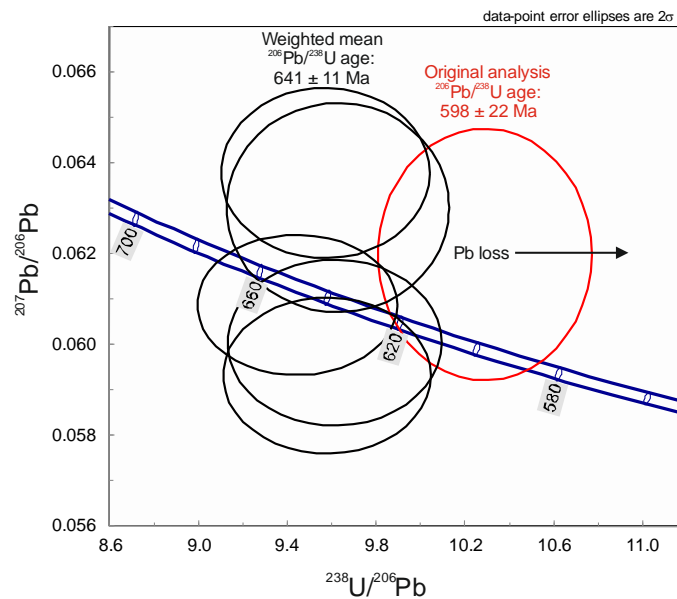


**Figure 4.5.** Tera-Wasserburg plot illustrating the effect of Pb loss on the youngest Hammamat grain population, creating a c.40 Ma age difference between the original analyses and later analyses of 5 spots on the same grain.

### iii) Phanerozoic cover rocks

- ***Western Desert (Egypt)***

Sample WD12a (Figure 4.6) is a Palaeozoic ripple laminated quartz arenite collected in Wadi Tahl, south-western Egypt, while WD18a is a Mesozoic quartz-arenite collected in Wadi Wassa, south-western Egypt.  Both samples have a dominant zircon population at c. 600 Ma, with > 60% of grains of this age showing negative εHf. Zircons between 700 and 900 Ma are dominated by more juvenile grains, with positive εHf.  A population of c.  1000 Ma grains appears to fall into two distinct groups, with juvenile and more crust-dominated hafnium compositions.  In addition, subordinate populations of Paleoproterozoic and Archaean grains (totalling c. 10%), and sparse Phanerozoic grains are present.

- ***Red Sea Hills (Egypt)***

Sample RSH09a is a Cretaceous quartz arenite from Wadi Kharit in the Red Sea Hills. Zircons are dominated by peaks at c. 620, 730-900 and 1000 Ma, with predominantly juvenile εHf.  A minority of grains at c. 620 and 1000 Ma show more cratonic εHf values.  25% of c. 620 Ma grains and 42% of c. 1000 Ma grains show negative εHf.  8% of grains give Archaean or Palaeoproterozoic ages.

## iv) Modern wadi sands

- ***Western Desert (Egypt)***

WD04a is a dune sand, collected in the Western Desert of Egypt.  The zircon age and εHf isotope distribution are similar to the Western Desert bedrock samples, with zircons populations at c. 600 and 1000 Ma (Figure 4.5 and 4.6) dominated by grains with a strong cratonic hafnium signature (c. 60% and 80% respectively).  16% of grains give Archaean or Palaeoproterozoic ages.

- ***Red Sea Hills (Egypt)***

RSH07a is a modern wadi sand collected in Wadi Hammamat, deposited on Cretaceous sandstone bedrock.  The zircon age and εHf isotope distribution are similar to the Red Sea Hills Cretaceous bedrock sample, with peaks at c. 620, 770 and 1000 Ma.  50% of 620 Ma grains and 42% of c. 1000 Ma grains have cratonic εHf values.  8% of grains give Archaean or Palaeoproterozoic ages.

## v)  Modern river sands

### - Blue Nile

Sample ETH2a was collected from the Blue Nile Gorge in the Ethiopian Highlands. It shows two main zircon age populations at 660-720 Ma and 800-850 Ma. εHf values are dominantly juvenile, although sparse grains at 500-600 Ma yield εHf values as low as -10. Sparse c.1000 Ma ages are also present, but Archaean and Palaeoproterozoic ages are absent. Juvenile Cenozoic grains are present. Sample SD03 was collected near Wad Madani in Sudan. It is dominated by 750-850 Ma zircons with juvenile εHf values. Only sparse c.600 Ma grains are found, and only one Palaeoproterozoic age was observed.

- *Tekeze*

Sample ETH6a was collected from the river Gibai, a tributary of the Tekeze, while Sample ETH08a was collected further downstream at Malemin Bridge. Both samples show dominant peaks at c. 620 Ma and a number of peaks ranging back to c.1000 Ma. Sparse Palaeoproterozoic and Archaean grains make up c. 6% of each population. A single Cenozoic grain was identified in each sample.

- *Atbara*

Sample SD06 was collected from the Atbara close to its confluence with the Nile Trunk in Sudan. The most dominant population forms a peak at c.600 Ma, with a subordinate peak at c.800 Ma, both dominated by juvenile εHf values. Palaeoproterozoic and Archaean grains are sparse (3%). Cenozoic grains make up 6% of the population.

White Nile

Sample SD02 was collected from the White Nile downstream (north) of the Sudd marshes in Sudan. Zircons are dominated by c.600 Ma grains, with subpopulations

showing both juvenile and more cratonic εHf values.  Older age peaks at c. 850 and 1000 Ma are dominated by juvenile εHf values.  Only two Archaean grains were identified (c. 2%), in marked contrast to sample N7-17 (see above) from upstream (south) of the Sudd marshes.

- ***Nile trunk***

Sample SD04 captures the signature of the Nile trunk at Dongola in northern Sudan, downstream of the confluences of the Blue Nile, White Nile and Atbara, but upstream of the Aswan Dam.  The detrital zircon age and εHf distribution are similar to the upstream Blue Nile sample (ETH2a), with peaks at c. 630, 680 and 830 Ma, all dominated by juvenile εHf values.  Only two Archaean to Palaeoproterozoic ages are present (2%).  Four Cenozoic ages were measured.

Sample BS01 was collected downstream of SD04 at Beni Suef, south of Cairo. It is dominated by c. 600 Ma zircons, with smaller populations at c.830 and 1000 Ma.  εHf values show dominantly juvenile values, but 11% of c. 600 Ma and 73% of c. 1000 Ma grains have negative, craton-influenced values.  Archaean and Palaeoproterozoic grains make up 9% of the zircon population.  No Cenozoic grains were observed.

### 4.5.4 Ar/Ar Mica and Plagioclase Feldspar and U/Pb Rutile

Samples analysed include N7-17, ETH02a, RSH-7a and SD04a which are a combination of modern river and wadi sands (Figure 4.1). Similar to the zircon U/Pb data, the $^{40}Ar/^{39}Ar$ mica and plagioclase data and the U-Pb rutile data all show a dominant Pan-African signature (c.600 Ma). Despite having a strongly Archaean signature in U/Pb zircon analyses, White Nile samples show evidence of overprinting by the Pan-African orogeny as neither rutile, plagioclase or mica analysis show any

grains to be older than c.623 Ma. Despite other analyses showing the presence of Cenozoic grains in samples from the Ethiopian Highlands, this is not picked up in $^{40}Ar/^{39}Ar$ analysis data.

### 4.5.5 Sr, Nd and Hf isotope analysis of modern river muds

Mud samples were collected from the surface of flash-flood deposits in the Red Sea Hills in order to characterise the composition of material eroded from local Phanerozoic sedimentary rocks.  The muds show a limited range in isotope composition (Figure 4.8 and 4.9), with moderately radiogenic $^{87}Sr/^{86}Sr$ (averaging 0.7096), and non-radiogenic εNd (averaging -6.1) and εHf (averaging -4.9).  Fine grained muds and aeolian samples collected in the Western Desert show considerably more scattered results, with radiogenic $^{87}Sr/^{86}Sr$ (0.708 to 0.716) and non-radiogenic εNd (-5.8 to -12.8) and εHf (-8 to -21.6).

Modern river mud samples collected from the Atbara and Tekeze rivers have Sr, Nd and Hf isotope compositions similar to average Ethiopian basalts (Figures 4.4, 4.6; Pik et al., 1999, Meshesha et al., 2010).  Samples from the Blue Nile, the Nile Trunk in northern Sudan, and the Nile in Egypt (collected before the construction of the Aswan High Dam), plot on trends towards higher $^{87}Sr/^{86}Sr$, and lower εNd and εHf, consistent with incorporation of older sediment derived from sources other than Ethiopian basalt.  A sample collected from the White Nile just south of its confluence with the Blue Nile at Khartoum plots close to the Nile Trunk trend.

Two modern river mud samples have anomalous isotope compositions.  A sample from the Uri River, a tributary of the Tekeze in Ethiopia, together with a White Nile sample collected at Kosti, 300 km south of Khartoum, have significantly more

radiogenic $^{87}Sr/^{86}Sr$ (Tekeze 0.7090, White Nile, Khartoum 0.7093), and less radiogenic εNd (-5.1, -5.9), although εHf is similar to the least radiogenic Nile Trunk samples (-2.6, -3.3). These samples plot within the range of the modern wadi muds draining Phanerozoic sediments in the Red Sea Hills (Figure 4.8 and 4.9).

Two samples collected from the Albert and Victoria branches of the Nile in Uganda were also analysed.  These have highly radiogenic $^{87}Sr/^{86}Sr$ (0.718, 0.721), and non-radiogenic εNd (-26.3, -34.1) and εHf (-25.9, -55.4).

Excluding the two anomalous samples described above, and the White Nile samples taken from Uganda, the range in isotope composition shown by the Nile and its tributaries is rather limited:  $^{87}Sr/^{86}Sr$ varies from 0.7043 in the Atbara to 0.7067 in the White Nile sample from Khartoum; εNd varies from 5.5 to -1.8; and εHf varies from 10.8 to -1.8.
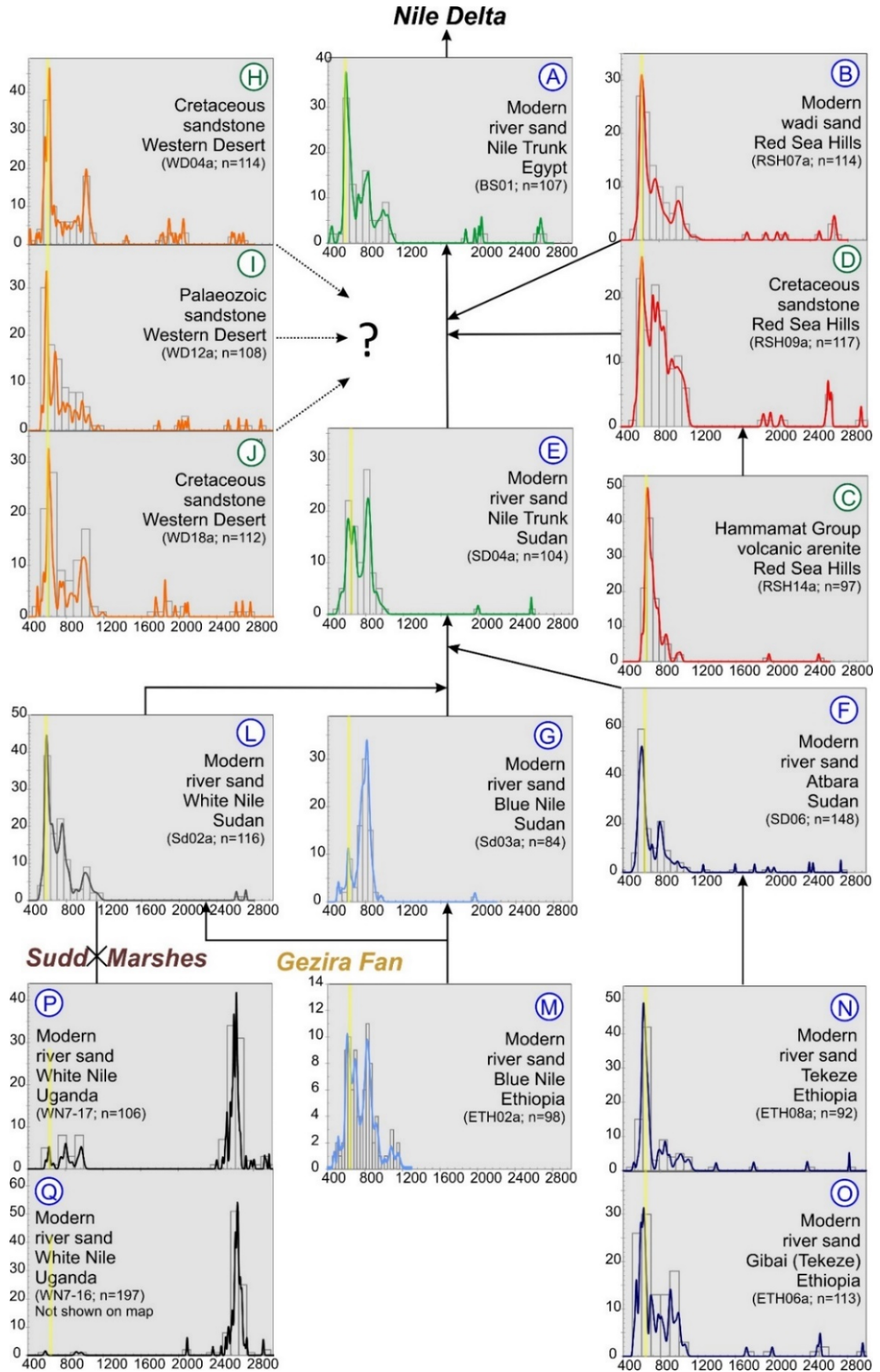
**Figure 4.6** Detrital zircon U-Pb age frequency and relative probability plots for each Nile cone source area.
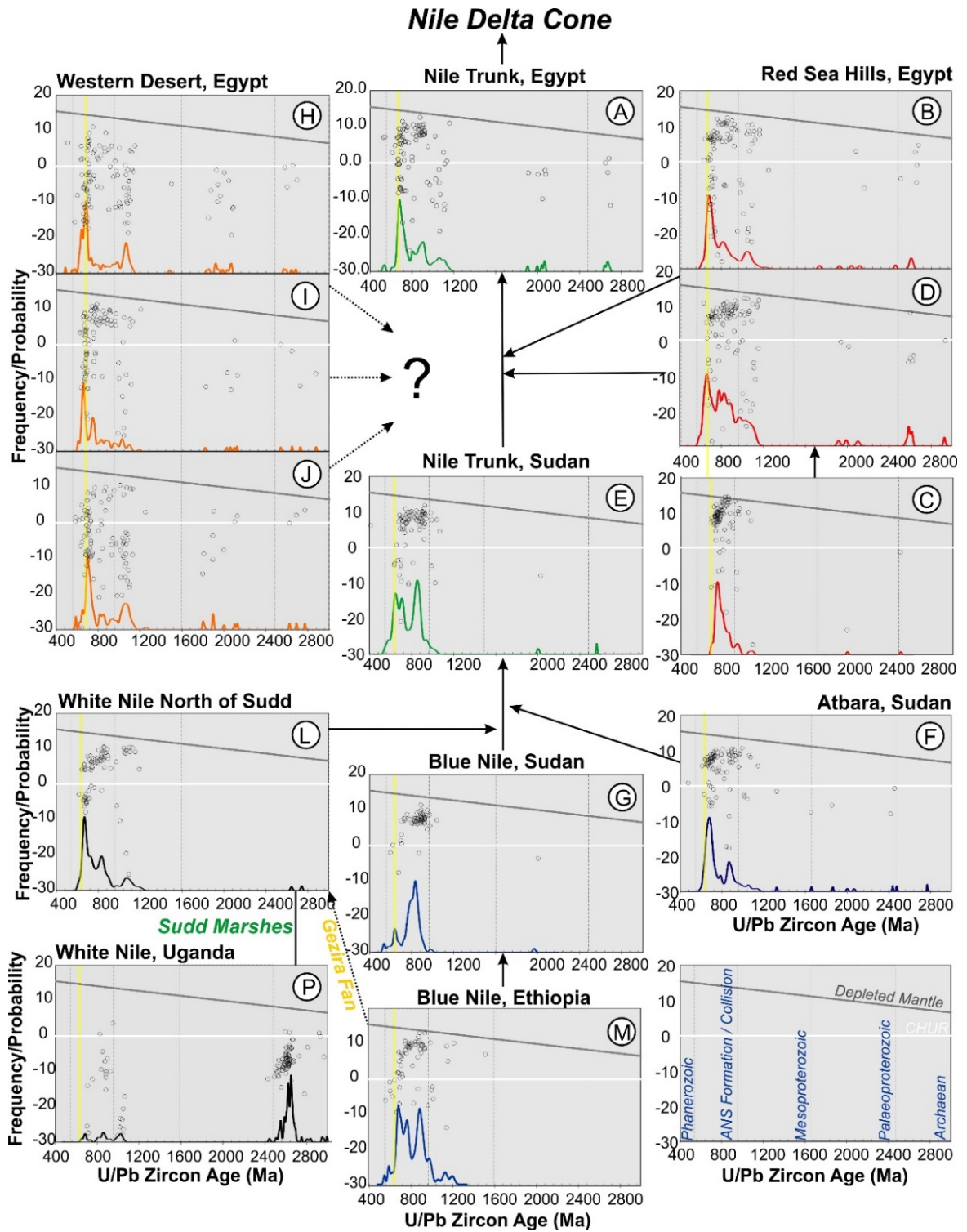
**Figure 4.7** Detrital zircon U-Pb age frequency and relative probability plots with εHf vs U-Pb age. The yellow line at 600 Ma marks the approximate time of the Pan-African orogeny and the collision of the Arabian Nubian Shield with the Saharan Metacraton, Congo and Tanzanian cratons. Letters in each diagram refer to samples in Figure 4.8.
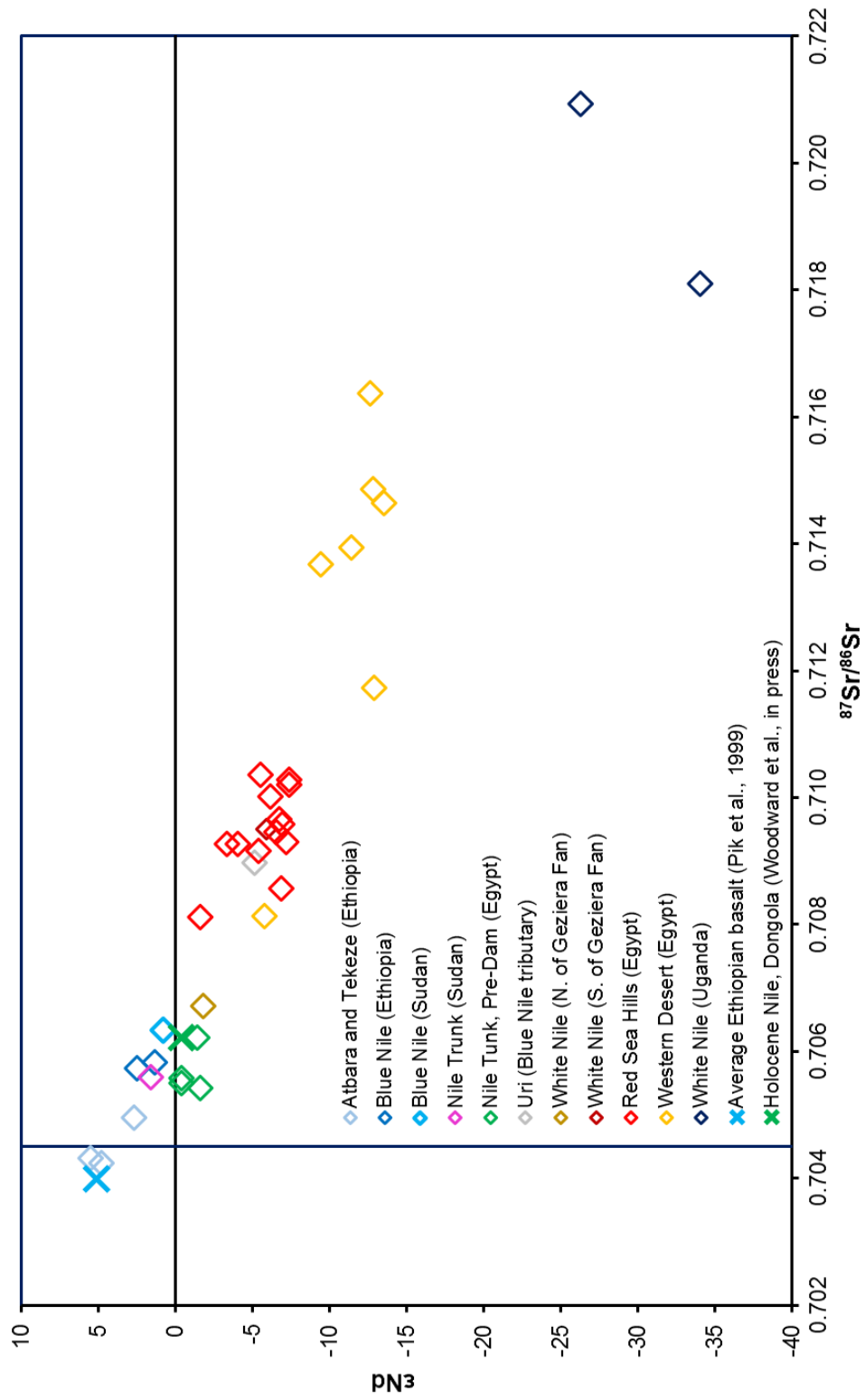
**Figure 4.8** $^{87}Sr/^{86}Sr$ versus $\varepsilon$Nd isotope data for Nile hinterland and trunk muds and Nile trunk sands taken .prior to the construction of the Aswan dam.
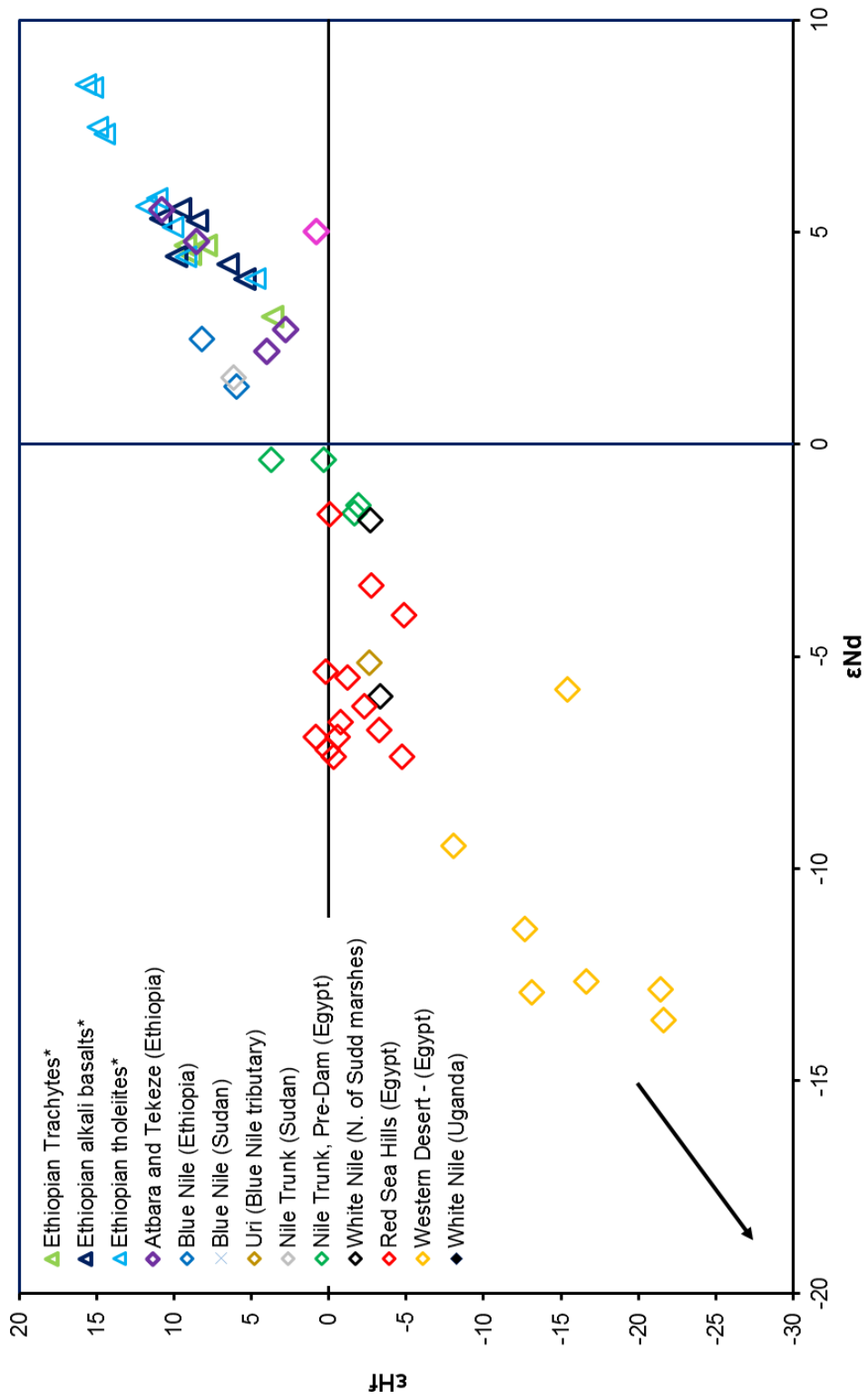
**Figure 4.9** εHf plotted against εNd for the Nile hinterland and main Nile trunk. Black arrow indicates trend towards the location of Ugandan White Nile analyses.

## 4.6 Discussion

### 4.6.1 Precambrian cratons

The Nile traverses Precambrian rocks of the Congo-Tanzania craton and Saharan Metacraton. The geology of the Saharan Metacraton (Figure 4.1) is poorly understood due to the overlying sedimentary cover and desert sands, and as a result very little modern isotope data is available to help constrain its age and tectonic evolution; the U-Pb ages reported by Abdelsalam et al. (2002) are discordant pre-chemical abrasion ID-TIMS ages, or model ages derived by zircon evaporation techniques, which yield poorly constrained $^{207}$Pb/$^{206}$Pb ages only. However, Bea et al. (2011) report Archaean U-Pb SHRIMP ages as old as 3 Ga for gneisses at Uweinat, with evidence for crust as old as 3.22 Ga at Gebel Kamil in southern Egypt. Similar ages have been obtained in this study for gneisses from c. 80 km east of Uweinat, within the region mapped as the metaigneous Gebel Kamil Series by Bea et al. (2011). The sample studied here (WD16a) has evidence for a metasedimentary protolith (broken pre-metamorphic zircon cores), with evidence for zircon growth between c. 3.2 and 2.9 Ga, and subsequent metamorphism at c. 2.7 Ga. Depleted mantle Hf model ages lie between 3.4 and 3.5 Ga. We see no evidence in our data for the c.2 Ga thermal event (the Eburnean orogeny) recorded by Bea et al. (2011).

Sample N7-17, a modern river sand sample collected at Murchison Falls, Uganda, was sampled from within the North-East Congo Block of the Congo-Tanzanian craton, close to the Aswa Shear Zone, which forms the boundary with remobilized crust of the Saharan Metacraton to the north (Appel et al., 2005; Katumwehe et al., 2015), adjacent to the Pan-African Central African Fold belt. Zircons from this sample have similar Hf model ages (Figure 4.4) to the Archaean gneiss sample from the Saharan

Metacraton (WD16a). Zircons in the Murchison Falls sample record crystallisation at c.2.7 Ga, c.960 Ma and c. 600 Ma; the younger age population forms rims with Hf isotope compositions that are consistent with re-melting of similar Archaean crust. The fields defined by the Saharan Metacraton and modern river White Nile (Figure 4.4) provides the best estimate of the composition of Precambrian cratonic basement in the Nile catchment.  600 Ma zircon rims, and similar aged rutile, plagioclase and mica indicate penetration of the effects of the Pan-African orogeny deep into the craton interior, in agreement with the previous work and conclusions of Appel et al. (2005) and Schenk et al. (2007).

### 4.6.2 The Hammamat Group

The depositional and tectonic environment of the Hammamat Formation, which directly overlies or is in structural contact with the Precambrian Arabian Nubian Shield basement, is disputed; both a pre-Pan-African (Eliwa et al., 2010) and post-collisional depositional environment (Bezenjani et al., 2014) have been proposed. Both local and long-distance distal provenance have been suggested (Avigad et al., 2012).

Previous workers have tried to establish the maximum depositional age of the Hammamat Group using detrital zircon populations (Wilde & Yussef 2002, Bezenjani et al 2014).  This can be approached using a number of methods:  the age of the youngest grain, the age of the youngest population of grains, or the age of the youngest population with consistent chemistry (e.g. hafnium isotope composition). In all cases, the determination of maximum depositional ages is complicated by the possibility of Pb-loss leading to spuriously young ages.  Recent recommendations (summarised inSpencer (2016) Spencer et al., 2016) suggest that if anomalously

young grains are found, these grains should be reanalysed several times in order to test for Pb-loss.

The volcanic arenite sample from the Hammamat Group studied here contains four zircon grains that give $^{206}Pb/^{238}U$ ages younger than 620 Ma.  In detail, these grains are slightly discordant, and repeat analysis (5 analyses for each grain) demonstrated that these grains had indeed suffered Pb-loss, and had crystallisation ages of 635-640 Ma.  This is consistent with the age of the youngest concordant zircon population with consistent hafnium isotope composition in the data set, which has an age of c. 640 Ma.

Wilde and Youssef (2002) and Bezenjani et al. (2014) record younger maximum depositional ages, (e.g. 596 ± 5 Ma), but these are based on sparse young grains which may have been subject to lead loss; indeed, the youngest grains in the Thalbah Group (Bezenjani et al. 2014, Figure 5d) are clearly discordant.  The absence of a significant c. 600 Ma zircon population, which dominates all overlying sedimentary rocks and modern river samples elsewhere in North Africa, also argues in favour of deposition of the Hammamat group before the emplacement of the post collisional granites following the Pan-African Orogeny at 600 Ma. Indeed, the field relationships in Wadi Hammamat clearly show that the Um Had member sampled in this study is folded, overthrust by ophiolites and volcanoclastic sediments, and subsequently intruded by a c. 596 Ma granite (Figure 4.10).  The c. 635 Ma maximum depositional age for the Hammamat Group proposed in this study slightly predates the age of c. 630 Ma suggested by Fritz et al. (2013) as the age of collision between the Arabian Nubian Shield and the Saharan Metacraton.
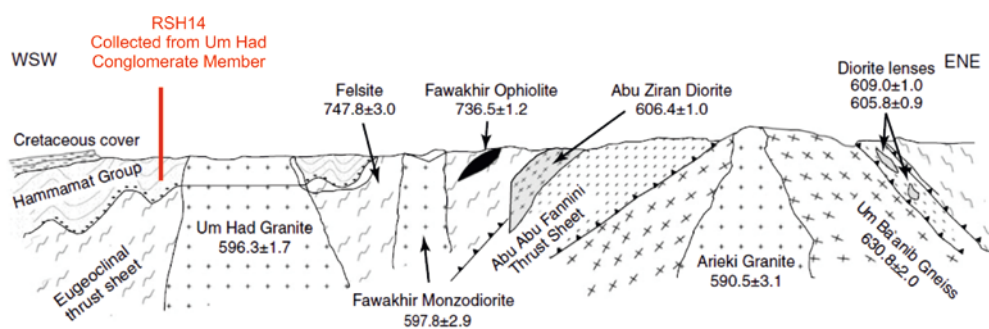
**Figure 4.10** Schematic cross-section (Abd-El-Rahman, 2010) illustrating the stratigraphic relationship between the Hammamat Group, RSH14a (maximum depositional age c.635 Ma, this study) and the Um Had Granite (c.596 Ma from U-Pb ID-TIMS, Abd El-Rahman et al., 2010).

A maximum depositional age of c. 635 Ma for the Hammamat Group is consistent with the proposed depositional age of similar sedimentary rocks in Sinai (the Wadi Zaghra metasediments;(Andresen, 2014)).

The presence of c.1000 Ma grains in Palaeozoic and Mesozoic sediments in North Africa and in this case, the Hammamat Group is of great debate as the nearest known source is 3000km's away (Burundi, Rwanda – Cahen et al., 1984). However, Avigad et al. (2012) and Kolodner et al. (2006b) suggest that these Mesoproterozoic grains show no signs of long distance transport which suggests that they have come from a more proximal source (Avigad et al., 2012; Kolodner et al., 2006b) . Avigad et al. (2003) suggest that Kilbaran material could have been transported from East Africa towards the margins of Gondwana by Neoproterozoic glaciers, and that the glacial detritus was later reworked into the lower Palaeozoic section by the Cambrian–Ordovician fluvial system. Neoproterozoic diamictite successions, considered to be products of the 720–750 Ma Sturtian glaciation, have been reported from the southern part of the Arabian–Nubian Shield in Ethiopia (the

Negash diamictite) and Eritrea (Beyth et al., 2003; Miller et al., 2003b). These diamictites contain Kibaran age zircons (Avigad et al., 2012).

Hammamat Formation zircon data analysed as part of this study (Figure 4.4 and 4.5) can be largely explained entirely by derivation from underlying local Arabian Nubian Shield bedrock, which is dominated by zircons with juvenile hafnium isotope compositions derived from 870-630 Ma oceanic arc rocks. Sample RSH14a contains a highly juvenile zircon population at c.780 Ma with εHf values in the region of +15. The composition of these zircons is consistent with derivation from ophiolitic sources within the Arabian Nubian Shield. Greiling et al. (2014) report fragments of ophiolites and ophiolotic melange in the Hammamat area and Ali et al. (2010) discuss a 2-stage evolution for the Yanbu–Onib–Sol Hamed–Gerf–Allaqi–Heiani (YOSHGAH) ophiolite belt at ∼810–780 Ma and ∼730–750 Ma.

The small number of Pre-Neoproterozoic grains found in the Hammamat sample could possibly be explained by derivation from within the Arabian Nubian Shield (Ali et al., 2009)  without having to invoke a more distal source. The Arabian Nubian Shield bedrock in Egypt incorporates some inherited pre-880 Ma igneous zircons with juvenile εHf values indicating either incorporation of sediments during subduction along a passive margin or inheritance from the mantle source region, or both (Stern et al., 2011) . Wilde and Youssef (2002) suggest other possible source areas for these Pre-Neoproterozoic grains, such as the Central and South Eastern Desert, or further afield in the Arabian Nubian Shield in parts of Saudi Arabia where sparse zircons of this age have previously been recorded. However, we believe that such distal sources

are not required to explain our data because it is possible that they have been derived from more proximal sources within the Arabian Nubian Shield in Egypt.

The volcanic lithic arenite composition and epidote-rich nature of the Hammamat bedrock sample (RSH14a) supports our interpretation that it is derived directly from Arabian Nubian Shield arc rocks in a pre-collisional intra-arc setting. Furthermore, the composition and zircon U-Pb ages of the sample are in stark contrast to the overlying post-collisional Phanerozoic cover sequences in the region, which are quartz arenites with ZTR indices as high as 99 and have diverse zircon U-Pb age spectra, as described below.

Given the above, we therefore consider there is no evidence to suggest that the Hammamat Formation sampled in this study is post-collisional or that long distance transport needs to be invoked.

### 4.6.3 Phanerozoic Cover

Samples from Phanerozoic cover sequences in the Western Desert and Red Sea Hills of Egypt are mineralogically mature and contain zircons with similar age peaks to those of cover rocks from surrounding regions (Figure 4.4). Red Sea Hills Phanerozoic cover and modern wadi samples are derived from out with the underlying Arabian Nubian Shield basement. this is indicated by:

- the occurrence of >2000 Ma zircons, which are extremely rare in the Arabian Nubian Shield (Stern et al., 2010);

- the increased mineralogical maturity and more complex zircon populations compared to the underlying locally sourced Hammamat Formation (see above);

- the presence of a significant 1000 Ma population with cratonic εHf values, which is incompatible with derivation from the juvenile arc of the Arabian Nubian Shield.

A similar conclusion was reached by Morag et al. (2011) who looked at εHf values of the 1000 Ma zircon population in cover sequences of Israel and Jordan. Although their data showed a preponderance of grains with negative εHf values, our data from Egypt shows two populations at c.1000 Ma, one with positive εHf values and one with negative values. Whilst the population with positive values would be compatible with derivation from an as yet unrecorded arc from within the Arabian Nubian Shield, the provenance of the population with negative εHf values remains enigmatic. The cratonic c.1000 Ma zircons found in the Mesozoic cover of both Western Desert and Red Sea Hills samples can be most simply explained by recycling from underlying Palaeozoic cover sequences, but the original basement source is debated. As pointed out by Kolodner et al. (2009), long distance transport from suitable cratonic source areas far to the south are ruled out by the paucity of >2000 Ma grains which would also be present if derived from such a region. It is possible that the source could be material transported from East Africa towards the margins of Gondwana by Neoproterozoic glaciers as suggested by Avigad et al. (2003). Neoproterozoic diamictite successions have been reported from the southern part of the Arabian–Nubian Shield in Ethiopia (the Negash diamictite) and Eritrea (Beyth et al., 2003; Miller et al., 2003a). These diamictites contain c.1000 Ma old zircons (Avigad et al., 2003). Alternatively, the original source may have been from a region since rifted off Gondwana, which may have also supplied zircons to, for example, the

Neoproterozoic Arkenu Formation cover sediments of Libya, which contains grains of an appropriate age (Meinhold et al., 2011).

### 4.6.4 Effects of geomorphology and local bedrock geology on the isotope signal of the Nile River

North of Uganda, the White Nile passes through an extensive area of marsh land (The Sudd) which has trapped most of the detritus from the river since 2.7 Ma (Williams and Talbot, 2009). This is clearly reflected in the isotope data. Zircons in Ugandan White Nile modern river sediments, south of the Sudd, are dominated by Archaean grains with evidence for crustal reworking and new zircon growth at c.960 and 600 Ma. A craton-dominated signature is also displayed by the highly negative $\varepsilon$Nd values and high $^{87}Sr/^{86}Sr$ values of the White Nile muds.

By contrast, north of the Sudd at Kosti, the detrital signature of White Nile zircons is much less cratonic. Archaean grains are almost completely absent, and instead the zircon populations show strong similarities to Blue Nile and/or Phanerozoic cover sediment signatures (Sample SD02). A mud sample from the same location has Sr-Nd-Hf values similar to Phanerozoic cover (Figure 4.8 and Figure 4.9). Potential contributing sources to the White Nile north of the Sudd could be the Sobat River, the Ethiopian Highlands via the Blue Nile (Gezira Fan), and/or alluvial fans draining into the river from the Nuba Mountains.

The River Sobat drains similar lithologies to the Blue Nile. Published data show it to have $^{87}Sr/^{86}Sr$ values of 0.708-0.712 and $\varepsilon$Nd values of -1.6 to -9.1, spanning the range of our data for modern muds in the Red Sea Hills (Padoan et al 2011). However, the River Sobat flows through an extensive region of marsh land north of

the Sudd (the Machar Marshes) and was not considered to be a significant source of sediment to the Nile Trunk by Padoan et al., (2011).

Sample SD02 was collected north of Kosti, close to the southern limit of the Gezira fan, so significant input of Blue Nile material from across the fan is not thought to be likely.  However, from the Last Glacial Maximum (c. 20 Ka) onwards, a major alluvial fan (the Khor Abu Habl alluvial fan) has drained into the river from the Nuba Mountains to the west (Williams et al., 2000).  Ephemeral rivers feeding the fan drain Proterozoic basement rocks and overlying Cretaceous 'Nubian' cover sequences.

Further downstream, a mud sample at SD01b, collected just to the south of Khartoum has an $\varepsilon$Nd of -1.8 and $^{87}$Sr/$^{86}$Sr of 0.7067. This is due to the sample location being adjacent to the Gezira Fan (Williams 2009), which formed during the Late Pleistocene. During times of peak flow, suspended sediment from the Blue Nile was transported across the fan and deposited in the White Nile dramatically altering its signature (Williams, 2009).

Further downstream to the north, the Blue Nile, and then the Atbara, join the Nile trunk. Both the Blue Nile and the Atbara drain, from south to north downstream: Cenozoic volcanic rocks; Phanerozoic cover; Arabian Nubian Shield; and Proterozoic basement with Pan-African mineral cooling ages (Mock et al., 1999). Sr-Nd-Hf isotope data indicate that the Atbara has a higher proportion of volcanic detrital contribution to the river sediment compared to the Blue Nile, which is also reflected in petrographic data showing a higher proportion of clinopyroxene and olivine (Garzanti et al., 2006). Evolution of the signal downstream is indicated by a decrease in Cr content (Figure 4.3) in both the Atbara/Tekeze and Blue Nile. This is also reflected in

the progressively higher $^{87}Sr/^{86}Sr$ values and lower εNd and εHf values (Figure 4.8, Figure 4.9) as the rivers' drainage areas evolve from mafic-dominated (εNd and εHf values >0) to encompass increasing proportions of basement and/or cover sediment downstream. Notably, a sample collected from a tributary of the Tekeze (the Uri) in an area of Palaeozoic cover rocks has an isotope composition identical to that of the local bedrock, indicating that this material is an important source to the river. Variation in the bedrock lithology is also illustrated by the significant change in proportions of major zircon populations in the Blue Nile downstream. Notably, the region of Arabian Nubian Shield cut by the Blue Nile in NW Ethiopia contains granitoids with U-Pb zircon ages in the ranges from 650 – 700 and 800-880 Ma, and juvenile εNd values (data summarised in Johnson (2014)). These populations are clearly represented in our Blue Nile dataset, with prominent peaks at 800-830 Ma in samples ETH2a and SD03, persisting into the Nile trunk at Dongola (sample SD04). 680 Ma zircons are also abundant in sample ETH2a from the Blue Nile, and in the southern Nile trunk (SD04).

The Nile trunk sample taken downstream of the White Nile confluences with the Blue Nile and Atbara, at Dongola in Sudan (SD04a), shows a U/Pb zircon signature much the same as the Atbara and Blue Nile combined. The c.1000 Ma peak, present in the sample from the White Nile North of the Sudd (SD02a) is not seen in the Nile Trunk. The dominant contribution to the Nile trunk from the Blue Nile over the Atbara is shown by the similarity in Sr-Nd values between the Blue Nile and Nile trunk (Figure 4.7), the paucity of Meso- and Palaeoproterozoic zircon grains in the trunk Nile sample, a characteristic similar to that of the Blue Nile but not of the Atbara. The greater contribution of sediment from the Blue Nile versus the Atbara to the Trunk

124

Nile is in agreement with the conclusions of Garzanti et al., (2006) based on petrographic data.

Between Dongola, Sudan, and Northern Egypt, the trunk Nile flows between the Red Sea Hills to the east and the Western Desert in the West, both comprised predominantly of Phanerozoic sedimentary cover. Contribution to this stretch of river from such cover rocks is shown by the difference in zircon age and εHf value distribution between samples at Dongola (SD04a) and Northern Egypt (Beni Suef, BS01), with the latter containing more Palaeoproterozoic-Archaean grains and grains with cratonic εHf, similar to the signature of Phanerozoic cover (Figure. 4.4 and 4.6). Dilution of the mafic-influenced signal by cratonic/cover sediment input is also demonstrated by the decreasing εNd values between Dongola and sands from the Egyptian Nile collected prior to construction of the Aswan High Dam (Shukri, 1950), although the change in $^{87}Sr/^{86}Sr$ ratio is less evident. The Red Sea Hills, rather than the Western Desert, is considered to be the major contributor of the Phanerozoic detritus in view of its elevated topography.

### 4.6.5 Supercontinent Assembly and the Pan-African Orogeny

Figure 4.9 shows all of the U/Pb and Hf isotope data derived from Nile hinterland samples as part of this study. In Figure 4.11, The largest peak at c.600 Ma relates to the Pan-African orogeny when Neoproterozoic juvenile intra-oceanic island arcs of the Arabian Nubian Shield accreted, and finally collided with the Saharan Metacraton and Congo/Tanzania cratons (Johnson et al., 2011a). This can be seen in samples derived from as far afield as the White Nile in Uganda (N7-17 and N7-16).

The influence of the Pan-African Orogeny was also seen in U/Pb rutile, and Ar/Ar plagioclase and mica ages which reflect post orogenic cooling. This is in agreement with hornblende, muscovite, amphibole, biotite and sericite $^{40}Ar/^{39}Ar$ data from Arabian Nubian Shield bedrock (Johnson et al., 2011a).

In detail, the data show two maxima at c.840-780 and 700-600 Ma with juvenile εHf values, which represent two major episodes of arc development within the Arabian Nubian Shield. The reduction in data density between the two episodes may relate to arc collisions in the Arabian Nubian Shield, documented by the emplacement of ophiolites at this time (Ali et al., 2010), which may be represented in our dataset by c. 750 Ma detrital zircons from the Hammamat Group, which have the highest (most juvenile) εHf values in the entire data set.

The final closure of the Mozambique Ocean is documented by the marked switch to more negative εHf values in the c.600 Ma population, due to the intrusion of post-collisional granites derived by melting of continental crust within the suture zone.

Pre-Neoproterozoic grains make up to 97% of sediment in the White Nile south of the Sudd. They are also relatively common in cover sediments and modern wadi sediments sampled in the Red Sea Hills (average 9%) and the Western Desert (average 12%). Such grains are extremely sparse in the White Nile north of the Sudd (average 2%), Blue Nile (average 1%) and the Nile Trunk in Sudan (average 2 %). They are relatively abundant in sediments from the Atbara and Tekeze (average 6%) and the Nile Trunk in Egypt (average 8%). Although we cannot exclude a small contribution from the White Nile, we believe that the most likely source of the Pre-

Neoproterozoic grains in modern Nile sediments are Phanerozoic cover sequences in the source regions of the Atbara and Tekeze and Red Sea Hills.

A notable feature of the data is the discontinuity of the field of c.1000 Ma grains with juvenile εHf versus those with clear cratonic influence. This suggests two distinct sources, one from an oceanic-arc setting and a second involving re-melting of a cratonic source. The most cratonic grains within each age population in our dataset plot within the field for North African crust derived using our basement data (WD16a and WN7-17).

The supercontinent cycles which led to the creation of Gondwana (650-500 Ma) are represented in all of the samples collected as part of this study (Figure 4.11). The isotope signatures of the samples analysed from the Nile river and its hinterland contain Mesoproterozoic and older zircons that may be related to earlier supercontinent cycles. However, the location of Congo and Tanzania cratons in reconstructions of Rodinia (De Waele et al., 2008) is a matter of debate and the lack of exposure and reliable geological data from the Saharan Metacraton means that its location in Rodinia and earlier supercontinent configurations is unknown. Although our data contain some c.2000 Ma zircons, these cannot be related to the formation of the supercontinent 'Nuna' (aka. Colombia) because it did not involve North African cratons (Rogers and Santosh, 2002).
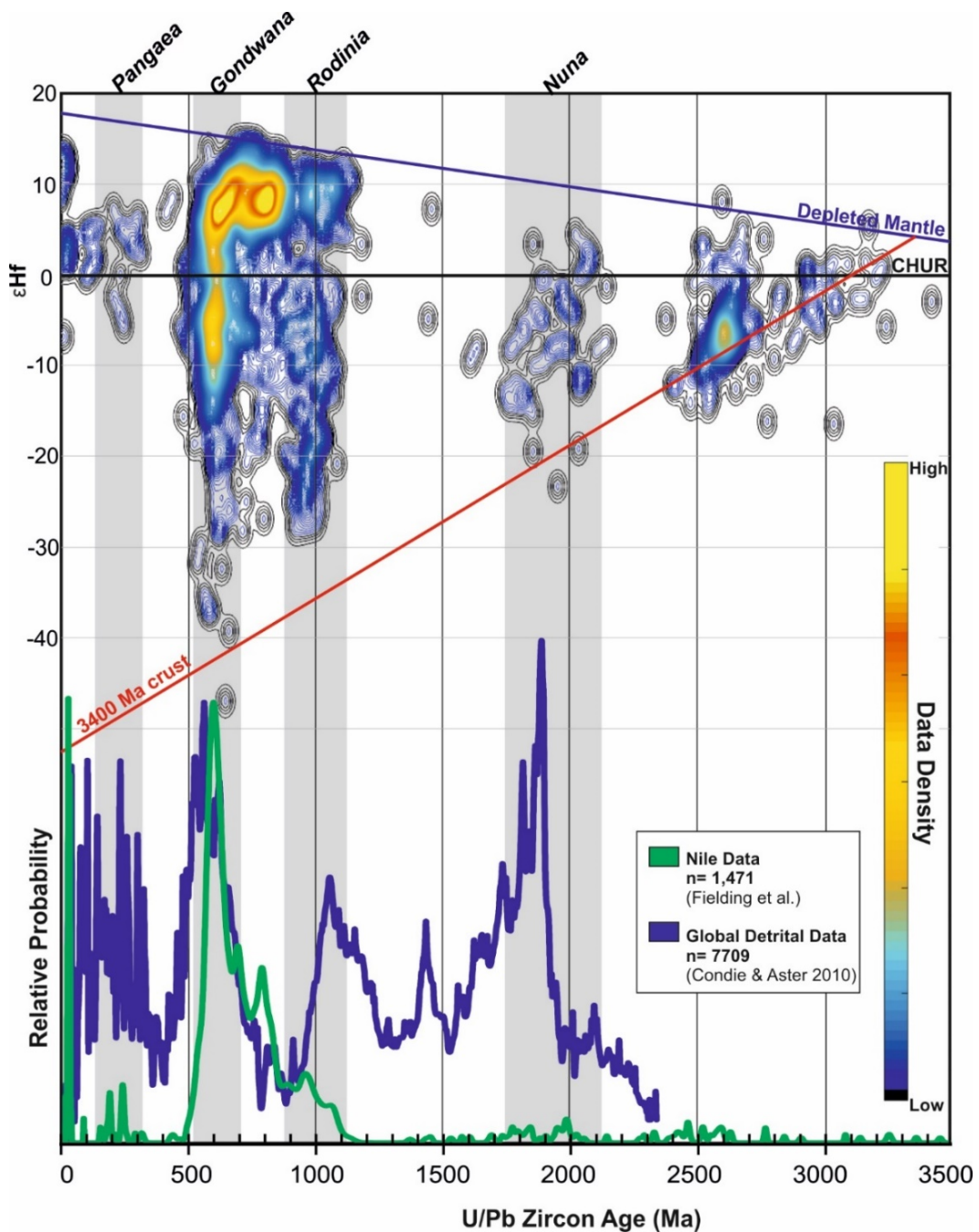
**Figure 4.10** Probability density plot illustrating the Hf isotope – time evolution of the source regions supplying detrital zircons discussed in this study. The density of the data distribution is calculated using a modified version of the MATLAB implementation of the Kernel Density Estimation procedure supplied by Botev (2010), using bandwidths equivalent to the typical analytical uncertainty of the U/Pb ages (±20 Ma) and epsilon hafnium values (± 1 epsilon units). Contours are generated by the MATLAB *contour3* function and plotted using the *plot3d* function. Warm colours (yellow) represent dense areas of data and cool colours (blues) represent more sparse data. Also shown is the global compilation of detrital data from Condie & Aster (2010).

## 4.7 Conclusions

This study expands on previous work characterising the modern Nile hinterland. In doing so, it provides a more detailed understanding of the provenance signatures that may be seen downstream in the Nile cone over time.

Gneissic basement of the Saharan Metacraton in southern Egypt, and detrital zircons derived from rocks of the Congo Craton in northern Uganda, both indicate an age of crust formation between 3.0 and 3.5 Ga, with subsequent melting and/or metamorphism at c. 2.7 Ga.

Our combined U-Pb and Hf-isotope zircon dataset document the evolution of the North African crust, in particular highlighting phases in the development of the Arabian Nubian Shield and its collision with the Saharan Metacraton.  The original source of c.1000 Ma grains in sediments of the Nile catchment remains enigmatic, within which, two distinct populations: one indicating a juvenile ultimate source and one a cratonic source. It is possible that they could have been sourced from West Africa during the Rodinia super continent collision and reworked into Western Desert sediments.

The Hammamat Group of the Arabian Nubian Shield is locally derived and was deposited in an intra-arc setting before the suturing of the Saharan Metacraton and the Arabian Nubian Shield. A maximum depositional age of 630 Ma is based on reanalysis of anomalously young grains, which are shown to have suffered Pb-loss.

As predicted, the provenance signature of the White Nile is dramatically different upstream and downstream of the Sudd marshes as a result of sediment trapping. This study shows that North of the Sudd, at Kosti, the signature of the White Nile is

dominated by material derived from Phanerozoic sandstones via alluvial fans to the west of the river.  Further north however, (south of Khartoum) the White Nile is greatly affected by its proximity to the Gezira fan and receives an influx of Blue Nile sediment during times of peak flow.

Here it is shown that Phanerozoic cover sediments which blanket much of northeast Africa represent an important source of detritus to the river and are characterised by the presence of significant (9-12%) populations of pre-Neoproterozoic zircon grains. Such grains are relatively sparse in modern Nile sediments, but reach a maximum (12%) in the Nile trunk in Egypt.

Blue Nile and Atbara sediments contain Cenozoic zircons sourced from Ethiopian volcanic rocks. The influence of these Ethiopian volcanic rocks decreases downstream in the Blue Nile and Atbara sediments as more and more sediment is derived from nearby Phanerozoic cover and the Arabian Nubian Shield basement.

# Chapter 5: When did the Nile begin?

Laura Fielding[1], Yani Najman[1], Ian Millar[2], Peter Butterworth[3] & Ben Kneller[4]

1. Lancaster Environment Centre, Lancaster University; 2. British Geological Survey, 3. BP Egypt, Cairo; 4. University of Aberdeen, Aberdeen.

## Abstract

The palaeodrainage history of the Nile is greatly debated. Estimates regarding the time the river's catchment expanded from a local area to the extensive catchment that we see today (6,853 km in length) range from Oligocene-Pleistocene. Radar-based river studies, incision rates, uplift histories and sediment volumes have all been used to gain insight into the evolution of one of the longest rivers in the world.

This study investigates the unique sedimentary archive of the Oligocene to Recent Nile submarine cone to document provenance studies for the first time. We show that the extensive Nile catchment that we see today was established much earlier than previously suggested, and present evidence of detritus from the Ethiopian large igneous province (LIP) reaching the delta since at least the Oligocene (31 Ma).

Zircons with U/Pb ages and hafnium isotope signatures compatible with the Ethiopian LIP were supplied to the delta since at least the Miocene (16 Ma). Such zircons are absent from Oligocene delta sediments, but Nd and Sr isotope data for Oligocene delta muds as old as 31 Ma require significant mafic input. The Ethiopian LIP represents the only possible source for this detritus. Our findings have implications for the nature of continental break-up during the Pan-African orogeny, and for sapropel development in the Mediterranean.

## 5.1 Introduction

The present day Nile and its tributaries reach as far south as Lake Victoria and Lake Albert (drained by the White Nile), Lake Tana to the east (drained by the Blue Nile, Atbara and Tekeze in the east) and the Bahr el Ghazal flowing through central Africa and the Congo in the west (Figure 5.1).

Present-day annual discharge from the Nile River is largely due to overflow from equatorial lakes such as Lake Victoria and Lake Albert, feeding the White Nile downstream through the marshes of the Sudd in northern Uganda, before reaching its depocentre in the Nile Delta Cone. The Blue Nile provides a more seasonal supply of discharge during times of heavy rainfall (June-August). However the Blue Nile supplies 96% of the sediment that reaches the Nile delta today (Garzanti et al., 2006)
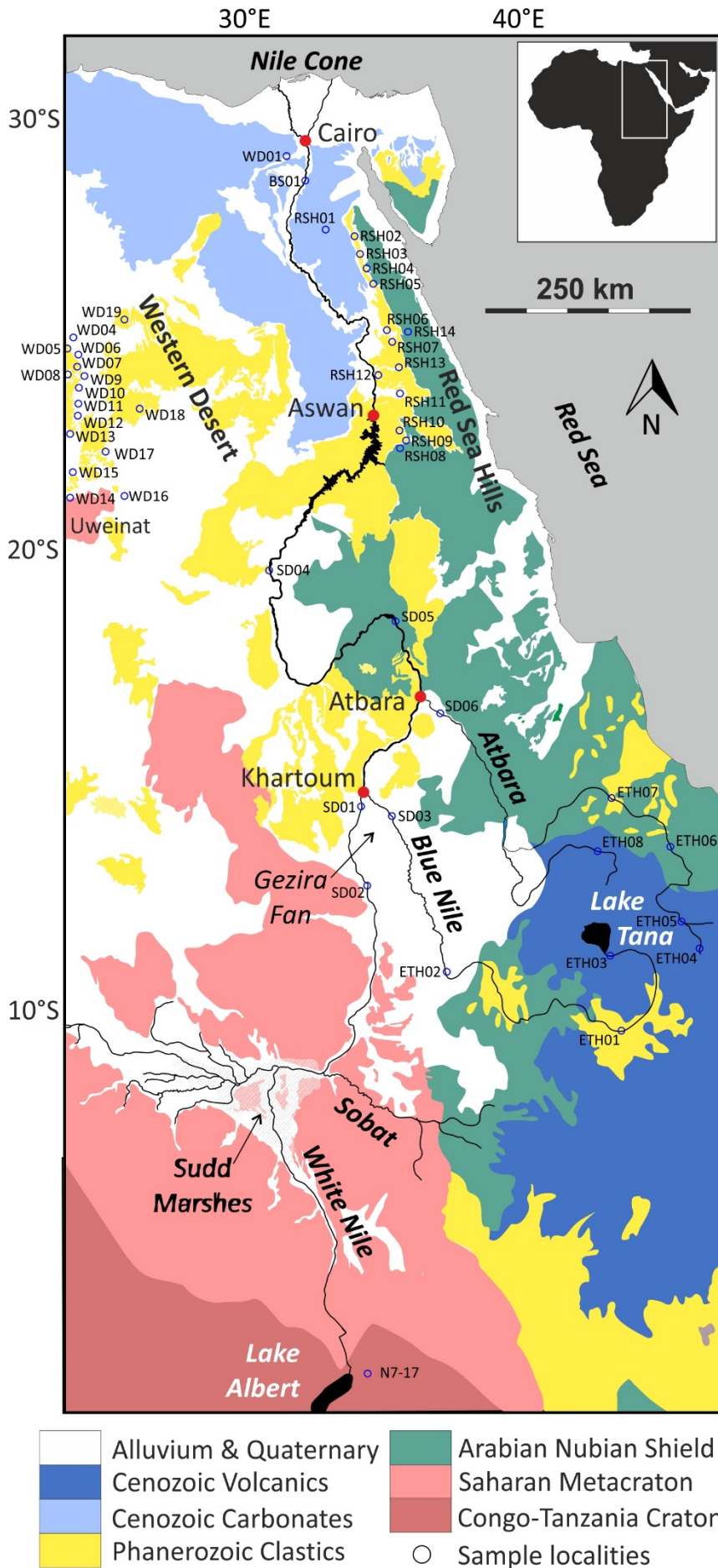
**Figure 5.1 Modern river samples and hinterland geology of Nile river source areas.** Inset shows location of map as boxed area. Map modified from (al-Miṣrīyah, 1981; Johnson, 2014; Kazmin, 1972; Ministry of Energy and Mines, 1981).

### 5.1.1 Previous Palaeodrainage Models

The Nile delta cone is dated as Eocene (onshore) (Underwood et al., 2013) and Oligocene-Recent (offshore); earliest Nile delta cone deposits of Eocene age occur on land at Fayum, just south of Cairo (Underwood et al., 2013). By the Oligocene, the delta cone had prograded to its current position following the shoreline as the Tethys Ocean retreated, exposing a newly emergent hinterland. The Oligocene clastic sediments from the Nile River overlie a segment of a Jurassic and Early Cretaceous passive margin. Miocene Nile cone deposition was interrupted by Late Tortonian and Messinian hinterland erosion and deposition, with Pliocene deltaic deposition re-commencing as a result of a major transgression. The source of the sediments that make up the delta cone are of much debate. The delta is reported to have received detritus from the White Nile only since 5000 years before present (Williams et al., 2003). However, the time that the drainage changed from a locally sourced Red Sea Hills catchment to a more extensive (Blue Nile) catchment encompassing the Ethiopian Highlands is poorly known, with estimates ranging from Oligocene to Late Pleistocene (Issawi and McCauley, 1992; Macgregor, 2012; Pik et al., 1999; Shukri, 1950).

Proponents of Oligocene initiation of sediment supply from the Ethiopian plateau have used knick point facies to infer a 3-phase incision in the Ethiopian Highlands at 29-10 Ma, 10-6 Ma and 6 Ma (Gani et al., 2007); uplift of the plateau instigated erosion in the Tekeze, Atbara and Blue Nile catchments (Gani et al., 2007). Thermochronological studies suggest that the elevated plateau physiography, which controls most of the present-day Nile hydrology, has existed since the Oligocene, ca.29 Ma (Pik et al., 2003).

Authors favouring a Nile drainage originating in the Late Miocene cite sparse remotely sensed radar data to argue for a south-draining 'Qena System' dominating the Nile valley until the Messinian Salinity Crisis (Rouchy and Caruso, 2006). The Messinian Salinity Crisis consisted of a cycle of nearly complete desiccation in the Mediterranean from 5.99-5.33 Ma (Krijgsman et al., 1999), during which time the Nile drainage changed flow direction to the north as a result of down-cutting and river capture of a Wadi Qena river (Issawi and McCauley, 1992). There is no mention by these authors of any connection of the Ethiopian Highlands to the main Nile even in the Late Miocene.

Sediment volume calculations of the delta cone have been used to infer that a connection with the Ethiopian Highlands did not occur until the Pleistocene (Macgregor, 2012; Palacios, 2013). Despite high erosion rates in the Ethiopian Highlands synchronous with uplift since ~31 Ma (Gani et al., 2007; Pik et al., 2008), the low pyroxene content in Pliocene Nile delta sediments (Shukri, 1950) is used to infer that the sink for Ethiopian detritus was elsewhere, or that the Blue Nile was not initiated until the Pleistocene.

We use Oligocene-Recent Nile delta core samples to reveal the first occurrence of material characteristic of the Blue Nile headwaters, namely the Ethiopian continental flood basalts (CFB), and thus to constrain the timing of expansion of the catchment to something approaching its present length of 6,853 km.

## 5.1.2 Potential Nile Source Areas

There are three postulated source areas for the delta cone sediments; the Ethiopian Highlands, White Nile source regions and the Red Sea Hills catchment areas. The Red

Sea Hills of eastern Egypt comprises Neoproterozoic gabbro, granitoid and meta-volcanic basement arc rocks of the northern Arabian Nubian Shield, Mesozoic sedimentary deposits and Eocene carbonates (Daumain et al., 1958). The White Nile Source Regions (Uganda, Rwanda, Sudan, Democratic Republic of Congo and Tanzania) consist largely of the Archaean – Proterozoic Congo and Tanzania cratons with overlying Neoproterozoic and Mesozoic sedimentary rocks (Abdelsalam, 2002). The Ethiopian Highlands (drained by the Blue Nile, Atbara and Tekeze Rivers) comprise Neoproterozoic basement of the southern Arabian Nubian Shield, Mesozoic cover sequences and Cenozoic (~30 Ma) flood basalts (Hofmann et al., 1997; Mohr and Zanettin, 1988). In this study, we focus on detritus derived from the Ethiopian Highlands as its uplift and geological history plays an important role in the present configuration of the River Nile, and its distinctive lithologies and location ensure that occurrence of Ethiopian Highlands detritus in the Nile delta unambiguously indicates initiation of Blue Nile contribution to the delta. The continental flood basalts that dominate much of the Highlands are associated with East African plume activity, rifting and continental break up (Buck, 2006; Ebinger, 2005). Pre-rift basaltic magmatism initiated at around 31 Ma (Baker et al., 1996; Rochette et al., 1998; Ukstins et al., 2002) and subsequent plume-related uplift caused faulting within what is now the Ethiopian Highlands; plume-related uplift was succeeded by formation of the Afar depression and shield-volcano building episodes between 26 and 22 Ma (e.g. forming the Choke and Guguftu shield volcanoes) (Gani et al., 2007). During these periods, a significant volume of rhyolite lava and ignimbrite were also emplaced. It is these Oligocene-Miocene felsic rocks that yield characteristic zircons that enable this provenance study to pinpoint a more precise timing of the Blue Nile

connection to the main Nile trunk by documenting their first occurrence in the Nile delta cone.

This study characterises modern river Nile samples (Table 3.1 and Figure 5.1) and compares them to Nile Cone core samples in order to document provenance changes through time. Both sand and mud samples were taken from the Nile hinterland from flowing rivers where possible. This was done in order to represent a wider area of the catchment as opposed to the analysis of single bedrock samples that would represent the signature of only small geographic regions. Nile Cone samples were collected from pre-drilled core in Cairo, BP Egypt (Table 3.5). Samples from the Cone were restricted to where core had been drilled and varied from consolidated to unconsolidated. All core had previously been logged and dated using biostratigraphy by BP Egypt.

## 5.2 Results

### 5.2.1 Nile source area sediments

Modern river sands and muds were sampled from the Blue Nile, Atbara, Tekeze, White Nile and main Nile trunk in Sudan (see Figure 5.1), in order to characterise the source regions that may have supplied detritus to the Nile cone.  Where modern river sediments were not available (e.g. in the Red Sea Hills), flash-flood deposits were taken.

#### Detrital zircon U/Pb data

All modern river/wadi samples are dominated by c. 600 Ma (Pan-African) and older zircon grains (Figure 5.2), but several samples sourced from the Blue Nile catchment (Figure 5.2f) contain a small proportion of Cenozoic zircons. These Cenozoic grains fall into a bimodal age distribution that corresponds to the two main volcanic episodes in the Ethiopian Highlands, at c. 30-32 Ma and 23-27 Ma. By contrast, samples from the modern Red Sea Hills and White Nile (Figure 5.2g and h) contain no Cenozoic grains.

#### U/Pb and Hf zircon data

When U/Pb zircon chronology is paired with εHf data, it is possible to determine the origin of each grain in terms of its cratonic or juvenile (ocean island arc) source (Figure 5.3). Negative εHf values indicate a cratonic source (i.e. the Saharan Metacraton or Congo and Tanzanian craton) whilst positive values are indicative of ocean island arc sources (i.e. the Arabian Nubian Shield). Juvenile zircons with ages of c. 31 Ma occur in Ethiopian volcanic rocks near Lake Tana (Fig.3). MC-ICPMS

analyses of Hf were carried out on three Lake Tana samples (Zege, Yipag and Hydro); these show a range of εHf values from +15 to +5.

Cenozoic zircons from the Blue Nile, Atbara and Tekeze modern river sediments show two main populations: c. 30 Ma grains have εHf values dominated by less juvenile values (εHf from +5 to 0) than the Lake Tana samples (εHf from 5 to 15), but showing some grains with a similar composition to that of grains derived from Lake Tana rhyolites; 23-27 Ma grains show εHf values between 3 and 14.

### Sr-Nd bulk rock mud data

Each source area shows a distinct Sr-Nd isotope signature. Samples from the Ethiopian Highlands show a distinctive mafic-influenced signature, close to the composition of Ethiopian CFBs, with εNd values ranging from 2 to 8 and relatively low $^{87}Sr/^{86}Sr$. Samples from the Red Sea Hills have a more negative εNd signature with values ranging from -5 to -8 and higher $^{87}Sr/^{86}Sr$ levels, indicating influence from a more cratonic source (Figure 5.4).

Sediments from the White Nile have strongly negative εNd values ranging from -14 to -34, due to their derivation from cratonic rocks of the Congo – Tanzania Craton and Saharan Metacraton. The $^{87}Sr/^{86}Sr$ values vary greatly from sample to sample but are never lower than 0.718.

### 5.2.2 Nile cone sediments

Both mud and medium sand core samples were taken from the Oligocene (Rupelian, 31 Ma) through to Recent, including box core samples from the delta cone, representing Holocene sedimentation prior to construction of the Aswan Dam.

### U/Pb Detrital zircon analyses

All samples contain zircons populations with ages of 500-800, c. 2000 and c. 2500 Ma. In addition, Cenozoic zircons are found in Nile delta samples from Miocene times onwards, with ages that overlap with known episodes of volcanism in the Ethiopian Highlands. Analyses showed the Miocene delta samples to have the greatest age variation (Figure 5.2 and 5.3).

### U/Pb and Zircon Hf data

The grains from older (c.31 Ma) Nile cone sediments show a similar range in age and εHf to zircons from Lake Tana and the Blue Nile (Figure 5.3). Those from younger (c.26 Ma) sediments plot closer to depleted mantle values (εHf = c. 17), also similar to those seen in the Blue Nile.

### Sr-Nd bulk mud analyses

Sr-Nd analyses of core muds from the Nile cone show intermediate values between Ethiopian CFB and Red Sea Hills sediments / Saharan aerosols (Figure 5.4). The simplest explanation for the distribution shown by the data requires a mafic contribution from the Ethiopian Highlands; the Nile delta muds could not have been derived from the Red Sea Hills and aeolian sources alone. Models involving simple mixing of average CFB with average Red Sea Hills sources and their weathered equivalents (Jung et al., 2004) indicate that the Sr and Nd composition of Oligocene and Pliocene muds could be explained by incorporating 10-20% of CFB, whereas Miocene and Pleistocene muds require 30-45% of mafic input. Our Blue Nile, Atbara and Tekeze sediment samples plot on the same mixing trends, close to the CFB end-member.

Derivation of this signature from other Cenozoic mafic sources in Egypt and Sudan

(Lucassen et al., 2008) can be ruled out as they are volumetrically insignificant.
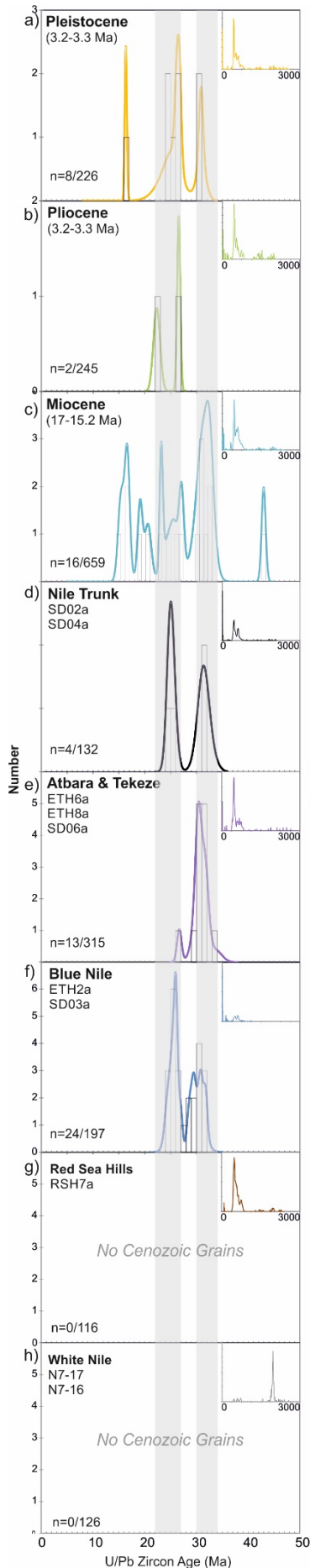
**Figure 5.2 Detrital U/Pb zircon ages from the Nile delta cone and potential source areas.** Histograms and frequency distribution curves for detrital zircon populations from a) Pleistocene Nile delta cone sands; b) Pliocene Nile delta cone sands; c) Miocene Nile delta cone sands; d) Nile trunk modern river sands (Sudan); e) Atbara and Tekeze modern river sands; f) Blue Nile modern river sands; g) Red Sea Hills modern river sands h) White Nile modern river sands. Shaded grey areas represent episodes of volcanism recorded in the Ethiopian Highlands (22-27 Ma and 30-34 Ma). Red Sea Hills and White Nile samples have been plotted to show the absence of Cenozoic grains. 'n= x/xx' refers to the number of Cenozoic grains relative to the total number of grains analysed for each source area.

143
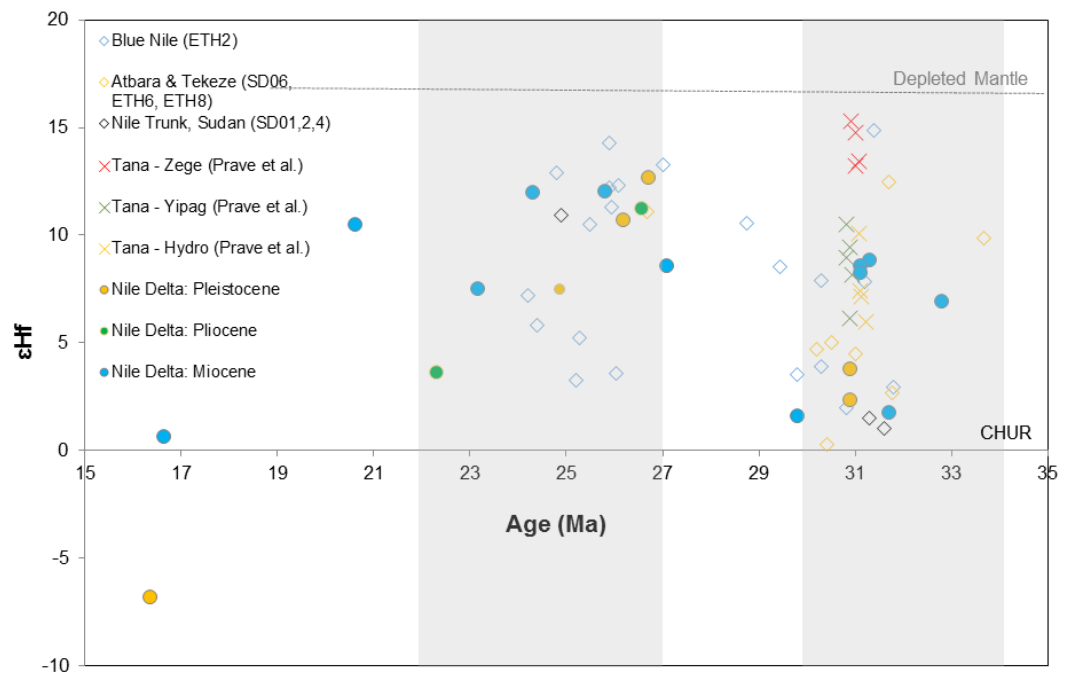
**Figure 5.3 Detrital εHf and U/Pb zircon ages for Cenozoic grains.** Data obtained from the

Atbara, Tekeze, Blue Nile and Sudan Nile trunk modern river sands and Nile delta cone sands

(Miocene-Pleistocene) coupled with wash solutions from ID-TIMS analysis of bedrock

samples taken from rhyolites near Lake Tana.
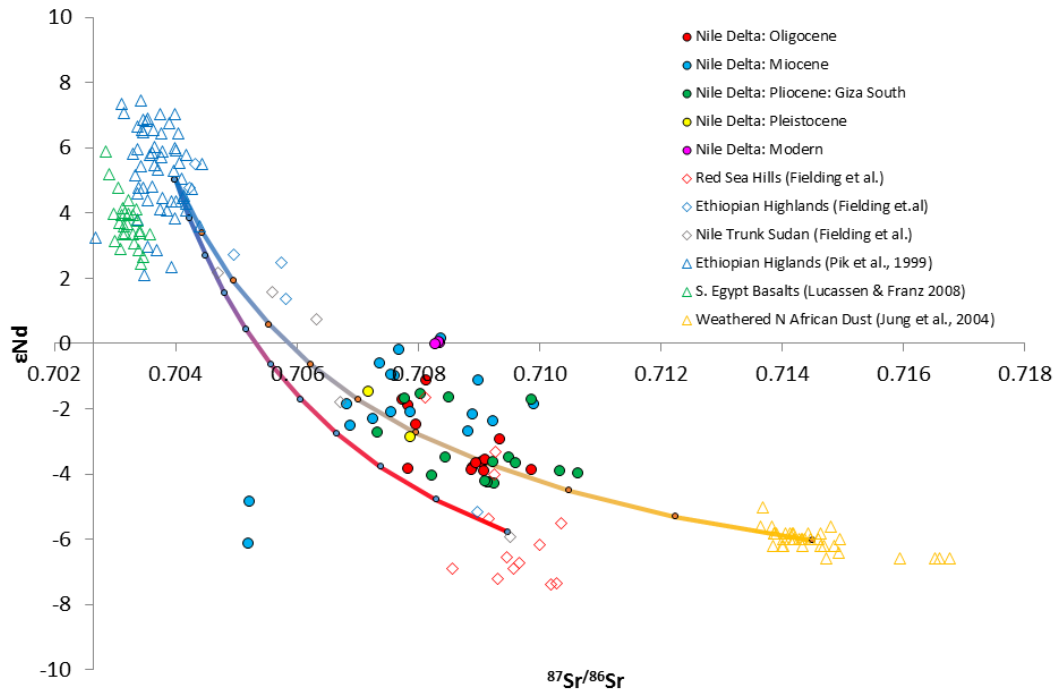
**Figure 5.4 Bulk rock mud εNd and $^{87}$Sr/$^{86}$Sr isotope geochemistry,** with data from modern

river muds and Nile delta cone muds. Nile cone sediments scatter around a mixing line

between basalts from the Ethiopian Highlands (Pik et al. 1999) and more evolved

compositions. Mixing curves are shown between average Ethiopian Highland basalt, and

average Red Sea Hills wadi mud, and the < 2 micron dust fraction interpreted by (Jung et al.,

2004) to represent average weathered north African crust.

## 5.3 Discussion

Results provide strong evidence that rivers draining the Ethiopian Highlands were connected to the Nile delta since at least the early Oligocene, the age of our oldest sediments analysed. U-Pb zircon analyses provide direct evidence supporting Ethiopian CFB input since the Miocene, as Cenozoic zircons occur in Burdigalian-Pleistocene core samples.

Notably, Cenozoic zircons are absent from the Oligocene samples, despite completion of more than 360 zircon analyses. This may be because there was insufficient time for young grains derived from 31 Ma volcanic rocks to be eroded and transported to the delta by the time of deposition of 31 – 27 Ma Oligocene sediments in the Nile cone. Alternatively, Ethiopian rivers were not yet eroding zircon-fertile areas of the catchment.  The Blue Nile cut back by headward incision and it may be that  appropriate sources for the young zircons were not tapped until after 27 Ma, perhaps during the Miocene, when periods of increased uplift and incision occurred (Gani et al., 2007; Pik et al., 1999). However, we have no samples between 27 Ma and 17 Ma in age, so it is not possible to constrain the first arrival of Cenozoic grains from the Ethiopian LIP any more closely.

Despite a lack of Cenozoic zircons in the Oligocene core, the Oligocene Sr-Nd data are more influenced by mafic sources than could be explained by derivation from the Red Sea Hills alone, indicating that the Ethiopian Highlands were contributing detritus to the delta by Oligocene times. This interpretation is supported by the similarity of the Sr-Nd values observed in the Oligocene and Pliocene samples, implying that the provenance of the Nile delta was not significantly different in

Oligocene and Pliocene times; in the Pliocene the presence of Cenozoic zircons unambiguously shows that the Blue Nile/Atbara contributed to the delta.

These data provide the first evidence to demonstrate a source to sink link from Ethiopian Highlands to Nile delta since at least the Oligocene, validating the hypotheses of those who proposed an early (Gani et al., 2007; Pik et al., 2003; Underwood et al., 2013) rather than late (Issawi and McCauley, 1992; Macgregor, 2012; Shukri, 1949) initiation of this major drainage network.

Initiation and changes of drainage patterns, with their attendant sedimentary records, have long been used as an indirect approach to dating surface uplift (e.g. Cox, 1989), particularly in Africa where the inter-relationships between plume influence, continental break-up, epeirogenesis and topographic development are debated (e.g. Paul et al., 2014). Key to understanding the interrelationships are knowledge of the timing of these events. Pik et al.(2003) proposed Blue Nile gorge incision, indicating an uplifted Ethiopian Highlands, since 25-29 Ma, determined from thermochronometry. Paul et al. (2014) used longitudinal river profiles to determine African uplift on the assumption that uplift rate controls profile geometries. They determined development of Afar topography since 40-35 Ma, although they noted the poor fit between calculated and observed river profiles for Nile tributaries draining the Ethiopian Highlands, which they suggested could be attributed to violation of their assumption of invariant upstream drainage area, by river capture. Our research is the first to use a provenance approach to contribute to constraining the timing of this surface uplift. In showing that the Nile routed from the Ethiopian plateau source to delta sink since at least 30 Ma, we infer that the plateau had

uplifted by this time, in agreement with studies using alternative approaches (e.g. Moucha and Forte, 2011). An older Ethiopian-sourced Nile might yet be recognised in onshore Eocene deposits  (Underwood et al., 2013) . Thus it is clear that plateau uplift occurred early in the continental break-up of the region, preceding the initial stages of Afro-Arabian continental rifting by >5 Ma (Ukstins et al., 2002).

Knowledge of the timing of initiation of the Nile also allows assessment of sapropel formation hypotheses. After closure of the Mediterranean's gateway to the Indian ocean (Karami et al., 2009) sapropels formed in the basin from mid-Miocene times (Kidd et al., 1978; Mourik et al., 2010).Their formation in the Mediterranean is said to relate to  increasing amounts of freshwater reaching the basin by a combination of various factors (increased precipitation versus evaporation, glacial run-off and discharge from the Nile and other bordering rivers), leading to increased nutrient supply and anoxia promoted by stratification of the water column, and the importance of Nile runoff to this process is debated (Krom et al., 2002; Meijer and Tuenter, 2007; Scrivner et al., 2004). It was not previously possible to reconcile models advocating a strong Nile influence on sapropel development with the proposal of a late onset of initiation of major Nile drainage. Now, with evidence demonstrating that the Nile has drained into the Mediterranean least since the Oligocene, it is possible to suggest that a major Nile influx of freshwater may have been one of the major contributors to sapropel development in the Mid Miocene.

## 5.4 Analytical Methods

Modern river sediments were collected from each of the source areas. Both sand and mud fractions were sampled, and in some cases bedrock samples were taken if there were no flowing rivers present, for example in the Red Sea Hills and the Western Desert in Egypt. Sand samples were used for *in situ* laser ablation techniques (LA-ICPMS) and mud samples were used for analysis of Sr-Rb and Sm-Nd radiogenic tracers. The Nile delta core sediments were sampled in order to achieve continuous stratigraphic coverage, but with some lateral variation (east, west and central Nile delta). Biostratigraphical ages range from Oligocene to Recent (31, 27.5, 17, 51.4, 15.2, 2.95, 1.8 and 0.02 Ma).

### 5.4.1 U/Pb Zircon LA-ICPMS

Grains were randomly handpicked from mineral separates after sieving at 250μm and using the 'super panner' at NIGL, Keywoth to concentrate zircon grains. These were then mounted in epoxy resin and photographed. Care was taken to ensure there was no bias from the beginning of the sample preparation to the plotting of the data in PDP's (Probability Density Plots). All zircons were imaged using cathodoluminescence prior to laser ablation work to avoid domain cross over between two different zones, radiation damage and cracks. 120 grains were initially analysed from each sample.

After the initial round of analysis, which targeted samples from each source and each time period from the delta cone, additional grain mounts were made and cathodoluminescence microscopy was used to screen for 16-35 Ma grains. The Cenozoic grains have low U contents and low radiogenic Pb contents, and commonly

show normal discordance on a Tera Wasserburg plot due to the presence of common Pb. Multiple spots per grain were therefore analysed in order to derive more precise ages for the Cenozoic zircons. For concordant and near-concordant data, the weighted average of the $^{206}$Pb/$^{238}$U ages was used to derive a pooled age. Where multiple spots fell on a discordia with a realistic upper intercept age, the lower intercept age on a Terra Wasserburg plot was used. Where data showed insufficient range in composition to allow construction of a meaningful discordia, the line was anchored to a common Pb value defined by the combined dataset (Appendix 6).

## 5.4.2 Zircon Hf isotope analysis

Isotope analyses were carried out at the NERC Isotope Geosciences Laboratory using a Thermo Scientific Neptune Plus MC-ICP-MS coupled to a New Wave Research UP193FX Excimer laser ablation system and low-volume ablation cell. Helium was used as the carrier gas through the ablation cell with Ar make-up gas being connected via a T-piece and sourced from a Cetac Aridus II desolvating nebuliser. Lutetium ($^{175}$Lu), ytterbium ($^{172}$Yb, $^{173}$Yb), and hafnium ($^{176}$Hf, $^{178}$Hf, $^{179}$Hf and $^{180}$Hf) isotopes were measured simultaneously during static 30 s ablation analyses. The spot size used was 35 or 50 µm; fluence = 7-10 J/cm$^2$.

Hf reference solution JMC475 was analysed during the analytical session and sample $^{176}$Hf/$^{177}$Hf ratios are reported relative to a value of 0.282160 for this standard. Correction for $^{176}$Yb on the $^{176}$Hf peak was made using reverse-mass-bias correction of the $^{176}$Yb/$^{173}$Yb ratio empirically derived using Hf mass bias corrected Yb-doped JMC475 solutions (Nowell and Parrish, 2001). $^{176}$Lu interference on the $^{176}$Hf peak was corrected by using the measured $^{175}$Lu and assuming $^{176}$Lu/$^{175}$Lu = 0.02653.

At least two zircon reference materials (91500, Mud Tank and on occasion, Plesovice and Zr144 standard glass) were analysed throughout the analytical session. The results of multiple standard analyses are summarised in Appendix 9. The 91500 zircon reference material was used to normalise the $^{176}$Lu/$^{177}$Hf ratio assuming a value of 0.000311 Woodhead and Hergt (2005).

Analytical uncertainties for unknowns were propagated by quadratic addition to include the standard error of the mean of the analysis and the reproducibility of the 91500 reference material. εHf values were calculated using a $^{176}$Lu decay constant of 1.867 x 10-11y-1 (Söderlund et al., 2004), the present-day chondritic $^{176}$Lu/$^{177}$Hf value of 0.0336 and $^{176}$Hf/$^{17}$7Hf ratio of 0.282785 Bouvier et al. (2008).

### 5.4.3 Sr-Nd Radiogenic Isotope Analysis

Powdered core and modern river mud samples were leached in dilute acetic acid to remove carbonate before spiking with$^{149}$Sm-$^{150}$Nd, $^{87}$Rb and $^{84}$Sr isotope tracers. Dissolution and column chemistry used standard techniques (See Appendix 5).

# Chapter 6: The evolution of the river Nile and factors affecting the Nile cone sedimentary record

Laura Fielding[1], Yani Najman[1], Ian Millar[2], Peter Butterworth[3], Eduardo Garzanti [4], Giovanni Vezzoli[4], Dan Barfod[5] & Ben Kneller[6]

*1. Lancaster Environment Centre, Lancaster University, Lancaster, U.K.; 2. British Geological Survey, Keyworth, U.K.; 3. BP Egypt, Cairo; 4. University Milano-Biccoca, Milan, Italy; 5. SUERC, East Kilbride, U.K.; 6. University of Aberdeen, Aberdeen*

## Abstract

We present the first detailed multiproxy provenance study of Oligocene-Recent Nile

delta cone sediments, and show that the palaeodrainage of the Nile river and

composition of the sediments supplied to the delta cone have remained relatively

stable over the last 30 Ma.  Our study of detrital zircons and Sm-Nd bulk composition

of Oligocene-Recent Nile delta cone sediments shows that the Ethiopian Large

Igneous Province has been contributing detritus to the Nile since the uplift of the

Ethiopian Highlands at c.31 Ma. The detrital zircon signature of Nile delta cone sands

is dominated by grains derived ultimately from the Arabian Nubian Shield and post-

collisional granites related to the Pan-African Orogeny. A subordinate population of

grains derived from pre-Neoproterozoic cratonic basement is also present. The

signature of the cone sands is identical to that seen in recycled Phanerozoic

sedimentary cover sequences which overlie the Arabian-Nubian Shield and cratonic

basement rocks, and it is these sedimentary rocks that are thought to be the source

of most zircons found in the Nile sediments. Pre-Neoproterozoic zircons are more

common in Oligocene and Pliocene cone sands than in the Miocene and Pliocene.

This is interpreted as greater input from locally eroded sediments from the Red Sea

Hills at these times, due to uplift of the Red Sea Hills in the Oligocene, and infilling of

the Nile canyon by Red Sea Hills detritus in the Pliocene following down-cutting

during the Messinian Salinity Crisis. The relative continuity of the provenance signal

of the Nile sediments across 30 Ma of changing climate shows that aeolian dust,

which is commonly invoked as an end-member in modern river studies of the Nile, is

unlikely to be an important source to the delta cone samples studied here. In Nile

cone sands, the proportion of stable heavy minerals increases markedly down

section, indicating extensive diagenetic dissolution of less stable minerals. Tracer

isotopes in the Nile cone muds do not show a systematic variation with depth and

time, but instead are controlled by provenance and mineral sorting effects.

## 6.1 Introduction

The availability to this project of samples of Oligocene to Recent Nile delta cone sediment provides a unique opportunity to research the evolution of the River Nile over the last 30 Ma. In Chapter 5, it is demonstrated that the flow of the Blue Nile was initiated by Miocene times, as documented by the presence of Cenozoic detrital zircons derived from the Ethiopian Highlands in Miocene Nile delta rocks. Oligocene initiation of flow is inferred using tracer isotope studies.

This paper expands on the data presented in Chapter 5, and considers the changing distribution of U-Pb age and Hf isotope composition of detrital minerals, together with other provenance proxies in the Nile cone since the Oligocene. Values from this study are compared with published isotope data from the various possible Nile river source regions in order to study changes in the supply of sediment to the delta over the last 30 Ma and hence determine the river's palaeodrainage evolution.

The present day Nile is made up of three main tributaries, the Blue Nile, White Nile and Atbara (Figure 6.1). The mean water discharge during times of peak flow is dominated by the Blue Nile (68%), followed by the White Nile (10%) and Atbara (22%) (Williams and Adamson, 1982). The vast majority of White Nile sediment load is trapped in extensive swamps in South Sudan (the Sudd marshes, Figure 6.1), and does not reach the main Nile trunk.

The White Nile drains Archaean – Proterozoic rocks (in part remobilized during the Neoproterozoic) of the Congo and Tanzania Craton, and extends through the Saharan Metacraton (Abdelsalam, 2002) in South Sudan. In its terminal tract, the White Nile has an extremely low gradient due to its positioning along the floor of an ancient lake

that occupied its valley as long ago as 400 ka before present (Williams and Williams, 1980).

The Blue Nile and Tekeze-Atbara are sourced in the Ethiopian Highlands, where they drain Cenozoic flood basalts, Neoproterozoic basement rocks of the Arabian-Nubian Shield and largely Mesozoic cover sequences. Uplift of the Ethiopian Highlands in the Oligocene may have led to the initiation of flow in the Blue Nile (Gani et al., 2007; Pik et al., 1999; Pik et al., 2008).  However, there is no agreement in the published literature regarding the timing of initiation of such flow.

The geology of the Nile source regions has largely been shaped by the events of the Pan-African Orogeny (Kröner and Stern, 2004), when east and west Gondwana collided to form 'Greater Gondwana' at the end of the Neoproterozoic. This orogeny involved the collision of ancient cratons such as the Congo-Tanzania craton and the Saharan Metacraton with juvenile oceanic island arcs of the Arabian Nubian Shield. Evolution of the Nile has also been strongly controlled by the Cenozoic tectonic history of northeast Africa, with magmatism in the Oligocene leading to development of the East African rift (Ebinger, 2005), uplift of the Nile source regions in the Ethiopian Highlands, and opening of the Red Sea rift leading to uplift on the rift flanks facing the Nile basin.

**Figure 6.1 Modern river samples and hinterland geology of Nile river source areas.** Inset shows location of map as boxed area. Map modified from (al-Miṣrīyah, 1981; Johnson, 2014; Kazmin, 1972; Ministry of Energy and Mines, 1981).

## 6.1.1 Geology of Nile source regions

The Nile cuts a complex mosaic of terrains that were brought together during amalgamation of East and West Gondwana during the Pan-African orogeny. The modern Nile cuts rocks of the Congo and Tanzania cratons, Saharan Metacraton and Arabian Nubian shield. Together with largely Mesozoic cover sequences and Cenozoic volcanic rocks, this represents a complex mix of potential source rocks to the delta.

The Archaean Tanzanian Craton covers an area of over 3,500,000 km$^2$ (not solely drained by the Nile) with an average elevation of 1260 m (Cahen et al., 1984) and sits to the east of the Congo Craton. The Congo craton is also drained by the White Nile, and forms part of the West African Central Belt which formed between 2.5 and 2.0 Ga ago (Cahen et al., 1984; Goodwin, 1996; Tchameni et al., 2000; Walraven and Rumvegeri, 1993).

The term Saharan Metacraton refers to an area of pre-Neoproterozoic continental crust which has, in part, been highly remobilised during the Neoproterozoic Pan-African orogeny (Abdelsalam, 2002). It covers an area of 5,000,000 km$^2$ and extends from the Arabian Nubian Shield in the east to the Tuareg Shield in the west and the Congo Craton in the south. Much of the Saharan Metacraton is overlain by Phanerozoic 'Nubian' sedimentary rocks and desert sands (Abdelsalam et al., 2011). The poor exposure of the region means that the Saharan Metacraton and its relationship to adjacent blocks are poorly understood. The southern boundary is not well defined, but is taken to be marked by the Oubangides orogenic belt which separates it from the Congo-Tanzania Craton (Abdelsalam, 2002). Little modern geochronology has been carried out on rocks of the Saharan Metacraton. Legacy Rb-

Sr and U-Pb data quoted by Abdelsalam (2002) indicate a range of Late Archaean and Palaeoproterozoic protolith ages, with significant crustal reworking and addition of new crust in the Neoproterozoic. However, Bea et al. (2011) report SHRIMP U-Pb zircon ages as old as 3.22 ± 0.04 Ga for gneisses in the Uweinat and Gebel Kamil regions of the Western Desert in southernmost Egypt.

The Arabian Nubian Shield (Figure 6.1) is a collage of Neoproterozoic (c. 870-670) microcontinents and juvenile island arcs, overlain by younger Mesozoic sedimentary and Cenozoic volcanic rocks, and cut by voluminous granitoid intrusions (Johnson and Woldehaimanot, 2003; Kusky and Matsah, 2003; Stern, 1994). Pre-Neoproterozoic crust is only sporadically exposed. Oceanic subduction and arc-formation began at 870 Ma followed by terrane amalgamation associated with closure of the Mozambique Ocean and amalgamation of East and West Gondwana took place between c. 780 Ma and c. 600 Ma (Johnson and Woldehaimanot, 2003).

To the west of the Red Sea, the oldest arc terranes (> 800 Ma) of the Arabian Nubian shield occur in the south, in Ethiopia, Eritrea and Sudan (Johnson and Woldehaimanot, 2003). In contrast, ophiolitic rocks of the Eastern Desert of Egypt range in age from 810 to 720 Ma (Ali et al., 2010), and are overlain by younger (c.600 Ma) volcanic sequences (e.g. Breitkreuz et al. (2010)).

The final closure of the Mozambique Ocean (c.600 Ma) led to amalgamation of the Saharan Metacraton, Congo and Tanzanian cratons with the Arabian Nubian Shield. After collision, late orogenic uplift and extension led to the exposure of Late Neoproterozoic gneiss domes (Johnson and Woldehaimanot, 2003). Erosion of the

mountain belt led to deposition of fluvial and marine Cambro-Ordovician "cover" sediments, which blanketed much of North East Africa (Kolodner et al., 2006a).

Previous studies of the cover sediments in regions adjacent to the study area (i.e. Libya, Jordan, and Israel) have put forward potential Phanerozoic palaeogeographies for the region during deposition of the sedimentary cover succession. Altumi et al. (2013) and Kolodner et al. (2006a) record a trend from arkosic basal sediments with a dominant, narrow Late Neoproterozoic zircon population, to quartz arenites with an increasing number of older zircons (peaks at ca. 1000, 2000 and 2500 Ma) in the overlying sediments. Meinhold et al. (2011) ascribe the textural and mineralogical maturity of the bulk of the cover, and the provenance of the sediments, to degrees of recycling and long distance transport. Long-distance transport was invoked to explain the c.1000 Ma zircon population for which an obvious basement source in the Saharan Metacraton or Arabian Nubian Shield has not been discovered (Kolodner et al., 2006a; Meinhold et al., 2011).

The Cenozoic continental flood basalts that dominate much of the Ethiopian Highlands are associated with East African rift-related magmatic activity (Buck, 2006; Ebinger, 2005). The order in which rifting developed is a matter of some dispute. Pre-rift basaltic magmatism is said to have initiated around 31 Ma (Baker et al., 1996; Rochette et al., 1998; Ukstins et al., 2002) and subsequent uplift related to magmatic upwelling caused faulting within what is now the Ethiopian Highlands. Uplift was succeeded by formation of the Afar depression and shield-volcano building episodes between 26 and 22 Ma (e.g. Choke and Guguftu shield volcanoes) (Gani et al., 2007). During these periods, a significant volume of rhyolitic lava and ignimbrites was

emplaced. These latest Oligocene to Miocene felsic rocks are a fertile source of zircons to the modern Nile (Chapter 4 and 5).

### 6.1.2 Geographic distribution of Nile sediment sources

There are four potential source areas for the Nile cone sediments: the Sahara Desert, the Red Sea Hills, Ethiopian Highlands and White Nile source regions (Figure 6.1).

The Red Sea Hills (E. Egypt and N. Sudan) run parallel with the Red Sea and extend from Egypt into northern Sudan. This area is comprised of Neoproterozoic plutonic rocks and meta-volcanic basement of the northern Arabian Nubian Shield, overlain by Phanerozoic sedimentary deposits and Eocene carbonates (Daumain et al., 1958).

The Ethiopian Highlands **is** drained by the Blue Nile and Tekeze-Atbara rivers and is comprised of Neoproterozoic basement of the southern Arabian Nubian Shield, largely Mesozoic sandstones and carbonates overlain by Oligocene (~30 Ma) flood basalts (Hofmann et al., 1997; Mohr and Zanettin, 1988).

The White Nile Source Regions in Burundi, Rwanda, Uganda, northern Tanzania, western Kenya,  South Sudan include the Precambrian Saharan Metacraton and 1000 Ma Congo and Tanzania Cratons with overlying Mesoproterozoic to Mesozoic sedimentary rocks (Abdelsalam, 2002).

The Western Desert in southwest Egypt does not currently drain into the Nile but in the model of Issawi and McCauley (1992), may have contributed sediment to the delta during the Late Eocene.  The Western Desert is situated upon the Saharan Metacraton and overlying Phanerozoic sedimentary rocks (Abdelsalam, 2002).

### 6.1.3 The Nile Cone Sediments

The offshore Nile cone is subdivided into three major basins; the western, central and eastern provinces (Bellaiche et al., 2001) and has been the source of most of the gas production in the Mediterranean for many years (El Diasty and Moldowan, 2013).

Deposition in the delta's current location began in the late Oligocene (Issawi and McCauley, 1992; Said, 1981; Salem, 1976). Prior to this, the delta developed onshore in the Eocene (38-35 Ma) in the region of Fayoum (Salem, 1976; Underwood et al., 2013) and began to prograde out into its current position in the Mediterranean as a result of sea level fall and the receding Tethys Ocean.

Marine conditions and sediment accumulation continued in the Mediterranean until the end of the Miocene (Dolson et al., 2001), when the Mediterranean basin became cut off from the Atlantic, resulting in a c. 2000 metre fall in base level (the Messinian Salinity Crisis, 5.96 – 5.33 Ma), and the desiccation of the Nile cone (Garcia-Castellanos et al., 2009; Krijgsman et al., 1999). Sapropel accumulation alternated with evaporite deposition.  Evaporites formed during relatively arid periods which coincided with precession minima, whereas sapropels were deposited during relatively humid periods which coincided with precession maxima (Krijgsman et al., 1999). At the end of the Messinian Salinity Crisis the subsequent Zanclean flood rapidly filled the Mediterranean basin. An increase in sedimentation rate in the Nile delta cone occurred during the Late Pliocene – Early Pleistocene as a result of increased uplift, rainfall and subsequent denudation in the Ethiopian Highlands and northern hemisphere ice sheet growth (Palacios, 2013).

### 6.1.4 The provenance signal of Nile sediments

In Chapter 4, it was shown that modern Blue Nile, White Nile and Tekeze-Atbara sands sampled upstream of the confluence with the Nile contain zircon populations that show a significant contribution from Arabian-Nubian Shield basement, and are strongly influenced by geomorphological features such as the Sudd marshes and the Gezira Fan (Figure 6.1). White Nile sands collected south of the Sudd marshes in Uganda are dominated by grains derived from cratonic basement. Zircon grains in these sediments are trapped in the marshes of South Sudan, and little material makes its way into the downstream main Nile. Instead, White Nile sediments south of Khartoum show a strong Blue Nile zircon signature, resulting from overflow of the Blue Nile across the Gezira Fan during Pleistocene flood events, and back-flow of Blue Nile sediment into the White Nile during times of modern peak flow. Blue Nile and Atbara sediments sampled in Sudan and Ethiopia show contributions from Arabian Nubian Shield basement rocks, Phanerozoic cover sequences and Cenozoic volcanic rocks.

Modern river sands collected in the main Nile trunk (i.e. downstream of the Atbara confluence) in Sudan and Egypt show zircon age and εHf value distributions that are indistinguishable from those in Precambrian source rocks and in the voluminous Phanerozoic cover rocks that blanket north Africa (Chapter 4). The data distributions are similar to those described by Iizuka et al. (2013) for a sample from the modern Nile delta, and by Be'eri-Shlevin et al. (2009) for zircons in Quaternary – Recent Israeli coastal sands, which are derived by long-shore drift along the north coast of Africa from the Nile delta. Be'eri-Shlevin et al. (2009) conclude that the sands are predominantly recycled products of Phanerozoic sedimentary cover sequences.

In Chapter 4, U-Pb analysis of detrital rutile from the Nile catchment are reported, demonstrating that rutile is not an effective provenance indicator in this region of strong Pan-African metamorphic overprint. Rutile U-Pb ages record the time of cessation of Pb volume diffusion during cooling below ~ 500 °C (see discussion in Bracciali et al. (2015)). All analysed samples show a broad range in ages between 750 and 500 Ma, with maxima between 550 and 650 Ma.

In Chapter 4, Sr, Nd and Hf isotope data are also reported for modern mud samples from the Nile River and from dry wadis in the Nile catchment in the Red Sea Hills and Western desert in Egypt. Blue Nile and Atbara muds are dominated by the input of mafic volcanic material from Ethiopia, and have positive εNd values (up to +6) and low $^{87}Sr/^{86}Sr$ values. In contrast, muds eroded from Phanerozoic cover rocks in dry wadis of the Red Sea Hills have low εNd values (c. -6), and relatively high $^{87}Sr/^{86}Sr$. Sediment samples the Egyptian Nile trunk, collected before the construction of major dams on the river (Shurki 1950), show intermediate values, interpreted as resulting from mixing of Ethiopian basaltic detritus with sediments derived from erosion of cover sequences along the course of the Nile (Chapter 4). Padoan et al. (2011) recorded major changes in the Sr and Nd ratios along the course of the Nile throughout Uganda, Sudan and Ethiopia. High $^{87}Sr/^{86}Sr$ and low εNd in muds from the Ugandan White Nile reflect Archaean cratonic sources, whereas the River Sobat shows lower $^{87}Sr/^{86}Sr$ and higher εNd, reflecting sources in the crystalline basement of the Ethiopian Highlands. The contribution of mud from the upstream White Nile to the Nile trunk is thought to be minimal, again due to trapping of sediment in the Sudd marshes.

The Levantine basin is also influenced by sediments from the Nile. Krom et al. (1999) studied Sr ratios of the surface sediments of the Levantine basin which were found to be a mixture of 'Nile' sediment (characteristic of northern Sudan) and aeolian contributions from the Sahara. Krom et al. (2002) went on to analyse biostratigraphically dated core from the Nile cone dating back to 7000 years. Wetter climates in Ethiopia were found to correlate with higher river flow, but reduced sedimentation rates and ultimately a less Blue Nile-like Sr signature in the delta (Williams et al., 2015).

Pleistocene – Holocene hemipelagic sediments from the Western province of the Nile cone were analysed by Revel et al. (2010). Sr and Nd isotopes highlight the importance of aeolian contribution during arid periods and the dominance of the Nile River during wet periods.

Chapter 5 presented the only isotope-based study of pre-Pleistocene sediments from the Nile cone. Ethiopian-derived detrital zircons were identified in delta cone sediments as old as Miocene (Burdigalian, c. 17 Ma). These zircons are absent in Oligocene samples, but Sr-Nd isotope modelling indicates that Ethiopian flood basalt-derived detritus is present in samples as old as early Oligocene (Rupelian, c. 31 Ma).

## 6.2 Analytical Methods

Medium sand, silt and mud samples were taken from Nile delta cone cores of Oligocene (27.5 and 31 Ma), Miocene (15.2, 15.5 and 17 Ma), Pliocene (2.65-3.25 Ma) and Pleistocene (1.295 Ma) age (Appendix 1). The samples were provided by BP Egypt, who have constrained their age using biostratigraphy. Samples were collected as stratigraphically continuously as possible with some lateral variation. Samples were collected from the east, west and central Nile delta. Sand samples from Oligocene and Miocene cores were lithified and well consolidated, whereas Pliocene and Pleistocene samples were unconsolidated and friable. All sand samples obtained from the core were large enough for separation of sufficient minerals for analysis without amalgamation, so each analysis faithfully represents the Nile cone at each depth interval.

Detailed analytical methods for techniques used in this study are given in Chapter 3 (*Analytical Methods*).

Zircon and rutile grains were separated using standard methods, then hand-picked and mounted in epoxy disks and polished to reveal their interiors. All zircon grains were imaged using cathodoluminescence prior to analysis in order to allow targeting of laser spots. U-Pb analyses for both zircon and rutile were carried out at the NERC Isotope Geosciences Laboratory (NIGL), using a single collector Nu-Attom mass spectrometer with one of three New Wave laser systems, typically using a 35µm laser spot. Hafnium isotope composition of zircons was measured at NIGL using a Thermo-Electron Neptune Plus mass spectrometer, coupled to a New Wave 193UC

or 193FX Excimer laser. A 50μm spot was used, targeting previously dated zircon domains.

Plagioclase and white mica were separated from the light fraction remaining after zircon and rutile separation. Ar-Ar analyses were carried out at SUERC, East Kilbride, using a GVi instruments ARGUS 5-collector mass spectrometer using a variable sensitivity Faraday collector array in static collection (non-peak hopping) mode (Mark et al., 2009; Sparks et al., 2008).

Mud samples for Sr, Nd and Hf analysis were leached in dilute acetic acid to remove carbonate before spiking with $^{149}$Sm-$^{150}$Nd, $^{176}$Lu-$^{180}$Hf, $^{87}$Rb and $^{84}$Sr isotope tracers. Standard dissolution methods and ion-exchange chromatography were used to separate elements of interest. Sr and Nd isotope compositions were measured at NIGL on a Thermo-Electron Triton mass spectrometer, using dynamic multicollection. Hf isotope composition was analysed in static mode on a Thermo-Electron Neptune mass spectrometer coupled to a Cetac Aridus II desolvating nebuliser.

XRF major and trace element analysis was carried out at the Open University in Milton Keynes. See Analytical Methods for more details (Chapter 3 and Appendix 2).

Petrographic analysis, and heavy mineral analysis of sands and muds were carried out using methods modified from Garzanti et al., 2006 and Garzanti and Andò, 2007. Split aliquots of each bulk sample were impregnated with Araldite and prepared as standard thin sections and stained with alizarine red to distinguish calcite from dolomite. In each thin section, 400 points were counted for petrography according to the Gazzi-Dickinson method (Ingersoll et al., 1984). For heavy mineral analysis, between 200 and 270 transparent heavy minerals were counted in grain mounts by

the "area method" (Galehouse, 1971).  See Chapter 3, *Analytical Methods* for more details.

## 6.3 Results

### 6.3.1 U-Pb and Lu-Hf analysis of zircon

In Chapter 5, U-Pb zircon data were presented for Nile delta cone sediments, but focussing exclusively on young grains derived from the Ethiopian Large Igneous Province. Here we discuss the overall age distribution of the detrital zircon populations, and couple this with LA-ICPMS hafnium isotope analysis on grains from selected samples.

All Nile cone samples from Oligocene to Pleistocene are dominated by a c.600 Ma peak in zircon age distributions (Figure 6.2). In addition, there are subordinate populations between 700-850 Ma and at c.1000 Ma. Sparse Archaean and Palaeoproterozoic grains are also present in each sample in different proportions. A Cenozoic (15-32 Ma) population is present in many Miocene to Pleistocene samples. Grains of this age have not been identified in Oligocene samples (Chapter 4).

*In situ* analysis of U–Pb and Lu–Hf (Figure 6.3) on individual zircon grains helps to constrain the tectonic setting in which the magmas formed. Iizuka et al. (2013) use the age and εHf distributions of zircons derived from juvenile magmatic arcs to define an 'arc mantle' field in hafnium-age space.  In the age range of interest here (mostly 1200-600 Ma), positive εHf values (>4) indicate formation in a juvenile oceanic island arc-like setting, whereas negative εHf values reveal a more cratonic setting.  In the plots that follow, we include a field for 'cratonic influence', which is defined by the hafnium isotope composition of detrital zircons from sample WN7-17

(Victoria Nile at Murchison Falls, Uganda), including zircons formed by re-melting of this crust at c. 500 and 1000 Ma (Chapter 3).  This field represents typical north African Archaean basement.

Hf analysis on zircon grains from the Nile cone (Figure 6.3) highlights the difference in the proportion of arc-like grains originally derived from Arabian Nubian Shield source areas (the Ethiopian Highlands and Red Sea Hills basement and such grains recycled through the Phanerozoic cover) versus cratonic-derived grains originally sourced from the Saharan Metacraton and Congo and Tanzanian cratons in the White Nile source regions, and also found recycled in Phanerozoic sedimentary cover. All Nile cone samples show grain populations between 650 and 900 Ma being dominated by arc-like signatures ($\varepsilon$Hf >4), with an appreciable population with less juvenile values, particularly at c. 600 Ma. Sparse grains at c.1000 Ma show both juvenile and cratonic-dominated signatures, and Palaeoproterozoic and Archaean grains have predominantly cratonic signatures with negative $\varepsilon$Hf values. Inter-sample differences in the zircon populations are outlined below.

**Oligocene, 31 Ma (Rupelian) West Nile Delta Cone – sample ND35**

74% of the 550-650 Ma grains that fall within the Arabian Nubian Shield collision phase (550-650 Ma – Figure 6.3) show involvement of cratonic material with $\varepsilon$Hf values as low as -37 and the remaining 26% of grains have arc-like $\varepsilon$Hf values. The c.1000 Ma population is dominated by arc-like grains which make up 62% of the population and 38% of crustal grains showing $\varepsilon$Hf values as low as -26. There are no Cenozoic grains in the Oligocene sample and a small number of Palaeoproterozoic and Archaean grains with cratonic $\varepsilon$Hf as low as -8 are present.

**Oligocene, 27.5 Ma (Chattian) West Nile Delta Cone – sample ND31**

This Upper Oligocene sample shows much the same zircons populations, with a slightly reduced number of cratonic Archaean grains (Figure 6.2). 57% of all grains analysed show juvenile εHf values, with the majority of those juvenile grains falling within the Arabian Nubian Shield arc formation or collision phase (Figure 6.3). There is a distinct gap between the juvenile and cratonic c. 600 Ma population during the final stages of the Pan-African orogeny, and not a continuous spread of εHf values.

**Miocene, 17 Ma (Langhian) West Nile Delta Cone – sample ND10**

62% of grains in the 550-650 Ma population are cratonic and extend down to an εHf value of -15 (Figure 6.3). Unlike the Oligocene sample, there are no Palaeoproterozoic (2000-2500 Ma) grains present in this sample.

Two younger 15.5 Ma, Burdigalian samples (ND26 and ND31) have similar U-Pb zircon age distributions to the Langhian sample (Figure 6.2), with the exception that ND31 has a significantly higher proportion of grains between c. 650 and c. 900 Ma than the other two samples. Cenozoic grains in these additional samples are relatively common, with grains ranging from 15 to 32 Ma.

**Pliocene, 3 Ma (Piacenzian) West Nile Delta Cone – sample ND08**

In this unconsolidated Pliocene sample from the Western Nile Delta, 27% of all grains analysed have a juvenile εHf signature and fall within the Arabian Nubian Shield arc formation and collision phase (600-800 Ma) (Figure 6.3). There is also a cratonic grain population at c. 600 Ma with Hf values ranging from 0 to -35 and a scatter of grains within the cratonic field with 2500 – 3500 Ma depleted mantle model ages.

Mesoproterozoic, Palaeoproterozoic and Archaean grains all predominantly have cratonic εHf values.

**Pliocene, 2.65 Ma (Piacenzian) West Nile Delta Cone – sample ND01**

Unconsolidated sand samples from a Pliocene core show that for the 550-650 Ma population, 69% of the grains have crustal influence with εHf as low as -28, whilst 31% are arc-like (Figure 6.3). Grains between 650 and 900 Ma are dominated by arc-like signatures with sparse grains at c. 1000 Ma showing both juvenile and crust dominated signatures. There is a subordinate Palaeoproterozoic population with predominantly crustal εHf values, which is also seen in the Oligocene sample but is absent in the Miocene samples. There are two grains, both with crustal εHf values, which are older than 2500 Ma. A slightly older Pliocene sample (ND07) of 3.25 Ma was analysed for U/Pb only (Figure. 6.2) and shows a similar age distribution, with the addition of two Cenozoic grains (22 and 27 Ma).

**Pleistocene, 1.29 Ma (Gelasian) East Nile Delta Cone – ND41**

Unconsolidated sands from the most recent Nile cone sediments show crustal Hf values which make up 60% of the population between 550 and 650 Ma. Similar to the Miocene samples, εHf values are in the region of -15 which is less negative than values reached by Pliocene and Oligocene samples. There are no Palaeoproterozoic grains present in this sample, but there is a subordinate crust-like c.1000 Ma population. Four >2500 Ma grains, of negative or close to zero εHf values, are also recorded. An additional Pleistocene sample analysed for U-Pb only (ND42) (Figure 6.2), of the same age shows much the same age distribution, with three Cenozoic grains ranging from 24-26 Ma.
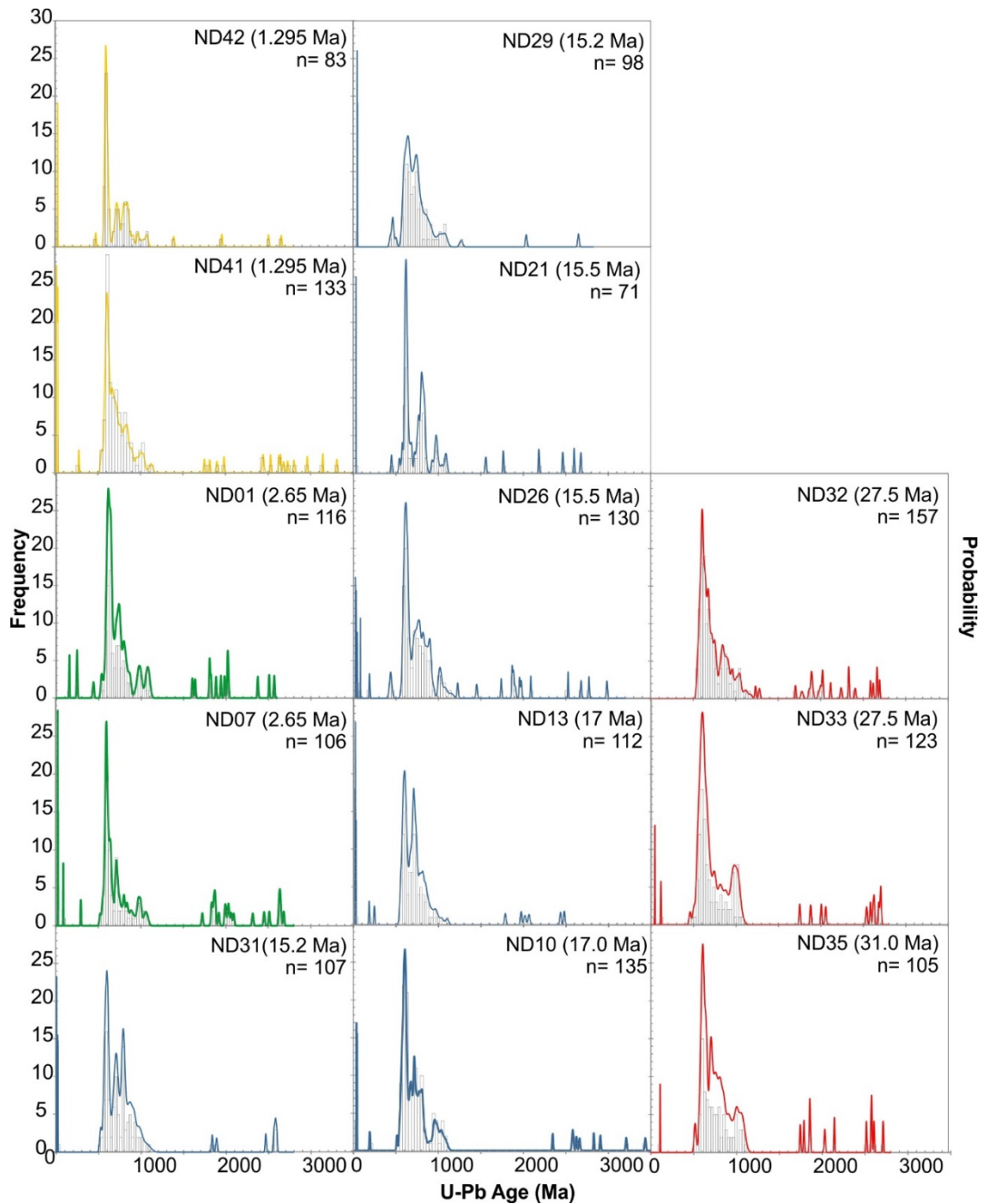
**Figure 6.2** Detrital zircon U-Pb age frequency and relative probability plots for each Nile cone sample analysed (Oligocene – Pleistocene). Concordant U-Pb age data are plotted as Red (Oligocene)/Blue (Miocene)/ Green (Pliocene)/ Yellow (Pleistocene) relative probability curves and grey frequency histograms. The number of concordant grains analysed for each sample = n. Only grains from ND01, ND08, ND10, ND35, ND31 and ND41 were then analysed for Hf (see Figure 6).
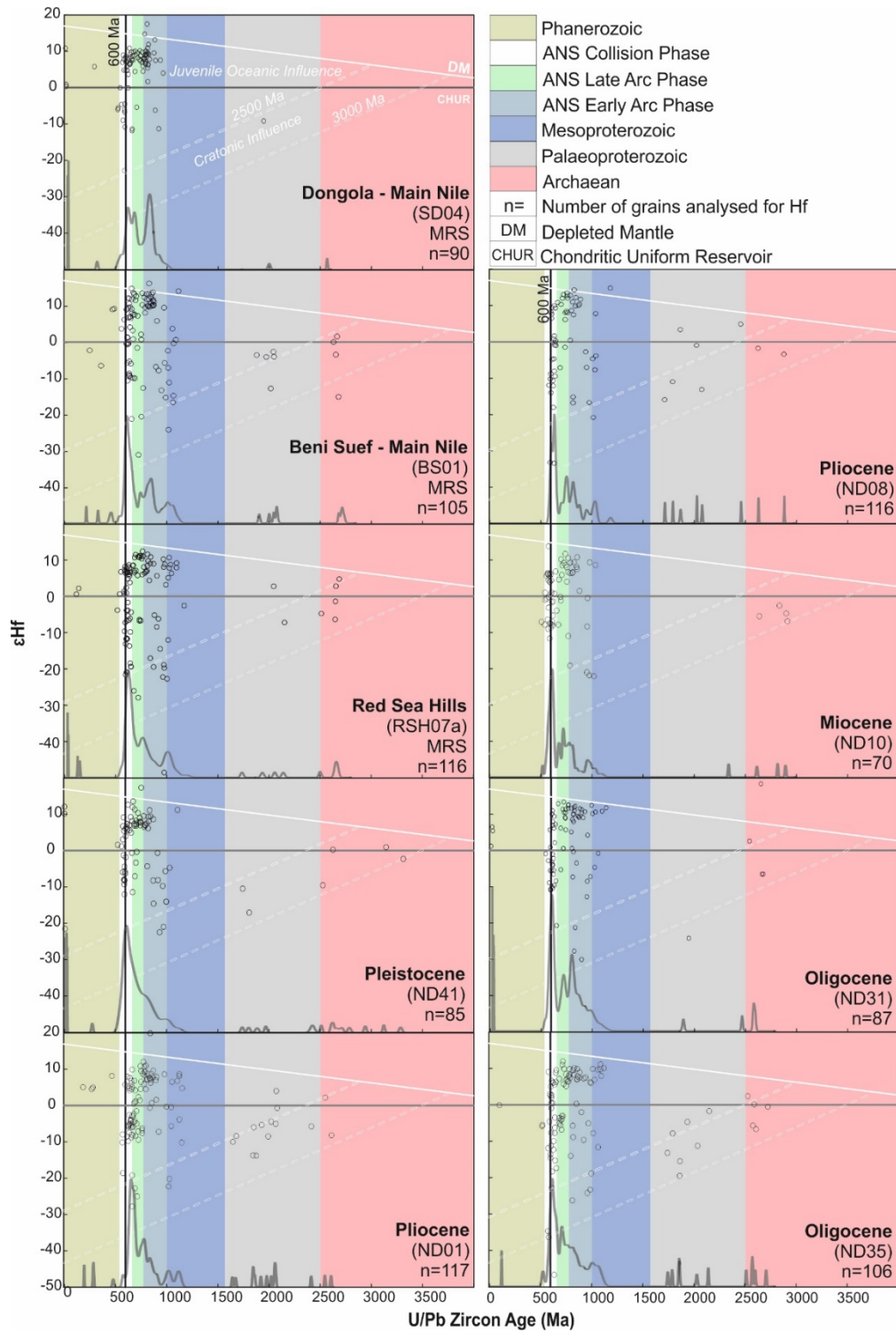
**Figure 6.3 Detrital zircon U-Pb age frequency and relative probability plots versus εHf.** Dashed grey lines represent the evolution of Hf in a typical zircon through time with depleted mantle model ages between 2500 and 3500 Ma. The black line marks 600 Ma, the approximate time of the Pan-African orogeny and the collision of the Arabian Nubian Shield with the Saharan Metacraton, Congo and Tanzanian cratons.

### 6.3.2 U/Pb Rutile, $^{40}Ar/^{39}Ar$ mica and plagioclase

In Chapter 4, it was discussed that $^{40}Ar/^{39}Ar$ mica, $^{40}Ar/^{39}Ar$ plagioclase and U/Pb rutile values of all the potential Nile delta source regions have a similar Pan-African signature with additional evidence of a minor population of Cenozoic grains in plagioclase data sets.

Rutile grains separated from five Oligocene to Pleistocene delta sands were analysed (Appendix 3). In each case, the data show a broad distribution in age, ranging from c. 800 to 500 Ma, with maxima between 580 and 620 Ma, reflecting a strong Pan-African overprint.  Although in detail each distribution is complex, the lack of discriminating features in rutile populations in potential source samples (Chapter 4) hinders any attempt to extract useful provenance information.

### 6.3.3 Rb/Sr, Sm/Nd and Lu/Hf bulk rock analyses

Sr and Nd tracer isotope data have previously been presented for mud samples from the Nile Delta cone (Chapter 5).  Here, we couple the data with new analyses from the <2 micron fractions, and include Hf-isotope data on the same samples.

The majority of delta cone samples define a prominent trend on a plot of $^{87}Sr/^{86}Sr$ against $^{87}Rb/^{86}Sr$ (Figure 6.4).  This trend extends to significantly more radiogenic $^{87}Sr/^{86}Sr$ values (0.7106) than seen in modern muds from the Nile River, and also higher than muds derived from the Red Sea Hills, which are proposed to represent the radiogenic end-member in the modern Nile system (Chapter 5).  Oligocene and Pliocene muds have higher $^{87}Sr/^{86}Sr$ (0.707 - 0.710) and $^{87}Rb/^{86}Sr$ compared to that seen in the Miocene and Pleistocene samples with $^{87}Sr/^{86}Sr$ between 0.705 - 0.709. The main exceptions to the dominant delta cone trend are the 27.5 Ma Oligocene

samples, and a minority of Miocene mud samples which overlap in composition with the Red Sea Hills end member.

Less than 2 micron fractions were separated from three Nile cone mud samples, and three Red Sea Hills modern muds. In most cases, the < 2 micron fractions have significantly higher $^{87}Sr/^{86}Sr$ and $^{87}Rb/^{86}Sr$ than the bulk muds. For the delta muds, the < 2 micron analyses plot on an extension of the dominant trend shown by the bulk data (Figure 6.4).

On a plot of εNd against $^{87}Sr/^{86}Sr$ , Nile cone data show considerable scatter to the right of a trend defined by mixing of average basalt Pik et al. (1999) with average Red Sea Hills mud (Figure 6.5). 27.5 Ma Oligocene and 2.65 Ma Pliocene samples tend to show the highest Sr ratios and lowest εNd (-2 to -4). Miocene (15.2 Ma) and Pleistocene samples have the lowest Sr isotope ratios and highest average εNd (0 to -3) (Figure 6.5). 17.0 Ma Miocene and 2.78 Ma Pliocene samples show intermediate values on average.

The Hf isotope compositions from the most mafic modern river mud samples from the Tekeze River have been used as an average for the Ethiopian flood basalts. These have been used in mixing calculations as there are no Hf data for the Pik et al. (1999) samples, and the Tekeze samples have similar isotope compositions to tholeiitic basalts from Ethiopia (Meshesha and Shinjo, 2010). The Tekeze samples plot on a steep trend, similar to alkali basalts described by Meshesha and Shinjo (2010) in Ethiopia. The Blue Nile samples plots directly between the basaltic end member and the Red Sea Hills muds (Figure 6.6). In a plot of εHf against εNd, Nile cone mud

samples scatter between average Ethiopian flood basalts and a crust dominated component with lower εNd and εHf.

The scatter of the Nile cone data show consistent groupings in many age populations (e.g. Holocene, 2.65 Ma Pliocene and both Oligocene populations etc.). By varying the Nd/Hf concentration ratio it is possible to generate a variety of mixing lines in order to model the observed compositions using a combination of Ethiopian basaltic material with average Red Sea Hills muds as end-members.
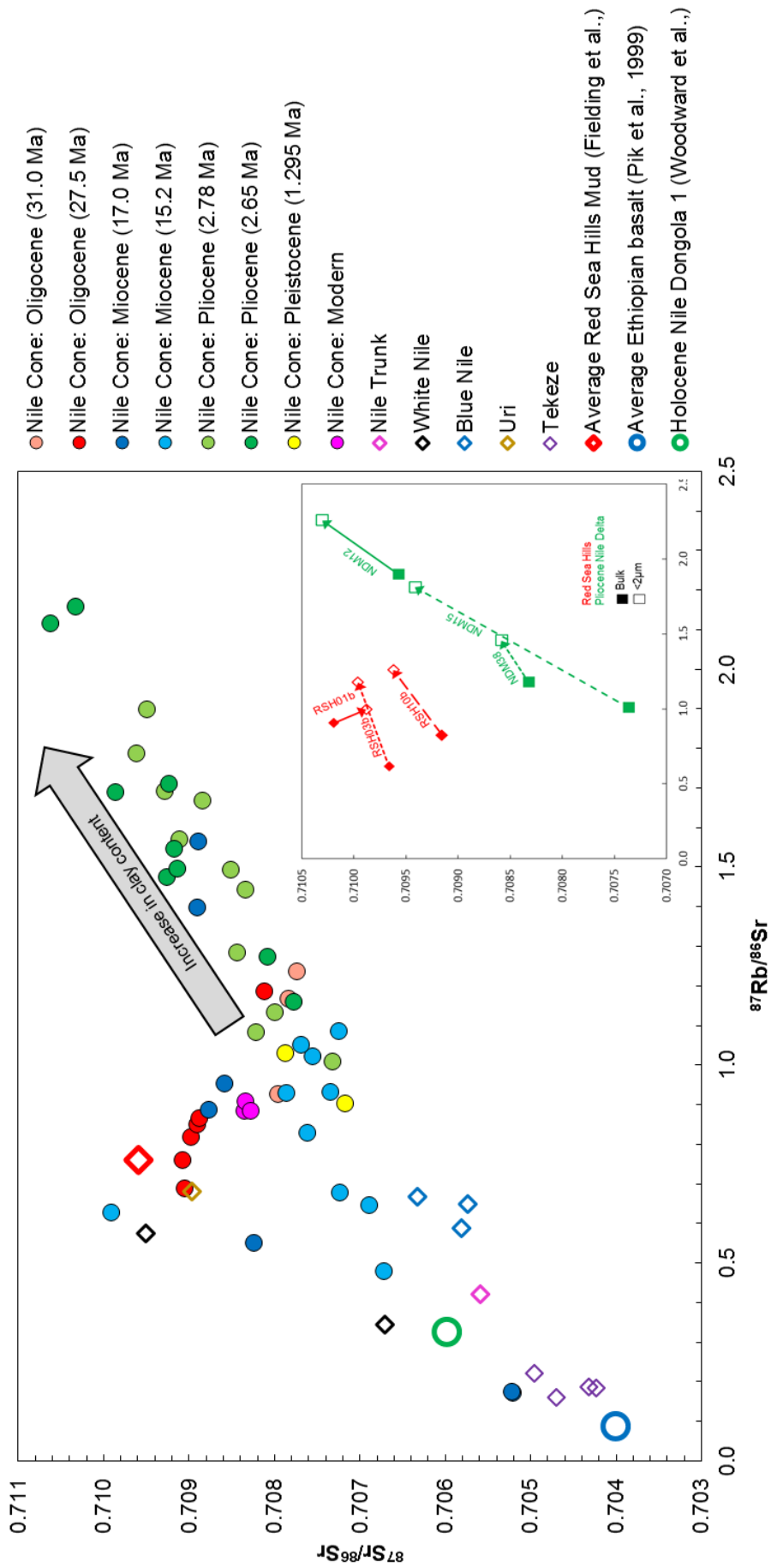
**Figure 6.4** $^{87}Sr/^{86}Sr$ against $^{87}Rb/^{86}Sr$ bulk data highlights the increase in radiogenic Sr in Nile cone samples. Nile cone samples plot on a consistent trend for much of the last 30 Ma, towards a highly radiogenic end member composition that is not represented by any lithology or source in the catchment. This end-member may represent material eroded from cover rocks and modified by mineral sorting in the fluvial system. **Inset:** A comparisson of the bulk (<63μm) and 2μm grain size fraction from the same sample shows an increase in the Sr ratio with a decrease in grain size.
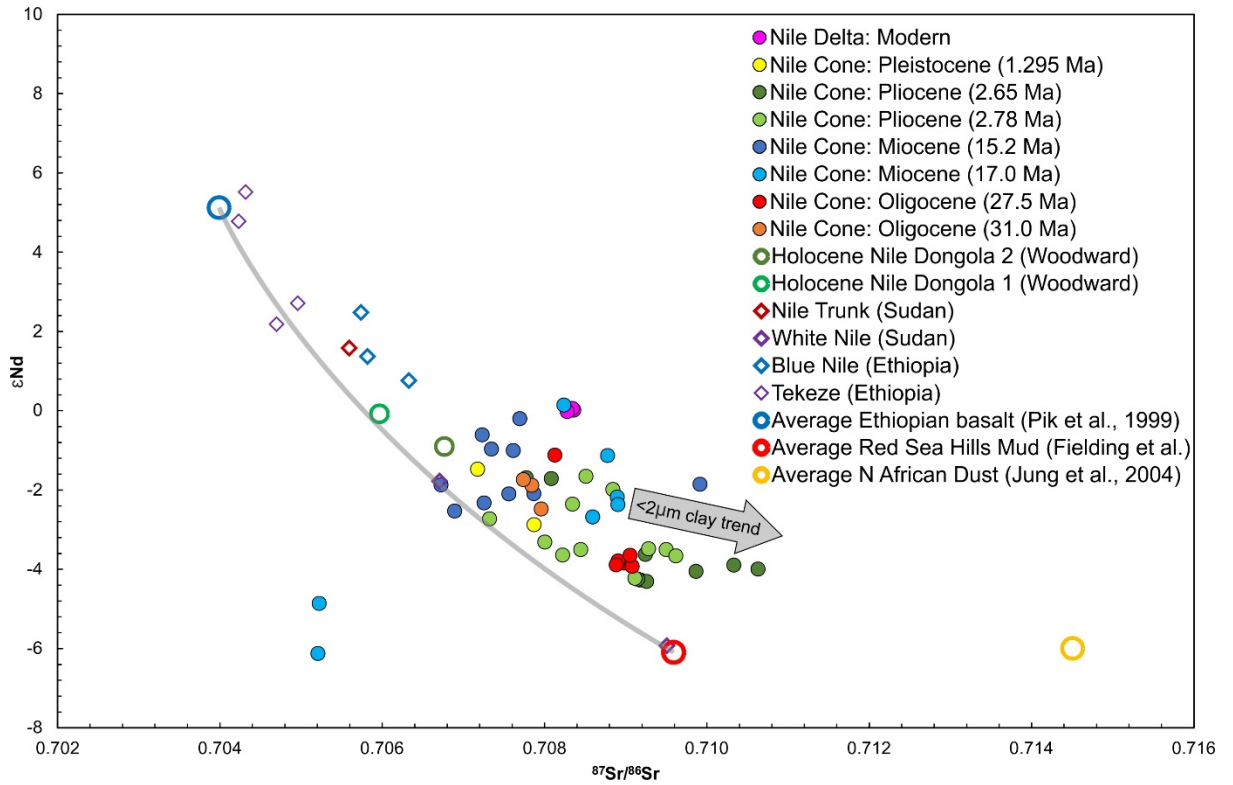
**Figure 6.5 Plot of εNd against $^{87}$Sr/$^{86}$Sr for Nile cone muds.** Data scatter between compositions typical of Ethiopian basalt (Pik et al., 1999) and muds derived by erosion of Phanerozoic cover sequences in the Red Sea Hills (Chapter 5). The scatter towards radiogenic Sr concentrations can be explained by mineral sorting of fine clay material during deposition of turbidite muds in the delta.
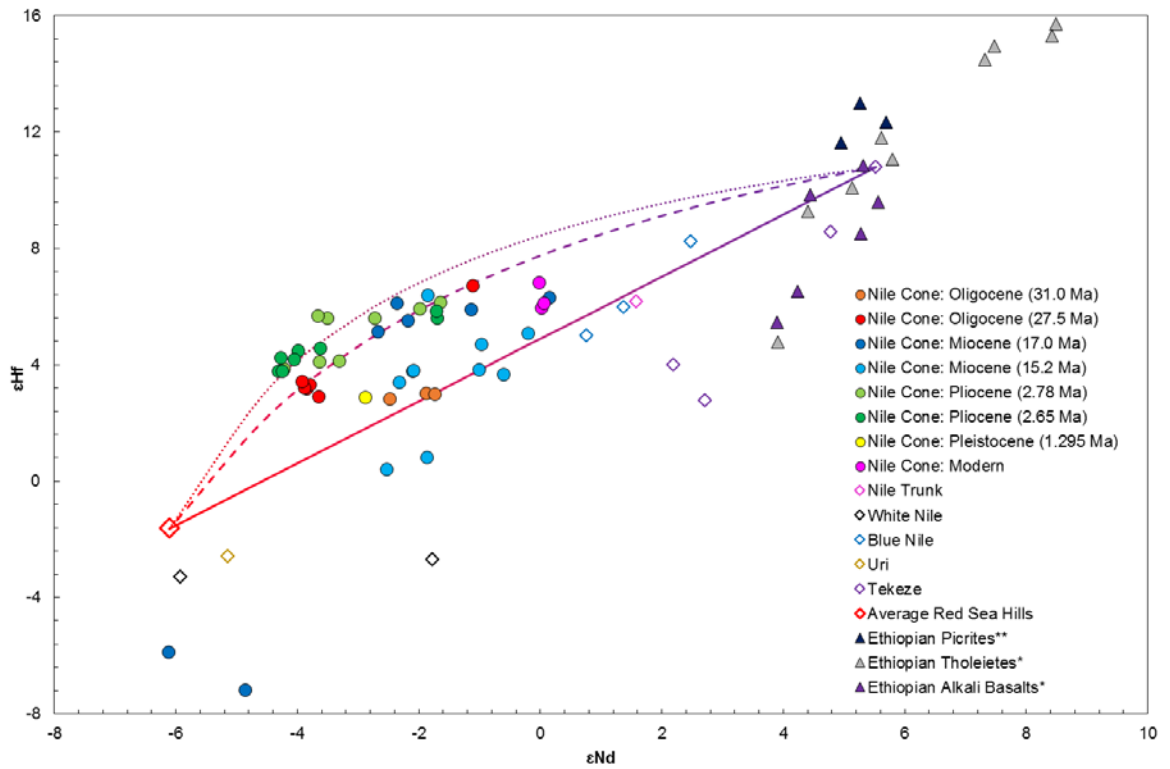
**Figure 6.6 εHf against εNd bulk rock analyses**. Nile cone sediments plotted against source area data from this study. * = Trachyte, tholeiite and Quaternary basalt data from Meshesha and Shinjo (2010). **= Ethiopian picrites from Nelson et al. (2012). Solid line represents mixing between average Red Sea Hills muds and a mafic Tekeze end member. The dotted line represents the Pliocene mixing trend for the same two end members. The dashed line represents the Pliocene, Chattian and Burdigalian mixing trend for the same two end members.

### 6.3.4 Petrography

The analysed sand samples range from feldspatho-quartzose to quartzose. Volcanic rock fragments, represented by frequently altered or glauconized grains with vitric, microlitic and lathwork texture, are present and most abundant in the Pliocene and Pleistocene samples. Few granitoid rock fragments and micas occur, along with minor sedimentary (shale, siltstone/sandstone, limestone, dolostone) and metamorphic grains (epidosite, porphyroid, chloritoschist). Carbonate grains are very rare throughout the section, never accounting for more than 0.3% of framework grains. This indicates that detritus from the Red Sea Hills was never significant, because carbonate rock fragments represent 10% to 50% of modern detritus from the Red Sea Hills.

Figure 6.7 shows that none of the analysed Nile cone sandstones compares closely with pre-Aswan High Dam Egyptian Nile sediments from previous petrographic studies (Garzanti et al., 2006). Our data show that only the very-fine-grained Pleistocene sample (ND42) contains common although extensively altered mafic volcanic rock fragments, common plagioclase and a moderately rich transparent-heavy-mineral assemblage. The other Pleistocene-Oligocene samples are significantly richer in quartz and contain either less volcanic rock fragments or less plagioclase, and poorer heavy-mineral assemblages. Volcanic detritus, however, occurs in higher proportions than in Red Sea Hills wadi sands from Eritrea and Sudan, or than in any Saharan samples (Garzanti et al., 2006).
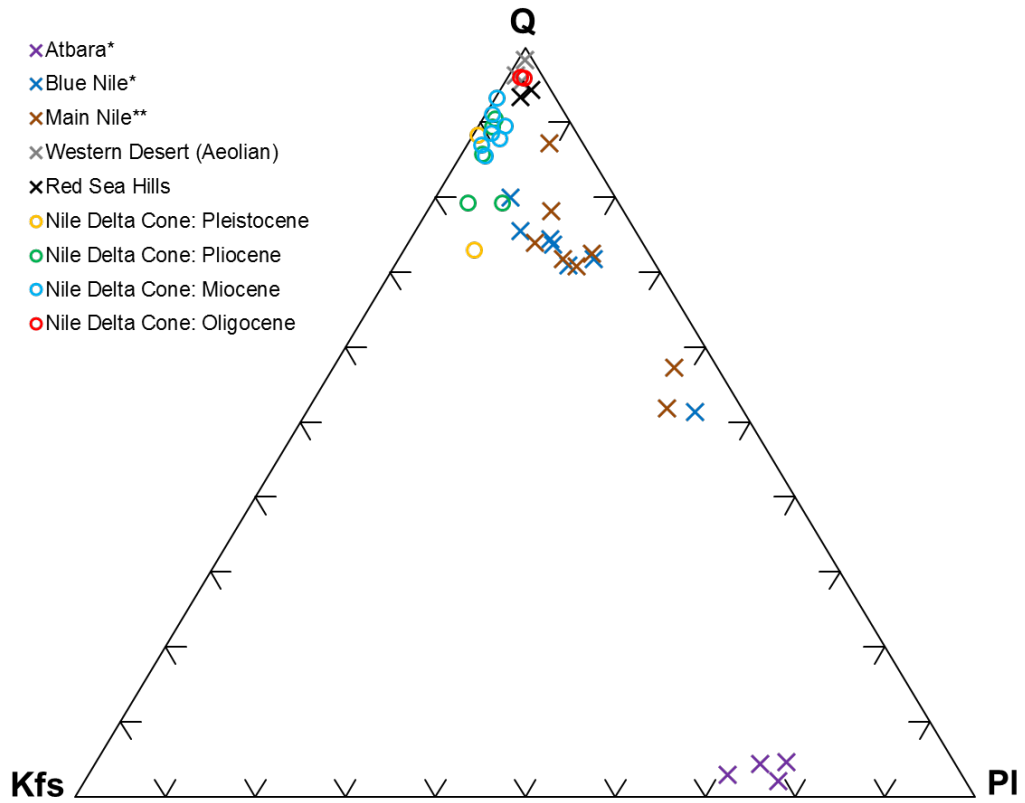
**Figure 6.7** A ternary plot showing the quartz (Q), k-feldspar (Kfs) and plagioclase feldspar (Pl) content of the Nile delta cone sands and source area petrography. *Data from Padoan et al. (2011) **Pre-Aswan dam Samples from the Egyptian Nile from Shukri (1950). Nile cone samples show an enrichment in quartz when compared to modern Nile sediments.

### 6.3.5 Heavy Mineral Analysis

Heavy mineral analyses are described below in terms of transparent heavy mineral concentration (tHMC) index (Garzanti and Andò, 2007) , which indicates the amount of transparent heavy minerals in the bulk sediment and the Zircon-Tourmaline-Rutile (ZTR) index (Hubert, 1962), which indicates the percentage of stable zircon, tourmaline, rutile and other Ti oxides over total transparent heavy minerals (Figure 6.8).

Sands:

Lower Pleistocene sands contain moderately poor (tHMC 1.1; ND41) to moderately rich (tHMC 4.9; ND42) amphibole-epidote assemblages with minor apatite, zircon, titanite, garnet, staurolite, tourmaline, kyanite and rutile (ZTR $5 \pm 2$).

Pliocene sands contain poor assemblages (tHMC $0.6 \pm 0.6$) with abundant epidote. Hornblende is common only in samples ND07 and ND09, which show higher tHMC indices. Other minerals include zircon, garnet, rutile, titanite, apatite, and minor tourmaline, staurolite and kyanite (ZTR $20 \pm 16$).

Miocene (Langhian to Burdigalian) sandstones contain extremely poor assemblages (tHMC $0.09 \pm 0.06$) dominated by zircon, rutile and tourmaline (ZTR $67\pm4$), with apatite, garnet and minor epidote, titanite, amphibole, kyanite, monazite and Cr-spinel.

Oligocene (Rupelian) samples contain extremely poor assemblages (tHMC $0.08\pm0.06$) dominated by zircon, rutile and tourmaline (ZTR $83\pm3$), with apatite and minor epidote, andalusite, garnet, Cr-spinel and titanite.

Muds:

Lower Pleistocene mud contains a poor (tHMC 0.8) amphibole-epidote assemblage with minor apatite, garnet, rare zircon, rutile and rare, probable clinopyroxene (ZTR 3).

Pliocene (Piacenzian) samples contain poor assemblages (tHMC 0.7 ± 0.5) with dominant epidote with Ti oxides, apatite, amphibole, zircon, tourmaline, titanite and garnet (ZTR 19 ± 16).

Miocene samples contain extremely poor assemblages (tHMC 0.09 ± 0.05) dominated by zircon, tourmaline and rutile (ZTR 62 ± 6) with apatite and minor epidote, garnet and Cr-spinel.

Oligocene samples contain extremely poor assemblages (tHMC 0.05 ± 0.05) dominated by zircon, rutile and tourmaline (ZTR 74 ± 6) with apatite, epidote and rare garnet.
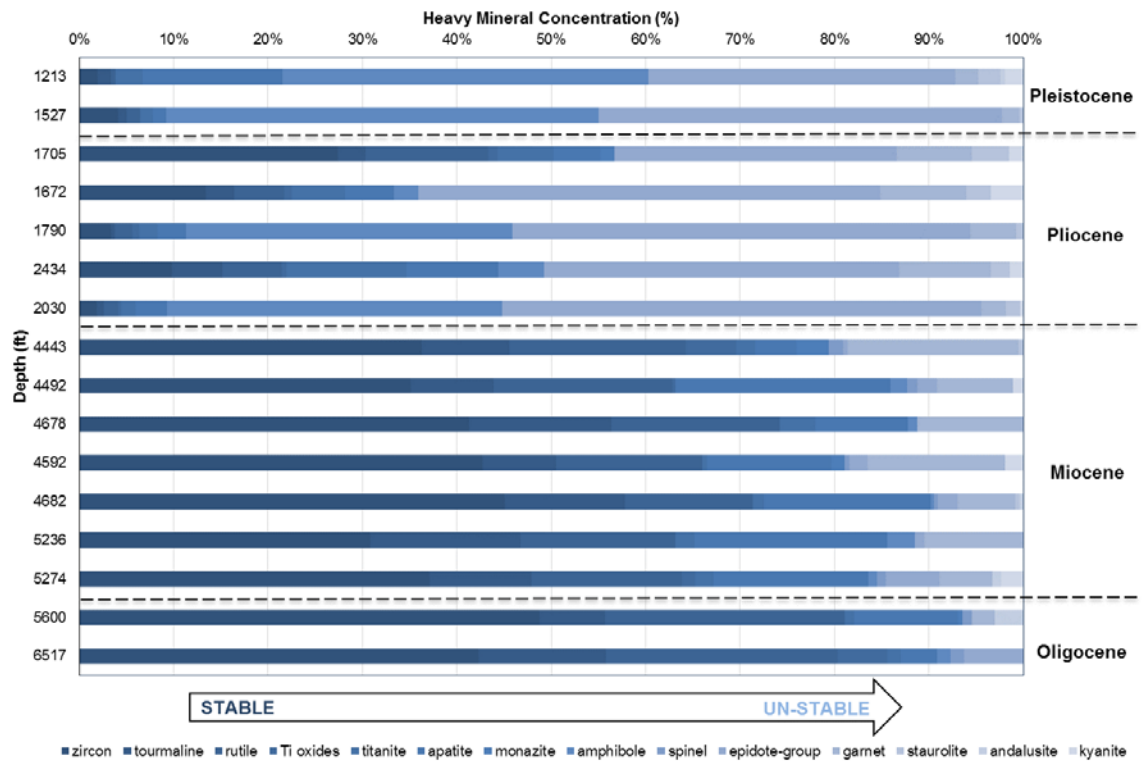
**Figure 6.8** Heavy mineral concentration of Nile cone sands (%) plotted against depth (ft). The decrease in the proportion of unstable versus stable heavy minerals in the Nile delta cone sands is ascribed to increasing intrastratal dissolution with increasing burial depth.

### 6.3.6 Major and Trace Element Geochemistry

Co and Ni concentrations from trace analysis were of particular interest as their quantities enable us to quantify the amount of mafic material (predominantly derived from the Ethiopian Flood Basalts and carried by the Blue Nile and Atbara) being delivered to the Nile cone. All delta samples show higher Co and Ni ppm than found in the White Nile (Padoan et al., 2011) and Red Sea Hills but still lower than found in the Blue Nile, Atbara and Tekeze samples (Padoan et al., 2011) (see Appendix 2). Unlike other bulk rock analyses (Sr, Nd and Hf), there is no variation of the signal over time and we do not see a separation between the Oligocene and Pliocene versus the Miocene and Pleistocene.

## 6.4 Discussion: contributing factors to the Nile cone signal

### 6.4.1 Provenance, palaeodrainage and the recycling of detrital zircons in Nile cone sediments

Detrital zircon populations in many African river sediments contain prominent Pan-African (c.600 Ma) age peaks, even where rocks of such age represent minor components of their drainage basins (e.g. in the Congo and Orange rivers; Iizuka et al. (2013)). This has been attributed to recycling of zircons through older sedimentary rocks deposited in drainage basins with different catchments (e.g. the Kalahari) (Iizuka et al., 2013). A similar conclusion has been reached by Be'eri-Shlevin et al. (2009) for recent Nile-derived sands deposited off the Israeli coast which derives most of its sediment from the Nile Cone via long-shore drift.

In Chapter 4, it was shown that the zircon age / hafnium isotope distribution of sands collected in upstream tributaries of the Nile are dominated by local bedrock geology. However, Figure 6.3 shows that modern river sands collected from the Nile trunk in Sudan (sample SD04) and Egypt (sample BS01) have similar zircon age / Hf-isotope characteristics to Phanerozoic cover sequences (RSH07a), which themselves may have been recycled from first-cycle Cambrian or Neoproterozoic sedimentary rocks derived from the mountain belt that crossed North Africa following the Pan-African orogeny (Meinhold et al., 2013).

All Oligocene to Pleistocene Nile delta fan samples analysed in this study have similar zircon age / Hf isotope characteristics to modern Nile trunk samples (Figure 6.3). They contain components that are ultimately derived from Arabian Nubian Shield sources (c.600-850 Ma grains), with some additional contribution from cratonic sources such as the Saharan Metacraton, or the Congo/Tanzania craton (>1500 Ma

grains). As with the modern Nile trunk samples, these age / Hf isotope distributions are similar to those seen in Phanerozoic cover sequences in the Red Sea Hills and Western Desert (Chapter 4), and in modern sediments eroded from these areas.  In the Red Sea Hills, wadis draining into the Nile from the western flank of the Red Sea Hills cut easily erodable Mesozoic sequences (e.g. the 'Nubian' Sandstone), whereas Arabian Nubian Shield basement rocks in the eastern Red Sea Hills mostly drain eastwards into the Red Sea.  For that reason, it is probable that many zircons in the delta cone samples are recycled through Phanerozoic cover and are not directly derived from their primary sources.

 >1500 Ma zircon grains are more common in Oligocene and Pliocene core samples, and are relatively sparse in Miocene and Pleistocene samples. We ascribe this to increased contribution from the Red Sea Hills at these times: the Red Sea Hills rocks contain an appreciable population of grains this age (sample RSH07a, Figure 6.3) and we observe an increase in this population between the Nile trunk sand sampled upstream (SD04) versus downstream (BS01) of the Red Sea Hills.  The larger proportion of Red Sea Hills detritus in the Nile during deposition of the 31 Ma Oligocene samples could be explained by the fact that the Red Sea Hills was uplifting at that time (e.g. (Bohannon et al., 1989; Ghebread, 1998; Kenea, 2001; Omar and Steckler, 1995) (Chapter 4).  The Pliocene samples were deposited at c. 2.65 Ma, which follows the Messinian Salinity Crisis (c.5.59-5.33 Ma (Krijgsman et al., 1999). We propose that the down-cutting of the Eonile canyon during the Messinian (Said, 1981) was followed by infilling with  locally derived sediment from the Red Sea Hills which led to an increase in the proportion of > 1500 Ma grains in the provenance

signature of the delta cone at this time. It is also possible that erosion of cover

sequences in the Ethiopian Highlands took place at this time.

The availability of > 1500 Ma grains in Phanerozoic sedimentary cover in similar

proportions to those seen in the delta samples means that it is not necessary to

invoke direct derivation of such grains from cratonic sources, such as the White Nile

source regions.  Furthermore, it is  thought that the White Nile was not connected to

the main Nile trunk until c.250 k.y. ago (Williams et al., 2003).

Cenozoic grains, derived from the Ethiopian Highlands (Chapter 5) occur in Nile cone

sediments from the Miocene (15.2 Ma) onwards.

Detrital U/Pb rutile analyses show complex age distributions, reflecting re-

equilibration of the rutile grains during Pan-African metamorphism.  However, the

lack of clear discriminating features in source samples from the Nile catchment

(Chapter 4) means that little useful provenance information can be derived from

these analyses.

### 6.4.2 Evidence from heavy mineral assemblages for diagenesis and hydraulic sorting.

Our analysis of heavy mineral assemblages shows that the composition of the Nile

delta samples is influenced by both mineral sorting and especially by burial

diagenesis (as seen by the progressive loss of less stable minerals down-hole, passing

to an ultra-stable assemblage at greatest depths).

Heavy mineral assemblages from both mud and sand samples from the Nile delta

cone were analysed to see if intrastratal dissolution had a lesser effect on less

permeable muds. However, heavy-mineral assemblages in Pleistocene and Pliocene sands and muds resulted to be very similar.

Chattian sands and muds and Rupelian sands and muds are also similar, except for a higher garnet/apatite and zircon/tourmaline ratio in the sands, which may be controlled by preferential hydraulic concentration of denser garnet and zircon in sands, and of less dense apatite and tourmaline in muds - "suspension sorting"; (Garzanti et al., 2011; Slingerland, 1984). Further evidence of suspension-sorting effects is the systematically greater relative abundance of zircon, rutile and garnet in sands than in muds of equivalent stratigraphic age. Also, monazite was sporadically observed in sands, but never recorded in muds.

### 6.4.3 The influence of provenance and hydraulic sorting on Sr, Nd and Hf isotope compositions.

Sr and Nd isotope distributions of both modern and Nile cone samples (Figure 6.5) show a broad trend of decreasing εNd and increasing $^{87}Sr/^{86}Sr$ downstream, from the Tekeze; Blue Nile; Nile trunk; Holocene Nile (onshore; Woodward et al 2015; and Miocene / Pleistocene delta; Oligocene / Pliocene delta. The correlation of these two isotope systems is well explained by changes in provenance, involving an Ethiopian basaltic source and a crustal end member.

Aeolian or White Nile sources have commonly been invoked as crustal end-members in studies of the more recent Nile sedimentary system involving Sr and Nd isotopes (Box et al., 2011; Krom et al., 1999; Krom et al., 2002; Padoan et al., 2011; Revel et al., 2014). Our Nile delta samples span 30 Ma of varying climate, through much of which the White Nile was not connected to the trunk Nile. An aeolian end-member would require a constantly arid environment since the Oligocene, which we know

not to be the case (Revel et al., 2010). We therefore consider locally derived sediment from Phanerozoic cover to be the most likely source of crustal material to the delta mud samples since 30 Ma. This is consistent with the evidence given above for derivation of zircons in Nile delta sands from Phanerozoic cover sequences, and conforms to the conclusion of Chapter 4, that the modern Nile trunk is dominated by detritus derived from erosion of Phanerozoic cover.

In detail, the Sr and Nd isotope data of delta mud samples show considerable scatter. Sr isotope data in particular (Figure 6.4 and 6.5) plot on a consistent trend for much of the last 30 Ma, towards a highly radiogenic end member composition that is not represented by any lithology or source sampled in the catchment area. Elevated $^{87}Sr/^{86}Sr$ values in muds may result from mineral sorting in the fluvial system or during deposition in the delta.

Hydraulic sorting within rivers can lead to elevated $^{87}Sr/^{86}Sr$ in suspended loads with little variation in Nd isotope composition (Garcon et al., 2014). Fluvial transportation in suspended loads enriched in phyllosilicates will result in increased $^{87}Sr/^{86}Sr$ in oceanic clays (Garcon et al., 2014).   In contrast, the Nd isotope budget of fluvial sediments is controlled by either monazite and allanite (eg. in Himalayan-derived sediments; Garzanti et al., 2010) or by titanite (as in the case of the Nile; Padoan et al., 2011 fig. 5), with additional contributions by clay minerals and biotite. Sm and Nd show little fractionation among these mineral phases, so there is little variation in Nd-isotope composition between bed-load and suspended-load.  The Hf-isotope budget of fluvial sediments is strongly controlled by detrital zircon.

Mineral sorting may also take place during deposition in the delta, with graded turbidites displaying a progressive decrease in the concentration of heavy minerals (e.g. zircon) from the base to the top, where clays with high Rb/Sr ratio are concentrated.

Jung et al. (2004) present Sr-Nd isotope data which illustrate the effect of weathering on dust derived from North Africa during the Holocene.  The dust fraction in Arabian Sea sediment cores spanning a time of changing climate was analysed, and results were interpreted as indicating changes in the weathering process in North Africa. The data have identical average εNd (-6) to average modern Red Sea Hills mud (Figure 6.5), but significantly elevated $^{87}Sr/^{86}Sr$.  Notably, <63 micron dust fractions have average $^{87}Sr/^{86}Sr$ of 0.712 – 0.714, whereas the <2 micron fractions have values of 0.714 – 0.717, suggesting that grain-size may also be an important factor in influencing $^{87}Sr/^{86}Sr$.

The most radiogenic Sr isotope values in our dataset are shown by Pliocene Nile cone muds.  In a single well (Figure 6.9), four Pliocene samples show $^{87}Sr/^{86}Sr$ increasing from 0.7073 to 0.7096 with depth, with two samples showing a reversal of the trend to a value of 0.7083.  This trend is mirrored by an inverse trend in Nd isotope composition.  This inverse-correlation of Sr and Nd isotope composition cannot be explained by weathering or mineral sorting processes, which should have little effect on Nd isotope composition.  We therefore conclude that the dominant control on the isotope characteristics of Nile muds is changing provenance.

As demonstrated in Chapter 5, modern Nile sediments plot on a simple trend in Nd-Sr isotope space between an Ethiopian basaltic end-member and modern Red Sea

Hill wadi muds. The trend towards highly radiogenic Sr values is only shown by delta muds. We therefore conclude that sorting of clays during turbidite deposition is responsible for the elevated values seen in many mud samples.

It is notable that Pliocene and Oligocene muds show lower average εNd and higher average $^{87}Sr/^{86}Sr$ than Miocene and Oligocene muds. This is consistent with the evidence presented above for a greater component of derived zircons from siliciclastic cover sequences in Oligocene and Pliocene samples.

Hf-Nd data for Nile cone muds show significant scatter (Figure 6.6). Despite this, individual groups of data points cluster (e.g. 31 Ma Oligocene, 27.5 Ma Oligocene and 2.65 Ma Pliocene). It is possible to construct mixing lines on this plot between Ethiopian basalts (Meshesha and Shinjo, 2010) and Red Sea Hills modern river sediments for different Nd/Hf concentration ratios. Pliocene samples, 17.0 Ma Miocene and 27.5 Ma Oligocene samples fit trends with very high Nd/Hf (dashed line - Figure 6.4). Modern Blue Nile and Nile trunk samples, Pleistocene, 15.2 Ma Miocene and 31 Ma Oligocene plot close to a trend with Nd/Hf = 5 (solid line – Figure 6.4). Variations in εNd and εHf values may be explained by the removal of Hf-rich zircon from suspended loads in the fluvial system, with higher Nd/Hf ratios reflecting higher degrees of sorting.

It is notable that the Pliocene samples which plot on trends indicating the highest Nd/Hf ratios (indicating the most extreme levels of zircon removal from the system) also show the highest $^{87}$Sr/$^{86}$Sr ratios, indicating concentration of clay minerals. This is consistent with the evidence from our heavy mineral analysis, which shows that the composition of the Nile delta samples is influenced by mineral sorting.
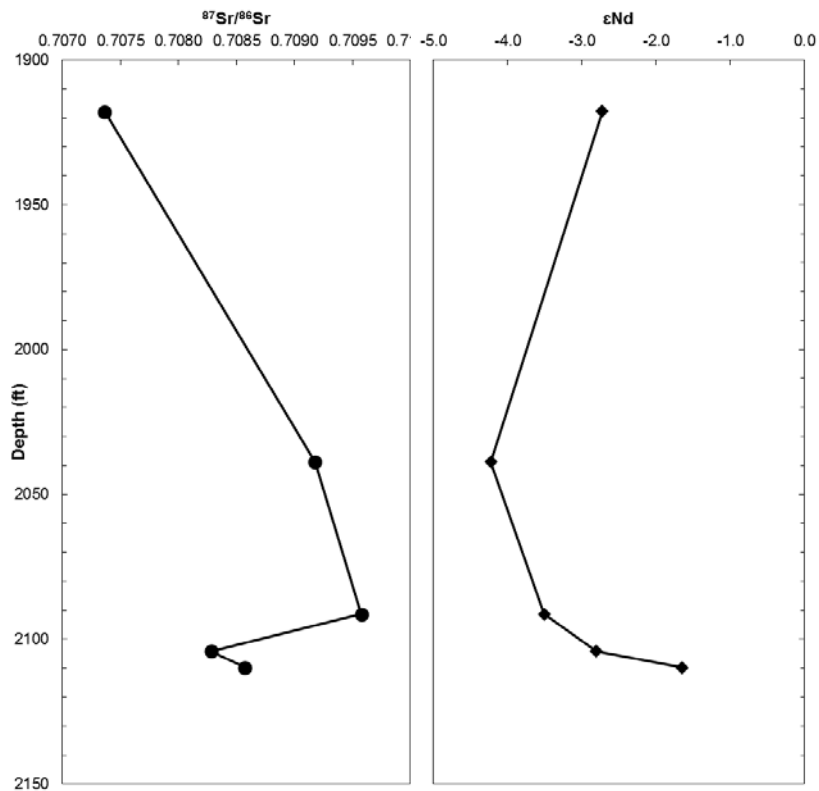


**Figure 6.9** $^{87}$Sr/$^{86}$Sr and εNd data for a single Pliocene well**. The inverse correlation of Sr and Nd isotopes suggests that controls such as provenance and grain size (mineral sorting) dominate the isotope signal – and not weathering or diagenesis.

## 6.5 Conclusions

All Oligocene to Pleistocene Nile cone samples analysed in this study have similar zircon age / Hf isotope characteristics to modern Nile trunk samples, indicating no major changes in palaeodrainage over time. The cone samples contain zircons that were ultimately derived from Arabian Nubian Shield sources (c.650-850 Ma grains), together with grains resulting from post-collisional intrusions (c. 600 Ma), with some additional contributions ultimately derived from cratonic sources such as the Saharan Metacraton, or the Congo/Tanzania Craton (>1500 Ma grains). The majority of these grains were recycled through Phanerozoic cover sequences before deposition in the cone. Nile cone sediments of at least Miocene age and younger additionally contain zircons derived from Ethiopian Highlands outlined in Chapter 5.

Craton-derived (> 1500 Ma) zircon grains are more common in Oligocene and Pliocene core samples, and are relatively sparse in Miocene and Pleistocene samples. The higher proportion of craton-aged grains in 31 Ma Oligocene samples could be explained by the Nile being dominated by locally eroded sediment from the Red Sea Hills, a proximal source which was up-lifting at that time. The higher proportion of craton-aged grains in the Pliocene samples could be the result of infilling of the Eonile Canyon by detritus from the Red Sea Hills after down-cutting following the Messinian Salinity Crisis.

The availability of > 1500 Ma grains in Phanerozoic sedimentary cover in similar proportions to those seen in the delta samples means that it is not necessary to invoke direct derivation of such grains from cratonic sources, such as the White Nile source regions.

Locally derived sediment from Phanerozoic cover, rather than aeolian dust, is the

most likely source of crustal material to the delta mud samples. This is consistent

with the evidence for derivation of zircons in Nile delta sands from Phanerozoic cover

sequences.

The dominant trend towards high $^{87}$Sr/$^{86}$Sr values in the Nile delta cone reflects

varying degrees of mineral sorting and concentration of clay minerals during

deposition. This also accounts for the variation of εNd and εHf values in the Nile cone

muds, because Hf-rich zircon is concentrated in sand.

**Chapter 7:** Concluding Discussion

This thesis addresses several questions regarding the provenance of the Nile delta cone sediments, but also addresses the evolution of the entire hinterland of the Nile River. Each chapter has addressed aspects of the geological evolution of the Nile cone sediments and source regions by generating a large multi-technique data-set in order to carry out a robust study.

## 7.1 A detrital record of Nile hinterland evolution (Chapter 4)

In this chapter addressing the Nile source regions, the results support the consensus that sediment recycling plays a huge role in the provenance signature of Phanerozoic sediments in North Africa. U-Pb-Hf data on detrital zircons from the White Nile, Blue Nile, Atbara/Tekeze and Nile trunk, as well as potential source regions in the Red Sea Hills and Western Desert sheds light on the evolution of the Arabian Nubian Shield and the final assembly of Gondwana. In doing so, previous debates about the depositional environment of the Hammamat formation have been addressed as it is found to have been deposited in an intra-arc setting, prior to the final assembly of Gondwana c.630 Ma.

Phanerozoic cover sediments which blanket much of North East Africa represent an important source of detritus to the river and are characterised by the presence of significant (9-12%) populations of pre-Neoproterozoic zircon grains and are found to be most common in modern Nile trunk sediments, making up 9%.

Geomorphic features are also shown to have a marked effect on the modern Nile catchment. The provenance signature of the White Nile is dramatically different upstream and downstream of the Sudd marshes as a result of sediment trapping. North of the Sudd, at Kosti, the signature of the White Nile is dominated by material

derived from Phanerozoic sandstones via alluvial fans to the west of the river.
Further north, to the south of Khartoum, the White Nile is greatly affected by its
proximity to the Gezira fan and receives an influx of Blue Nile sediment during times
of peak flow.

Other downstream changes include the decreasing abundance of Ethiopian volcanic
detritus in the Blue Nile and Atbara as more sediment is derived from Phanerozoic
cover and Arabian Nubian Shield basement downstream.

## 7.2 When did the Nile begin? (Chapter 5)

In Chapter 5, we show that the extensive Nile catchment that we see today was
established much earlier than previously suggested, and present evidence of detritus
from the Ethiopian large-igneous-province (LIP) reaching the cone since at least the
Oligocene (31 Ma).

Zircons with U/Pb ages and hafnium isotope signatures compatible with the
Ethiopian LIP were supplied to the delta since at least the Miocene (16 Ma). Such
zircons are absent from Oligocene cone sediments, but Nd and Sr isotope data for
Oligocene cone muds as old as 31 Ma require significant mafic input. The Ethiopian
LIP represents the only possible source for this detritus. Our findings have
implications for the nature of continental break-up during the Pan African orogeny,
and for sapropel development in the Mediterranean.

## 7.3 The evolution of the river Nile and factors affecting the Nile cone sedimentary record (Chapter 6)

All Oligocene to Pleistocene Nile cone samples analysed in Chapter 6 have similar zircon age / Hf isotope characteristics to modern Nile trunk samples. This indicates that no major changes to the palaeodrainage of the Nile have happened since c.31 Ma. The Nile cone samples contain zircons that were ultimately derived from Arabian Nubian Shield sources (c.600-850 Ma grains), with some additional contribution from cratonic sources such as the Saharan Metacraton, or the Congo/Tanzania craton (>1500 Ma grains). The majority of these grains were recycled through Phanerozoic cover sequences before deposition in the cone. Nile cone sediments of Miocene age and younger additionally contain zircons derived from Ethiopian Highlands outlined in Chapter 5.

Craton-derived (> 1500 Ma) zircon grains are more common in Oligocene and Pliocene core samples, and are relatively sparse in Miocene and Pleistocene samples. The higher proportion of craton-aged grains in 31 Ma Oligocene samples could be explained by the Nile being dominated by locally eroded sediment from the Red Sea Hills, a proximal source which was up-lifting at that time. The higher proportion of craton-aged grains in the Pliocene samples could be the result of infilling of the Eonile Canyon by detritus from the Red Sea Hills after down-cutting following the Messinian Salinity Crisis.

Locally derived sediment from Phanerozoic cover, rather than aeolian dust, is the most likely source of crustal material to the delta mud samples. This is consistent

with the evidence for derivation of zircons in Nile cone sands from Phanerozoic cover sequences.

The dominant trend towards high $^{87}Sr/^{86}Sr$ values in the Nile cone reflects varying degrees of mineral sorting and concentration of fine clay minerals during deposition in the delta. This also accounts for the variation of εNd and εHf values in the Nile cone muds where Hf-rich zircon is concentrated in sands as opposed to suspended loads as a result of mineral sorting during deposition and settling out of suspension.

**Chapter 8:** Limitations & Further Work

## 8.1 Limitations

This study acknowledges that the analysis conducted has limitations. Some of these limitations include:

**Sampling bias**: (grain size, heavy mineral separation, picking of zircon and rutile for single grain analysis etc.). Although every measure was taken to ensure that there was no sampling bias, it will always remain an issue. For example, it is not possible to analyse grains smaller than the diameter of the laser spot used for laser ablation during U/Pb zircon analysis. For this reason it is possible to 'miss' certain zircon populations and declare them as absent.

**Aeolian contamination:** Modern-river samples may have some degree of aeolian contamination. Avoiding this proved most difficult in the more arid source areas such as the Western Desert and Red Sea Hills where water-laid sediments were sometimes unavailable. In these circumstances, samples were taken as close to the head of the wadi as possible where it was more sheltered. From analysing both modern wadi sediments and bedrock samples from these areas, it is clear to see that the modern wadi sands have a very similar detrital zircon signature to the underlying bedrock and therefore aeolian contamination is negligible. This was not the case for the petrographical analysis, which showed all Nile River sediments to have a signature more characteristic of Saharan Dune samples.

Availability of core samples: Large gaps of time between Chattian – Burdigalian, Langhian – Upper Pliocene and the Upper Pliocene – Upper Pleistocene core samples meant that it was difficult to pinpoint the exact timing of changes in provenance.

**Characterisation of source regions:** This study has focused on regions currently and previously thought to have been drained by the Nile. This does not necessarily encompass all possible sediment sources to the Nile Cone.

## 8.2 Further Work

This project has produced an extensive sample-set of modern river and wadi sediments and bedrock samples from across the Nile catchment, together with samples from the Nile Cone spanning the last 30 Ma.  There is much potential for future research using these samples. In particular, more than 40 heavy mineral separates are available for future study.

Possible future research might include study of detrital apatite or monazite, and some exploratory work has already taken place at NIGL.

Apatite is of interest because it is a much more brittle mineral than zircon, so much less likely to survive multiple cycles of erosion, and more likely to represent first-generation erosion and deposition.  Apatite is difficult to date precisely using U-Pb because of high common Pb contents.  However, it is rich in rare-earth elements, including Nd, and laser-ablation analysis of Nd has been shown to be of use in provenance studies (Henderson et al., 2010).

Preliminary laser-ablation Sm-Nd analysis of Nile sediments shows linear correlations that, if interpreted as isochrons, appear to show real age information.  Figure 8.1a shows apatite laser-ablation Sm-Nd data for sample ETH2a, from the Ethiopian Blue Nile.  The detrital zircon population of this is dominated by peaks indicating ages of 675 and 810 Ma. Cenozoic grains are also common in this sample.

The apatite data form three populations.  Two populations form linear arrays which suggest ages of c. 688 and 835 Ma, similar to the age populations seen in the zircon data.  A third population shows little spread in age, and has relatively high $^{143}Nd/^{144}Nd$, suggesting that these may be Cenozoic grains, although they plot close to juvenile grains from the Nile Cone, which plot on a c. 1000 Ma isochron (Figure 8.1b).

Also shown in Figure 8.1a are apatite grains from the White Nile at Murchison Falls in Uganda.  These show a broad scatter, with lower, more crust-dominated $^{143}Nd/^{144}Nd$ ratios than ETH2a.  Two samples from the Nile Cone were also studied.  Samples ND10 and ND41 are dominated by a 600 Ma zircon peak, with subordinate peaks extending back to 1000 Ma, and sparse Palaeoproterozoic and Archaean grains.  Apatite data show two dominant trends, indicating ages of c. 600 and 1032 Ma, again consistent with the detrital zircon age distribution.

Uncertainties are large at the moment, but by combining with U-Pb apatite dating, there is potential to get more information on the geology of source regions, and place constraints on the extent of recycling.

The results of detrital rutile analysis during this project were disappointing, as no age populations were identified that gave distinctive provenance information.  The same may be true of monazite, which is likely to reflect Pan-African events.  However, monazite inclusions armoured within garnet may survive metamorphic overprinting, and record earlier metamorphic events, that might be diagnostic of specific source terranes.

In Chapter 6, the role of grain size control on the isotope composition of fine-grained mud samples is discussed.  The relationship between clay mineralogy, grain size and isotope composition has not been explored in detail during this study.  Further study might shed

light on the mixing processes between end-members highlighted by the tracer isotope analyses presented here.
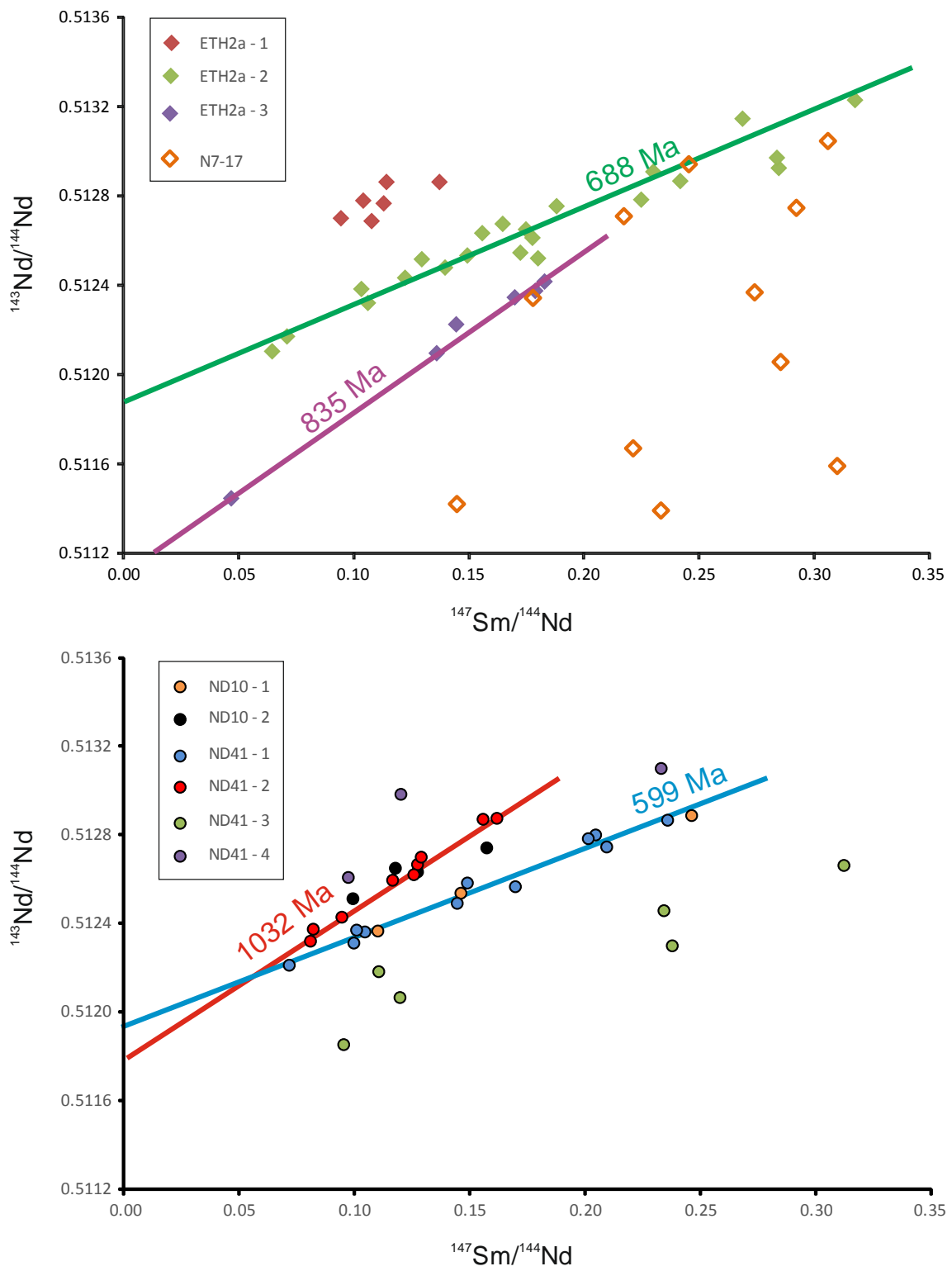


**Figure 8.1a** (top) **and b** (bottom) Preliminary Sm-Nd data for detrital apatites.

# 9.0 References

Abd-El-Rahman, Y., Polat, A., Fryer, B.J., Dilek, Y. & El-Sharkawy, M. , 2010, The provenance and textonic setting of the Neoproterozoic Um Hassa Greywacke Member, Wadi Hammamat area, Egypt: Evidence from petrography and geochemistry: Journal of African Earth Sciences, v. 58, p. 11.

Abdelkareem, M., and El-Baz, F., 2015, Mode of formation of the Nile Gorge in northern Egypt: a study by DEM-SRTM data and GIS analysis: Geological Journal.

Abdelsalam, M. G., Gao, S. S., and Liégeois, J.-P., 2011, Upper mantle structure of the Saharan Metacraton: Journal of African earth sciences, v. 60, no. 5, p. 328-336.

Abdelsalam, M. G., Li, J.P., Stern, R.J., 2002, Review: The Saharan Metacraton: Journal of African Earth Sciences, v. 34, p. 119-136.

Abdelsalam, M. G., Liégeois, J.-P., and Stern, R. J., 2002, The saharan metacraton: Journal of African Earth Sciences, v. 34, no. 3, p. 119-136.

Adamson, D., and WIlliams, F., 1980, Structural geology, tectonics and the control of drainage in the Nile Basin, 10: Rotterdam, p. 325-340.

Adamson, D. A., Gasse, F., Street, F., and Williams, M., 1980, Late Quaternary history of the Nile: Nature, v. 288, p. 50-55.

al-Miṣrīyah, H., 1981, Geologic map of Egypt Ministry of Industry and Mineral Resources, The Egyptian Geological Survey and Mining Authority.

Ali, B. H., Wilde, S. A., and Gabr, M. M. A., 2009, Granitoid evolution in Sinai, Egypt, based on precise SHRIMP U–Pb zircon geochronology: Gondwana Research, v. 15, no. 1, p. 38-48.

Ali, K. A., Azer, M. K., Gahlan, H. A., Wilde, S. A., Samuel, M. D., and Stern, R. J., 2010, Age constraints on the formation and emplacement of Neoproterozoic ophiolites along the Allaqi-Heiani Suture, South Eastern Desert of Egypt: Gondwana Research, v. 18, no. 4, p. 583-595.

Altumi, M. M., Elicki, O., Linnemann, U., Hofmann, M., Sagawe, A., and Gärtner, A., 2013, U–Pb LA-ICP-MS detrital zircon ages from the Cambrian of Al Qarqaf Arch, central-western Libya: Provenance of the West Gondwanan sand sea at the dawn of the early Palaeozoic: Journal of African Earth Sciences, v. 79, p. 74-97.

Andò, S., Garzanti, E., Padoan, M., and Limonta, M., 2012, Corrosion of heavy minerals during weathering and diagenesis: A catalog for optical analysis: Sedimentary Geology, v. 280, p. 165-178.

Andresen, A., Abu El-Enen, M.M., Stern, R.J., Wilde, S.A., Ali, K.A., 2014, The Wadi Zaghra metasediments of Sinai, Egypt: new constraints on the late Cryogenian-Ediacaran tectonic evolution of the northernmost Arabian-Nubian Shield: International Geology Review, v. 56, no. 8, p. 18.

Appel, P., Schenk, V., and Schumann, A., 2005, PT path and metamorphic ages of pelitic schists at Murchison Falls, NW Uganda Evidence for a Pan-African tectonometamorphic event in the Congo Craton: European journal of mineralogy, v. 17, no. 5, p. 655-664.

Avigad, D., Gerdes, A., Morag, N., and Bechstädt, T., 2012, Coupled U–Pb–Hf of detrital zircons of Cambrian sandstones from Morocco and Sardinia: Implications for provenance and Precambrian crustal evolution of North Africa: Gondwana Research, v. 21, no. 2-3, p. 690-703.

Avigad, D., Kolodner, K., McWilliams, M., Persing, H., and Weissbrod, T., 2003, Origin of

    northern Gondwana Cambrian sandstone revealed by detrital zircon SHRIMP dating:

    Geology, v. 31, no. 3, p. 227.

Baker, J., Thirlwall, M., and Menzies, M., 1996, Sr☐ Nd☐ Pb isotopic and trace element

    evidence for crustal contamination of plume-derived flood basalts: Oligocene flood

    volcanism in western Yemen: Geochimica et Cosmochimica Acta, v. 60, no. 14, p.

    2559-2581.

Be'eri-Shlevin, Y., Katzir, Y., and Valley, J. W., 2009, Crustal evolution and recycling in a

    juvenile continent: Oxygen isotope ratio of zircon in the northern Arabian Nubian

    Shield: Lithos, v. 107, no. 3-4, p. 169-184.

Bea, F., Montero, P., Anbar, M. A., and Talavera, C., 2011, SHRIMP dating and Nd isotope

    geology of the Archean terranes of the Uweinat-Kamil inlier, Egypt–Sudan–Libya:

    Precambrian Research, v. 189, no. 3, p. 328-346.

Beckinsale., R. D., Gale., N.H., 1969, A reappraisal of the decay constants and branching ratio

    of 40K: Earth Planet Sci Lett, v. 6, p. 5.

Bellaiche, G., Loncke, L., Gaullier, V., Mascle, J., Courp, T., Moreau, A., Radan, S., and Sardou,

    O., 2001, Le cône sous-marin du Nil et son réseau de chenaux profonds: nouveaux

    résultats (campagne Fanil): Comptes Rendus de l'Académie des Sciences-Series IIA-

    Earth and Planetary Science, v. 333, no. 7, p. 399-404.

Beyth, M., Avigad, D., Wetzel, H. U., Matthews, A., and Berhe, S. M., 2003, Crustal

    exhumation and indications for Snowball Earth in the East African Orogen: north

    Ethiopia and east Eritrea: Precambrian Research, v. 123, no. 2–4, p. 187-201.

Bezenjani, N. R., Pease, V., Whitehouse, M. J., Shalaby, M. H., Kadi, K. A., and Kozdroj, W.,

    2014, Detrital zircon geochronology and provenance of the Neoproterozoic

Hammamat Group (Igla Basin), Egypt and the Thalbah Group, NW Saudi Arabia: Implications for regional collision tectonics: Precambrian Research, v. 245, p. 225-243.

Bohannon, R. G., Naeser, C. W., Schmidt, D. L., and Zimmermann, R. A., 1989, The timing of uplift, volcanism, and rifting peripheral to the Red Sea: a case for passive rifting?: Journal of Geophysical Research: Solid Earth (1978–2012), v. 94, no. B2, p. 1683-1701.

Bosworth, W., Huchon, P., and McClay, K., 2005, The Red Sea and Gulf of Aden Basins: Journal of African Earth Sciences, v. 43, no. 1-3, p. 334-378.

Botev, Z. I., Grotowski, J.F. & Kroese, D.P. , 2010, Kernal Density Estimation via Diffusion: The Annals of Statistics, v. 38, no. 5, p. 41.

Bouvier, A., Vervoort, J. D., and Patchett, P. J., 2008, The Lu–Hf and Sm–Nd isotopic composition of CHUR: constraints from unequilibrated chondrites and implications for the bulk composition of terrestrial planets: Earth and Planetary Science Letters, v. 273, no. 1, p. 48-57.

Box, M. R., Krom, M. D., Cliff, R. A., Bar-Matthews, M., Almogi-Labin, A., Ayalon, A., and Paterne, M., 2011, Response of the Nile and its catchment to millennial-scale climatic change since the LGM from Sr isotopes and major elements of East Mediterranean sediments: Quaternary Science Reviews, v. 30, no. 3-4, p. 431-442.

Bracciali, L., Najman, Y., Parrish, R. R., Akhter, S. H., and Millar, I., 2015, The Brahmaputra tale of tectonics and erosion: Early Miocene river capture in the Eastern Himalaya: Earth and Planetary Science Letters, v. 415, p. 25-37.

Bracciali, L., Parrish, R. R., Horstwood, M. S., Condon, D. J., and Najman, Y., 2013, UPb LA-(MC)-ICP-MS dating of rutile: New reference materials and applications to sedimentary provenance: Chemical Geology, v. 347, p. 82-101.

Breitkreuz, C., Eliwa, H., Khalaf, I., Gameel, K. E., Bühler, B., Sergeev, S., Larionov, A., and Murata, M., 2010, Neoproterozoic SHRIMP U–Pb zircon ages of silica-rich Dokhan Volcanics in the North Eastern Desert, Egypt: Precambrian Research, v. 182, no. 3, p. 163-174.

Buck, W., 2006, The role of magma in the development of the Afro-Arabian Rift System: Geological Society, London, Special Publications, v. 259, no. 1, p. 43-54.

Burke, K., and Wells, G. L., 1989, TRANS-AFRICAN DRAINAGE SYSTEM OF THE SAHARA - WAS IT THE NILE: Geology, v. 17, no. 8, p. 743-747.

Cahen, L., Snelling, N. J., Delhal, J. v., and Vail, J. R., 1984, The Geochronology and Evolution of Africa, Oxford, Clarendon, 581 p.:

Cox, K. G., 1989, The role of mantle plumes in the development of continental drainage patterns.: Nature, v. 342, p. 4.

Craig, T., Jackson, J., Priestley, K., and McKenzie, D., 2011, Earthquake distribution patterns in Africa: their relationship to variations in lithospheric and geological structure, and their rheological implications: Geophysical Journal International, v. 185, no. 1, p. 403-434.

Daumain, G., Dubertret, L., and Lelubre, M., 1958, Esquisse Structurale Provisoire de l'Afrique: Association des Services Geologiques Africains (ASGA) Congrès Géologique International.

De Waele, B., Johnson, S., and Pisarevsky, S., 2008, Palaeoproterozoic to Neoproterozoic

growth and evolution of the eastern Congo Craton: its role in the Rodinia puzzle:

Precambrian Research, v. 160, no. 1, p. 127-141.

Dolson, J. C., Shann, M. V., Matbouly, S., Harwood, C., Rashed, R., and Hammouda, H., 2001,

AAPG Memoir 74, Chapter 23: The Petroleum Potential of Egypt.

Ebinger, C., 2005, Continental break-up: the East African perspective: Astronomy &

Geophysics, v. 46, no. 2, p. 2.16-12.21.

El Diasty, W. S., and Moldowan, J. M., 2013, The Western Desert versus Nile Delta: A

comparative molecular biomarker study: Marine and Petroleum Geology, v. 46, no.

0, p. 319-334.

Eliwa, H., Breitkreuz, C., Khalaf, I., and Gameel, K. E., 2010, Depositional styles of Early

Ediacaran terrestrial volcanosedimentary succession in Gebel El Urf area, North

Eastern Desert, Egypt: Journal of African Earth Sciences, v. 57, no. 4, p. 328-344.

Evuk, D., Franz, G., Frei, D., and Lucassen, F., 2014, The Neoproterozoic evolution of the

central-eastern Bayuda Desert (Sudan): Precambrian Research, v. 240, no. 0, p. 108-

125.

Flowerdew, M., Millar, I., Vaughan, A., Horstwood, M., and Fanning, C., 2006, The source of

granitic gneisses and migmatites in the Antarctic Peninsula: a combined U–Pb

SHRIMP and laser ablation Hf isotope study of complex zircons: Contributions to

Mineralogy and Petrology, v. 151, no. 6, p. 751-768.

Foucault, A., and Stanley, D. J., 1989, LATE QUATERNARY PALEOCLIMATIC OSCILLATIONS IN

EAST-AFRICA RECORDED BY HEAVY MINERALS IN THE NILE DELTA: Nature, v. 339, no.

6219, p. 44-46.

Galehouse, J. S., 1971, Point counting: Procedures in sedimentary petrology, p. 385-407.

Gani, N. D., Abdelsalam, M. G., Gera, S., and Gani, M. R., 2009, Stratigraphic and structural

evolution of the Blue Nile Basin, Northwestern Ethiopian Plateau: Geological Journal,

v. 44, no. 1, p. 30-56.

Gani, N. D. S., Gani, M. R., and Abdelsalam, M. G., 2007, Blue Nile incision on the Ethiopian

Plateau: Pulsed plateau growth, Pliocene uplift, and hominin evolution: GSA Today,

v. 17, no. 9, p. 4.

Garcon, M., Chauvel, C., France-Lanord, C., Limonta, M., and Garzanti, E., 2014, Which

minerals control the Nd–Hf–Sr–Pb isotopic compositions of river sediments?:

Chemical Geology, v. 364, p. 42-55.

Garzanti, E., and Andò, S., 2007, Heavy mineral concentration in modern sands: implications

for provenance interpretation: Developments in Sedimentology, v. 58, p. 517-545.

Garzanti, E., Andó, S., France-Lanord, C., Censi, P., Vignola, P., Galy, V., and Lupker, M.,

2011, Mineralogical and chemical variability of fluvial sediments 2. Suspended-load

silt (Ganga–Brahmaputra, Bangladesh): Earth and Planetary Science Letters, v. 302,

no. 1, p. 107-120.

Garzanti, E., Andò, S., Padoan, M., Vezzoli, G., and El Kammar, A., 2015, The modern Nile

sediment system: Processes and products: Quaternary Science Reviews, v. 130, p. 9-

56.

Garzanti, E., Andò, S., Vezzoli, G., Ali Abdel Megid, A., and El Kammar, A., 2006, Petrology of

Nile River sands (Ethiopia and Sudan): Sediment budgets and erosion patterns: Earth

and Planetary Science Letters, v. 252, no. 3-4, p. 327-341.

Garzanti, E., and Vezzoli, G., 2003, A classification of metamorphic grains in sands based on

their composition and grade: Research Methods Papers: Journal of Sedimentary

Research, v. 73, no. 5, p. 830-837.

Ghebread, 1998, Tectonics of the Red Sea region assesed: Earth Science Review, v. 45, p. 1-
44.

Goodwin, A. M., 1996, Principles of Precambrian geology, Academic Press.

Greiling, R., de Wall, H., Sadek, M., and Dietl, C., 2014, Late Pan-African granite
emplacement during regional deformation, evidence from magnetic fabric and
structural studies in the Hammamat–Atalla area, Central Eastern Desert of Egypt:
Journal of African Earth Sciences.

Henderson, A. L., Foster, G. L., and Najman, Y., 2010, Testing the application of in situ Sm–
Nd isotopic analysis on detrital apatites: A provenance tool for constraining the
timing of India–Eurasia collision: Earth and Planetary Science Letters, v. 297, no. 1, p.
42-49.

Hofmann, C., Courtillot, V., Feraud, G., Rochette, P., Yirgu, G., Ketefo, E., and Pik, R., 1997,
Timing of the Ethiopian flood basalt event and implications for plume birth and
global change: Nature, v. 389, no. 6653, p. 838-841.

Horstwood, M., 2008, Data reduction strategies, uncertainty assessment and resolution of
LA-(MC-) ICP-MD isotope data, Mineralogical Association of Canada, v. 40.

Horstwood, M. S., Foster, G. L., Parrish, R. R., Noble, S. R., and Nowell, G. M., 2003,
Common-Pb corrected in situ U–Pb accessory mineral geochronology by LA-MC-ICP-
MS: Journal of Analytical Atomic Spectrometry, v. 18, no. 8, p. 837-846.

Hubert, J. F., 1962, A zircon-tourmaline-rutile maturity index and the interdependence of
the composition of heavy mineral assemblages with the gross composition and
texture of sandstones: Journal of Sedimentary Research, v. 32, no. 3.

Iizuka, T., Campbell, I. H., Allen, C. M., Gill, J. B., Maruyama, S., and Makoka, F., 2013,
Evolution of the African continental crust as recorded by U-Pb, Lu-Hf and O isotopes

in detrital zircons from modern rivers: Geochimica Et Cosmochimica Acta, v. 107, p. 96-120.

Ingersoll, R. V., Fullard, T. F., Ford, R. L., Grimm, J. P., Pickle, J. D., and Sares, S. W., 1984, The effect of grain size on detrital modes; a test of the Gazzi-Dickinson point-counting method: Journal of Sedimentary Research, v. 54, no. 1, p. 103-116.

Issawi, B., and McCauley, J. F., 1992, The Cenozoic rivers of Egypt, the Nile problem., *in* Adams, B. a. F., R., ed., The Followers of Horus, studies dedicated to Michael Allen Hoffman 1944-1990., Volume 2: Oxford, Oxbow Press.

Issawi, B., and Osman, R., 2008, Egypt during the Cenozoic: geological history of the Nile River: Bulletin of the Tethys Geological Society, v. 3, p. 43-62.

Johnson, P. R., 2014, An Expanding Arabian-Nubian Shield Geochronologic and Isotopic Dataset: Defining Limits and Confirming the Tectonic Setting of a Neoproterozoic Accretionary Orogen: Open Geology Journal, v. 8, no. 1, p. 3-33.

Johnson, P. R., Andresen, A., Collins, A. S., Fowler, A. R., Fritz, H., Ghebreab, W., Kusky, T., and Stern, R. J., 2011a, Late Cryogenian-Ediacaran history of the Arabian-Nubian Shield: A review of depositional, plutonic, structural, and tectonic events in the closing stages of the northern East African Orogen: Journal of African Earth Sciences, v. 61, no. 3, p. 167-232.

-, 2011b, Late Cryogenian–Ediacaran history of the Arabian–Nubian Shield: A review of depositional, plutonic, structural, and tectonic events in the closing stages of the northern East African Orogen: Journal of African Earth Sciences, v. 61, no. 3, p. 167-232.

Johnson, P. R., and Woldehaimanot, B., 2003, Development of the Arabian-Nubian Shield: perspectives on accretion and deformation in the northern East African Orogen and

the assembly of Gondwana: Geological Society, London, Special Publications, v. 206, no. 1, p. 289-325.

Jung, S. J. A., Davies, G. R., Ganssen, G. M., and Kroon, D., 2004, Stepwise Holocene aridification in NE Africa deduced from dust-borne radiogenic isotope records: Earth and Planetary Science Letters, v. 221, no. 1-4, p. 27-37.

Karami, M., Meijer, P. T., Dijkstra, H., and Wortel, M., 2009, An oceanic box model of the Miocene Mediterranean Sea with emphasis on the effects of closure of the eastern gateway: Paleoceanography, v. 24, no. 4.

Katumwehe, A. B., Abdelsalam, M. G., Atekwana, E. A., and Laó-Dávila, D. A., 2015, Extent, kinematics and tectonic origin of the Precambrian Aswa Shear Zone in eastern Africa: Gondwana Research.

Kazmin, V., 1972, Geological map of Ethiopia.: Geological Survey of Ethiopia, Ministry of Mines, Energy and Water Resources.

Kenea, N. H., Ebinger, C.J., and Rex, D.C., 2001, Late Oligocene volcanism and extension in the southern Red Sea Hills, Sudan: Journal of the Geological Society, London, v. 158, p. 285-294.

Kidd, R. B., Cita, M. B., and Ryan, W. B. F., 1978, Stratigraphy of Eastern Mediterranean sapropel sequences recovered during DSDP 42A and paleoenvironmental significance: Init. Rep. DSDP, , v. 42, no. 1, p. 22.

Klitzsch, E. H., and Squyres, C. H., 1990, Paleozoic and Mesozoic Geological History of North Eastern Africa based upon new interpretation of Nubian strata: AAPG Bulletin, v. 74, no. 8, p. 8.

Kolodner, K., Avigad, D., Ireland, T. R., and Garfunkel, Z., 2009, Origin of Lower Cretaceous ('Nubian') sandstones of North-east Africa and Arabia from detrital zircon U-Pb SHRIMP dating: Sedimentology, v. 56, no. 7, p. 2010-2023.

Kolodner, K., Avigad, D., McWilliams, M., Wooden, J., Weissbrod, T., and Feinstein, S., 2006a, Provenance of north Gondwana Cambrian–Ordovician sandstone: U–Pb SHRIMP dating of detrital zircons from Israel and Jordan: Geological Magazine, v. 143, no. 03, p. 367-391.

Kolodner, K., Avigad, D., McWilliams, M., Wooden, J. L., Weissbrod, T., and Feinstein, S., 2006b, Provenance of north Gondwana Cambrian–Ordovician sandstone: U–Pb SHRIMP dating of detrital zircons from Israel and Jordan: Geological Magazine, v. 143, no. 03, p. 367-391.

Krijgsman, W., Hilgen, F., Raffi, I., Sierro, F., and Wilson, D., 1999, Chronology, causes and progression of the Messinian salinity crisis: Nature, v. 400, no. 6745, p. 652-655.

Krom, M., Cliff, R., Eijsink, L., Herut, B., and Chester, R., 1999, The characterisation of Saharan dusts and Nile particulate matter in surface sediments from the Levantine basin using Sr isotopes: Marine Geology, v. 155, no. 3, p. 319-330.

Krom, M. D., Stanley, J. D., Cliff, R. A., and Woodward, J. C., 2002, Nile River sediment fluctuations over the past 7000 yr and their key role in sapropel development: Geology, v. 30, no. 1, p. 71-74.

Kröner, A., and Stern, R., 2004, Africa: Pan-African orogeny: Encyclopedia of Geology. Elsevier, p. 1-12.

Kusky, T. M., and Matsah, M. I., 2003, Neoproterozoic dextral faulting on the Najd fault system, Saudi Arabia, preceded sinistral faulting and escape tectonics related to

closure of the Mozambique Ocean: Geological Society, London, Special Publications, v. 206, no. 1, p. 327-361.

Lapen, T. J., Mahlen, N. J., Johnson, C. M., and Beard, B. L., 2004, High precision Lu and Hf isotope analyses of both spiked and unspiked samples: a new approach: Geochemistry, Geophysics, Geosystems, v. 5, no. 1.

Loncke, L., Gaullier, V., Mascle, J., Vendeville, B., and Camera, L., 2006, The Nile deep-sea fan: An example of interacting sedimentation, salt tectonics, and inherited subsalt paleotopographic features: Marine and Petroleum Geology, v. 23, no. 3, p. 297-315.

Lucassen, F., Franz, G., Romer, R. L., Pudlo, D., and Dulski, P., 2008, Nd, Pb, and Sr isotope composition of Late Mesozoic to Quaternary intra-plate magmatism in NE-Africa (Sudan, Egypt): high-μ signatures from the mantle lithosphere: Contributions to Mineralogy and Petrology, v. 156, no. 6, p. 765-784.

Ludwig, K. R., 2003, User's manual for Isoplot 3.00: a geochronological toolkit for Microsoft Excel, Kenneth R. Ludwig, v. 4.

Macgregor, D. S., 2012, The development of the nile drainage system: integration of onshore and offshore evidence: Petroleum Geoscience, v. 18, no. 4, p. 417-431.

Mange, M. A., and Maurer, H. F., 1992, Heavy minerals in colourChapman and Hall, London.

Mark, D., Barfod, D., Stuart, F., and Imlach, J., 2009, The ARGUS multicollector noble gas mass spectrometer: Performance for 40Ar/39Ar geochronology: Geochemistry, Geophysics, Geosystems, v. 10, no. 10.

Mccauley, J. F., Breed, C. S., Schaber, G. G., McHugh, W. P., Issawi, B., Haynes, C. V., Grolier, M. J., and Kilani, A., 1986, Paleodrainages of the Eastern Sahara-The Radar Rivers Revisited (SIR-A/B Implications for a Mid-Tertiary Trans-Afnrcan Drainage System): Geoscience and Remote Sensing, IEEE Transactions on, no. 4, p. 624-648.

McLennan, S., and Taylor, S., 1985, The Continental Crust: Its Composition and Evolution: An

   Examination of the Geochemical Record Preserved in Sedimentary Rocks, Oxford:

   Blackwell Scientific.

Meijer, P. T., and Tuenter, E., 2007, The effect of precession-induced changes in the

   Mediterranean freshwater budget on circulation at shallow and intermediate depth:

   Journal of Marine Systems, v. 68, no. 3, p. 349-365.

Meinhold, G., Morton, A. C., and Avigad, D., 2013, New insights into peri-Gondwana

   paleogeography and the Gondwana super-fan system from detrital zircon U–Pb ages:

   Gondwana Research, v. 23, no. 2, p. 661-665.

Meinhold, G., Morton, A. C., Fanning, C. M., Frei, D., Howard, J. P., Phillips, R. J., Strogen, D.,

   and Whitham, A. G., 2011, Evidence from detrital zircons for recycling of

   Mesoproterozoic and Neoproterozoic crust recorded in Paleozoic and Mesozoic

   sandstones of southern Libya: Earth and Planetary Science Letters, v. 312, no. 1, p.

   164-175.

Meshesha, D., and Shinjo, R., 2010, Hafnium isotope variations in Bure volcanic rocks from

   the northwestern Ethiopian volcanic province: a new insight for mantle source

   diversity: Journal of mineralogical and petrological sciences, v. 105, no. 3, p. 101-111.

Miller, K. G., Sugarman, P. J., Browning, J. V., Kominz, M. A., Hernández, J. C., Olsson, R. K.,

   Wright, J. D., Feigenson, M. D., and Van Sickel, W., 2003a, Late Cretaceous

   chronology of large, rapid sea-level changes: Glacioeustasy during the greenhouse

   world: Geology, v. 31, no. 7, p. 585-588.

Miller, N. R., Alene, M., Sacchi, R., Stern, R. J., Conti, A., Kröner, A., and Zuppi, G., 2003b,

   Significance of the Tambien Group (Tigrai, N. Ethiopia) for Snowball Earth events in

   the Arabian–Nubian Shield: Precambrian Research, v. 121, no. 3–4, p. 263-283.

Ministry of Energy and Mines, S., 1981, Geological Map of the Sudan: Geological and

    Mineral Resources Department, Khartoum, Sudan.

Mock, C., Arnaud, N. O., Cantagrel, J.-M., and Yirgu, G., 1999, 40 Ar/39 Ar thermochronology

    of the Ethiopian and Yemeni basements: reheating related to the Afar plume?:

    Tectonophysics, v. 314, no. 4, p. 351-372.

Mohr, P., and Zanettin, B., 1988, The Ethiopian flood basalt province, Continental flood

    basalts, Springer, p. 63-110.

Morag, N., Avigad, D., Gerdes, A., Belousova, E., and Harlavan, Y., 2011, Detrital zircon Hf

    isotopic composition indicates long-distance transport of North Gondwana

    Cambrian–Ordovician sandstones: Geology, v. 39, no. 10, p. 955-958.

Moucha, R., and Forte, A. M., 2011, Changes in African topography driven by mantle

    convection: Nature Geoscience, v. 4, no. 10, p. 707-712.

Mourik, A., Bijkerk, J., Cascella, A., Hüsing, S., Hilgen, F., Lourens, L., and Turco, E., 2010,

    Astronomical tuning of the La Vedova High Cliff Section (Ancona, Italy)—Implications

    of the middle Miocene climate transition for Mediterranean sapropel formation:

    Earth and Planetary Science Letters, v. 297, no. 1, p. 249-261.

Münker, C., Weyer, S., Scherer, E., and Mezger, K., 2001, Separation of high field strength

    elements (Nb, Ta, Zr, Hf) and Lu from rock samples for MC-ICPMS measurements:

    Geochemistry, Geophysics, Geosystems, v. 2, no. 12.

Nelson, W. R., Furman, T., van Keken, P. E., Shirey, S. B., and Hanan, B. B., 2012, Os Hf

    isotopic insight into mantle plume dynamics beneath the East African Rift System:

    Chemical Geology, v. 320, p. 66-79.

Nowell, G., and Parrish, R., 2001, Simultaneous acquisition of isotope compositions and

    parent/daughter ratios by non-isotope dilution solution-mode plasma ionisation

multi-collector mass spectrometry (PIMMS): Special Publication of the Royal Society of Chemistry, v. 267, p. 298-310.

Omar, G. I., and Steckler, M. S., 1995, Fission track evidence on the initial rifting of the Red Sea: two pulses, no propagation: Science, v. 270, no. 5240, p. 1341-1344.

Padoan, M., Garzanti, E., Harlavan, Y., and Villa, I. M., 2011, Tracing Nile sediment sources by Sr and Nd isotope signatures (Uganda, Ethiopia, Sudan): Geochimica Et Cosmochimica Acta, v. 75, no. 12, p. 3627-3644.

Palacios, Z. H., 2013, Climate change as a controlling parameter in sediment supply : the Nile Province - See more at:

http://ethos.bl.uk/OrderDetails.do?uin=uk.bl.ethos.575393#sthash.0i0YHMsQ.dpuf

[PhD: University of Aberdeen

Paul, J. D., Roberts, G. G., and White, N., 2014, The African landscape through space and time: Tectonics.

Pickford, M., and Mein, P., 2006, Early Middle Miocene mammals from Moroto II, Uganda: Beiträge der Paläontologie, v. 30, p. 361-386.

Pik, R., Deniel, C., Coulon, C., Yirgu, G., Hofmann, C., and Ayalew, D., 1998, The northwestern Ethiopian Plateau flood basalts: classification and spatial distribution of magma types: Journal of Volcanology and Geothermal Research, v. 81, no. 1, p. 91-111.

Pik, R., Deniel, C., Coulon, C., Yirgu, G., and Marty, B., 1999, Isotopic and trace element signatures of Ethiopian flood basalts: evidence for plume–lithosphere interactions: Geochimica et Cosmochimica Acta, v. 63, no. 15, p. 2263-2279.

Pik, R., Marty, B., Carignan, J., and Lavé, J., 2003, Stability of the Upper Nile drainage network (Ethiopia) deduced from (U–Th)/He thermochronometry: implications for

uplift and erosion of the Afar plume dome: Earth and Planetary Science Letters, v. 215, no. 1-2, p. 73-88.

Pik, R., Marty, B., Carignan, J., Yirgu, G., and Ayalew, T., 2008, Timing of East African Rift development in southern Ethiopia: Implication for mantle plume activity and evolution of topography: Geology, v. 36, no. 2, p. 167.

Renne, P. R., Balco, G., Ludwig, K. R., Mundil, R., and Min, K., 2011, Response to the comment by WH Schwarz et al. on "Joint determination of 40K decay constants and 40Ar∗/40K for the Fish Canyon sanidine standard, and improved accuracy for 40Ar/39Ar geochronology" by PR Renne et al.(2010): Geochimica et Cosmochimica Acta, v. 75, no. 17, p. 5097.

Revel, M., Colin, C., Bernasconi, S., Combourieu-Nebout, N., Ducassou, E., Grousset, F. E., Rolland, Y., Migeon, S., Bosch, D., and Brunet, P., 2014, 21,000 Years of Ethiopian African monsoon variability recorded in sediments of the western Nile deep-sea fan: Regional Environmental Change, v. 14, no. 5, p. 1685-1696.

Revel, M., Ducassou, E., Grousset, F. E., Bernasconi, S. M., Migeon, S., Revillon, S., Mascle, J., Murat, A., Zaragosi, S., and Bosch, D., 2010, 100,000 Years of African monsoon variability recorded in sediments of the Nile margin: Quaternary Science Reviews, v. 29, no. 11-12, p. 1342-1362.

Ries, A. C., Shackleton, R. M., Graham, R. H., and Fitches, W. R., 1983, Pan-African structures, ophiolites and mélange in the Eastem Desert of Egypt: a traverse at 26°N Journal of the Geological Society,, v. 140, p. 20.

Rochette, P., Tamrat, E., Féraud, G., Pik, R., Courtillot, V., Ketefo, E., Coulon, C., Hoffmann, C., Vandamme, D., and Yirgu, G., 1998, Magnetostratigraphy and timing of the

Oligocene Ethiopian traps: Earth and Planetary Science Letters, v. 164, no. 3, p. 497-510.

Rogers, J. J., and Santosh, M., 2002, Configuration of Columbia, a Mesoproterozoic supercontinent: Gondwana Research, v. 5, no. 1, p. 5-22.

Rouchy, J. M., and Caruso, A., 2006, The Messinian salinity crisis in the Mediterranean basin: A reassessment of the data and an integrated scenario: Sedimentary Geology, v. 188-189, p. 35-67.

Said, R., 1981, The Geological Evolution of the River Nile.

Salem, R., 1976, Evolution of Eocene-Miocene Sedimentation Patterns in Parts of Northern Egypt: The American Association of Petroleum Geologists Bulletin, v. 60, no. 1, p. 34-64.

Schenk, V., Appel, P., Joens, N., Loose, D., Schumann, A., and Wegner, H., 2007, Metamorphic reworking of the Congo craton in Uganda: Geochimica Et Cosmochimica Acta, v. 71, no. 15, p. A887-A887.

Scrivner, A. E., Vance, D., and Rohling, E. J., 2004, New neodymium isotope data quantify Nile involvement in Mediterranean anoxic episodes: Geology, v. 32, no. 7, p. 565.

Sestini, G., 1989, Nile Delta: a review of depositional environments and geological history: Geological Society, London, Special Publications, v. 41, no. 1, p. 99-127.

Shukri, N. M., 1949, The mineralogy of some Nile sediments: Quarterly Journal of the Geological Society, v. 106, no. 1-4, p. 466-467.

-, 1950, The mineralogy of some Nile sediments: Quarterly Journal of the Geological Society, v. 106, no. 1-4, p. 466-467.

Slingerland, R., 1984, Role of hydraulic sorting in the origin of fluvial placers: Journal of Sedimentary Research, v. 54, no. 1.

Söderlund, U., Patchett, P. J., Vervoort, J. D., and Isachsen, C. E., 2004, The $^{176}$ Lu decay constant determined by Lu–Hf and U–Pb isotope systematics of Precambrian mafic intrusions: Earth and Planetary Science Letters, v. 219, no. 3, p. 311-324.

Sparks, R. S. J., Folkes, C. B., Humphreys, M. C., Barfod, D. N., Clavero, J., Sunagua, M. C., McNutt, S. R., and Pritchard, M. E., 2008, Uturuncu volcano, Bolivia: Volcanic unrest due to mid-crustal magma intrusion: American Journal of Science, v. 308, no. 6, p. 727-769.

Spencer, C. J., Kirkland, C.L. & Taylor, R.J.M. , 2016, Strategies towards statistically robust interpretations of in situ U-Pb zircon geochronology. : Geoscience Frontiers,.

Squire, R. J., Campbell, I. H., Allen, C. M., and Wilson, C. J. L., 2006, Did the Transgondwanan Supermountain trigger the explosive radiation of animals on Earth?: Earth and Planetary Science Letters, v. 250, no. 1–2, p. 116-133.

Stern, R. J., 1994, Arc-assembly and continental collision in the Neoproterozoic African orogen: implications for the consolidation of Gondwanaland: Annual Review of Earth and Planetary Sciences, v. 22, p. 319-351.

Stern, R. J., Ali, K. A., Liegeois, J. P., Johnson, P. R., Kozdroj, W., and Kattan, F. H., 2010, Distribution and significance of Pre-Neoproterozoic zircons in juvenile Neoproterozoic igneous rocks of the Arabian Nubian Shield: American Journal of Science, v. 310, no. 9, p. 791-811.

-, 2011, Distribution and significance of pre-Neoproterozoic zircons in juvenile Neoproterozoic igneous rocks of the Arabian-Nubian Shield: American Journal of Science, v. 310, no. 9, p. 791-811.

Tadesse, S., Milesi, J.-P., and Deschamps, Y., 2003, Geology and mineral potential of

Ethiopia: a note on geology and mineral map of Ethiopia: Journal of African Earth

Sciences, v. 36, no. 4, p. 273-313.

Talbot, M. R., Williams, M. A. J., and Adamson, D. A., 2000, Strontium isotope evidence for

late Pleistocene reestablishment of an integrated Nile drainage network: Geology, v.

28, no. 4, p. 343.

Tchameni, R., Mezger, K., Nsifa, N., and Pouclet, A., 2000, Neoarchaean crustal evolution in

the Congo Craton: evidence from K rich granitoids of the Ntem Complex, southern

Cameroon: Journal of African Earth Sciences, v. 30, no. 1, p. 133-147.

Ukstins, I. A., Renne, P. R., Wolfenden, E., Baker, J., Ayalew, D., and Menzies, M., 2002,

Matching conjugate volcanic rifted margins: 40Ar/39Ar chrono-stratigraphy of pre-

and syn-rift bimodal flood volcanism in Ethiopia and Yemen: Earth and Planetary

Science Letters, v. 198, no. 3, p. 289-306.

Underwood, C. J., King, C., and Steurbaut, E., 2013, Eocene initiation of Nile drainage due to

East African uplift: Palaeogeography, Palaeoclimatology, Palaeoecology, v. 392, p.

138-145.

Walraven, F., and Rumvegeri, B., 1993, Implications of whole-rock Pb☐ Pb and zircon

evaporation dates for the early metamorphic history of the Kasaï craton, Southern

Zaïre: Journal of African Earth Sciences (and the Middle East), v. 16, no. 4, p. 395-

404.

Wilde, S., and Youssef, K., 2002, A re-evaluation of the origin and setting of the Late

Precambrian Hammamat Group based on SHRIMP U–Pb dating of detrital zircons

from Gebel Umm Tawat, North Eastern Desert, Egypt: Journal of the Geological

Society, v. 159, no. 5, p. 595-604.

Williams, M., and Williams, F., 1980, Evolution of the Nile basin: The Sahara and the Nile
(MAJ Williams and H. Faure, Editors). p. . 207-224.

Williams, M. A., and Adamson, D., 1980, Late Quaternary depositional history of the Blue
and White Nile rivers in central Sudan: The Sahara and the Nile (MAJ Williams and H.
Faure, Editors). p. . 281-304.

Williams, M. A., and Adamson, D. A., 1982, A land between two Niles, AA Balkema.

Williams, M. A., and Talbot, M. R., 2009, Late Quaternary environments in the Nile basin,
The Nile, Springer, p. 61-72.

Williams, M. A. J., Adamson, D., Prescott, J. R., and Williams, F. M., 2003, New light on the
age of the White Nile: Geology, v. 31, no. 11, p. 1001-1004.

Woodhead, J. D., and Hergt, J. M., 2005, A preliminary appraisal of seven natural zircon
reference materials for in situ Hf isotope determination: Geostandards and
Geoanalytical Research, v. 29, no. 2, p. 183-195.

Woodward, J. C., Macklin, M. G., Krom, M. D., and Williams, M. A., 2007, The Nile: evolution,
Quaternary river environments and material fluxes: Large rivers: geomorphology and
management, v. 13, p. 712.

# 10.0 Appendices

1. Sample information

2. Major and trace element data

3. Heavy mineral data

4. Petrographic data

5. Tracer isotope data

6. U-Pb zircon data

7. Young age grain calculations for U-Pb zircon

8. U-Pb rutile data

9. Lu-Hf zircon data

10. Ar-Ar Mica and Plagioclase feldspar data

11. Additional Hammamat Group Zircon Data

12. Grain Maps